Doctoral Dissertation
Doctoral Program in Material Science and Technology (36th Cycle)

Nanostructured Materials for Ultrasensitive Detection of Contaminants in Water

By

Matteo Giardino

******

Supervisor:
Prof. D. L. Janner, Supervisor

Doctoral Examination Committee:
Prof. J. Ignes-Mullol , Referee, University of Barcelona
Prof. D. Milanese, Referee, University of Parma
Prof. M. Actis Grande, Politecnico di Torino
Prof. A. Tiraferri, Politecnico di Torino
Dr. F. Chiavaioli, National Research Council

Politecnico di Torino
2023

Declaration

I hereby declare that the contents and organization of this dissertation constitute my own original work and does not compromise in any way the rights of third parties, including those relating to the security of personal data.

Matteo Giardino
2023

* This dissertation is presented in partial fulfillment of the requirements for **Ph.D. degree** in the Graduate School of Politecnico di Torino (ScuDo).

Abstract

Raman spectroscopy is a versatile and non-destructive qualitative and quantitative chemical analysis technique applicable to gas, solid, and liquid samples.
Despite its advantages, the widespread use of Raman spectroscopy has been limited due to the intrinsic weakness of Raman scattering, occurring only for a small fraction of scattered photons (around 1 out of 10^7).
To address this limitation, Fleischmann introduced a variation of this spectroscopy, named surface-enhanced Raman scattering (SERS), which exploits metal nanoparticles to increase the Raman signal by several orders of magnitude thanks to some localized plasmonic resonance phenomena.
This thesis explores diverse methods for preparing Surface-Enhanced Raman Spectroscopy (SERS) sensors, ranging from direct chemical synthesis of gold nanoparticles to metal-thin film deposition on nanostructured substrates. Addressing the challenge of identifying the most versatile and repeatable method, considering sensing conditions and target applications, it provides a first chapter containing a comprehensive review of the optical properties of metals and the principles of SERS.
The second chapter delves into the direct chemical synthesis of SERS substrates, which is performed using optimized process parameters studied through a Monte Carlo simulation to maximize the SERS signal intensity of a certain Raman band for a given excitation wavelength. Such an approach allowed for the preparation of the SERS sensor, which demonstrated a detection limit of 0.32 nM for skatole in water at an excitation wavelength of 785 nm.
A second innovative technique, described in Chapter 3, involves vapor-phase chemical dewetting for synthesizing silver nanoparticles, showcasing versatility in both SERS detection Rhodamine-6G and application as a shadow mask for silicon etching.
Such an approach, which is based on the exposure of a thin film to hot water or acid vapor, is a valid alternative to thermal or laser treatments to induce the dewetting in the spinodal regime due to its lower cost and the possibility of working on heat-sensitive substrates.
The fourth chapter discusses the preparation of SERS sensors by depositing thin films on nanostructured substrates, demonstrating exceptional sensitivity in detecting solid contaminants such as nanoplastics. In particular, a soda-lime glass nanostructure is created by dry etching using a copper nanoparticle as a shadow mask and coated with a variable thickness of the gold or silver thin film. The gold-coated device was successfully employed for the detection of 100 nm polystyrene nanoparticles in water, exhibiting a record limit of detection of 0.68 ng mL^{-1}, almost three orders of magnitudes better than the current state of the art.
Furthermore, the last chapter emphasizes the importance of analytical software tools for the advanced processing of microscope images, facilitating comprehensive characterization of micro and nanostructured surfaces.
The thesis concludes by summarizing findings and discussing future perspectives for advancing SERS technology.

TABLE OF CONTENTS

LIST OF ACRONYMS

AFM	Atomic Force Microscopy
APTMS	(3-aminopropyl)triethoxysilane
BEM	Boundary Element Method
BSE	Backscattered electron
CB	Conduction band
DETA	(3-Trimethoxysilyl-propyl)diethylene-triamine
DLS	Dynamic light scattering
DoF	Depth of field
EDS	Energy dispersion spectroscopy
FESEM	Field emission scanning electron microscopy
FQSSD	Four quadrants backscattered electron detector
HFDS	heneicosafluorododecyltrichlorosilane
HNG	Hole nucleation and growth
LID	Laser induced dewetting
LOD	Limit of detection
LOQ	Limit of quantification
LSPR	Localized surface plasmon resonance
MBA	4-Mercaptobenzoic acid
NIR	Near Infrared region
NND	Nearest neighbor distribution
NP	Nanoparticle
PAMAM	Poly(amidoamine)
PBSE	Pseudobackscattered electron
PTE	Polyethieleneterephatalate
PTFE	Polytetrafluoroethylene
RIE	Reactive Ion Etching
RSA	Random sequential adsorption
SAEF	Surface averaged enanchement factor
SAM	Self-assembled monolayer
SD	Spinodal decomposition
SEF	SERS enhancement factor
SEM	Scanning electron microscope
SERS	Surface enhanced Raman spectroscopy
SLERSA	Self-limiting extended random sequential adsorption
SNR	Signal-to-noise ratio
SSD	Solid state detector
SVH	Spherical vector harmonics

TE	Track etched
TF	Thin film
UTF	Ultra-thin film
UV	Ultraviolet
VB	Valence band
XPS	X-ray photoelectron spectroscopy
XRD	X-ray diffraction

LIST OF FIGURES

INTRODUCTION AND OBJECTIVES

Surface Enhanced Raman Spectroscopy (SERS) is, nowadays, a pretty common technique for the study and detection of contaminants and biomolecules in water at concentrations as low as 10^{-12}-10^{-11} M. Different methods for preparing SERS sensors are available, and it is challenging to identify the most versatile and repeatable without considering the sensing conditions and the target applications.
This thesis aims to investigate the preparation of SERS sensors by different methods, ranging from the direct chemical synthesis of gold nanoparticles to the metal-thin film deposition on a previously nanostructured substrate. The advantages and disadvantages of each of these sensors are discussed, and an estimate of the detection limit is provided to better address the reader towards the most efficient technology for his own application.

- Chapter 1 - FUNDAMENTALS ON OPTICAL PROPERTIES OF METALS AND SURFACE ENANCHED RAMAN SPECTROSCOPY. This chapter serves as a review of the state of the art and as an introduction to the principles on which SERS is based. Optical properties of bulk metals are introduced, and their evolution is described as the materials are scaled down to nanometric size. The chapter also introduces Raman spectroscopy, putting in evidence its limitations and the need for a more sensitive technique, such as Surface Enhanced Raman spectroscopy, whose mechanism is also briefly discussed.

- Chapter 2 – SERS SUBSTRATE BY DIRECT CHEMICAL SYNTHESIS. This chapter deals with the preparation of SERS substrates by deposition of metal nano seeds on a functionalized substrate and their subsequent growth to tune both the size and the morphology of the nanoparticles. This chapter also describes the optimization of the substrate through Monte Carlo simulation of the seed deposition. Such SERS sensors have been successfully employed for the detection of skatole in water, achieving a limit of detection below 1 nM.

- Chapter 3 – SERS SUBSTRATE BY VAPOUR-PHASE CHEMICAL DEWETTING OF THIN FILM. This chapter introduced a highly innovative technique for synthesizing silver nanoparticles: the vapor-phase chemical dewetting. These methods simply consist of exposing a silver thin- or ultra-thin film to a high-volatility acid (e.g., HCl or HNO3) or hot water vapor to induce instability and obtain the dewetting of the film to form nanoparticles or nanoparticles. The obtained nanoparticles have been employed for the detection of Rhodamine6G in a concentration as low as 10^{-10} M. The application of the obtained nanoparticles as a shadow mask for silicon etching is also described.

- Chapter 4 – SERS SUBSTRATES BY THIN-FILM DEPOSITION ON PILLAR-NANOSTRUCTURED GLASSES. This chapter deals with preparing SERS sensors by depositing a gold or silver thin film on a previously nanostructured substrate. In this work, we used a soda-lime glass substrate etched in reactive ion etching using copper nanoparticles prepared by laser-induced dewetting as a shadow mask. The effectiveness as a SERS sensor was demonstrated by successfully detecting a 500 nM solution of 4-mercaptobenzoic acid and polystyrene nanoparticles, obtaining an extraordinary limit of detection of 0.8 ng mL^{-1}. In the same chapter, we will also discuss the preparation of a SERS sensor on a polyethylene terephthalate track-etch filtering membrane by oxygen plasma and the subsequent deposition of a silver or gold thin film.

- Chapter 5 – SOFTWARE ANALYTICAL TOOL. The preparation of SERS sensors and generally nanostructured surfaces usually requires a comprehensive characterization. In the frame of this thesis work, several analytical tools for the advanced processing of microscope (both optical and electron) images were developed and are briefly illustrated in this chapter.

- Chapter 6 – CONCLUSIONS AND FUTURE PERSPECTIVE. The conclusions of the research work are drawn and some possible future developments are discussed.

Chapter 1
FUNDAMENTALS ON OPTICAL PROPERTIES OF METALS AND SURFACE ENHANCED RAMAN SPECTROSCOPY

This chapter begins with a gentle introduction to the optical properties of bulk metal, describing the different mechanisms of interaction of the matter with the electromagnetic fields and providing a quantitative description, employing a classical theory known as the Drude-Lorentz model. The attention is then focused on the optical properties of nanostructured metals to illustrate how the confinement due at the nanometer scale influences the electronic structure of the metal and, therefore, its optical properties.

We'll start from some fundamental considerations on the optical modes in a metal nanoparticle introduced through a simple quasi-static calculation following the Clausis-Mossotti equation, later we'll expand the theoretical framework by discussing Mie's theory's fundamentals and major results. Finally, the presented theoretical backgorund is used to introduce the *Surface Enhanced Raman Spectroscopy* (SERS), which is the main topic of the present thesis, and its fundamentals.

1.1 OPTICAL PROPERTIES OF BULK METALS

Metals can present different electronic structures, as illustrated in Figure 1. Some metals, such as alkali metals, magnesium, and aluminum, show a completely filled valence band (VC) and partially filled conduction band (CB). In this case, when electrons are excited by an external field, they are likely to move from two different levels in the conduction band, and most of the electronic properties are determined by the *intraband transitions* within the CB. Given their typical associated energies, these transitions contribute to the absorption in the IR frequency range and the reflection in the visible range.

Intraband transition can be easily modeled using a classical approach known as Drude's model. In this theory, the electron is treated as a free particle gas and the correlation between their positions is described in terms of collective oscillations at a frequency ω.

If the electrons are excited by a wave with a frequency below the plasma frequency ω_P, this can determine the reflection as they can screen the field of the incident wave. On the contrary, if they are excited above the plasma frequency, they cannot respond fast enough, and the behavior of the metal is similar to that of a dielectric.

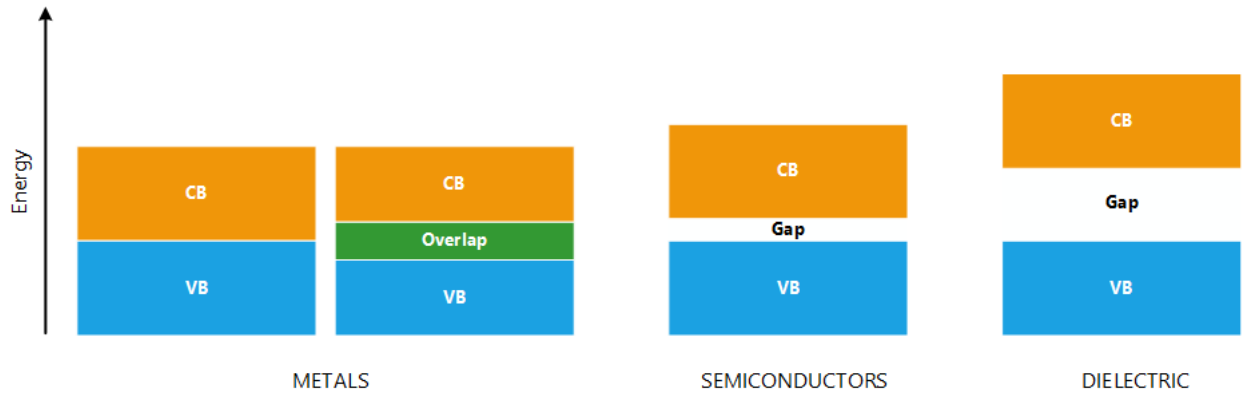

Figure 1: Different electron band structures observed in metals, semiconductors, and dielectric. Metals can have either a filled valence band (VB) adjacent to the conduction band (CB) or an overlapping of these two. In semiconductors and dielectrics, the VB and CV are separated by a gap of different amplitude.

Other metals can also present a structure that allows some *interband transition*, i.e. transitions from VC to CB or from CB to other unoccupied levels are possible. Moreover, in noble metals, such as copper and gold, both contributions are relevant and can influence the electric/optical response of the material over a very broad range of frequencies. In fact, Cu and Au are the two only colored metals within the periodic table while all the others are substantially colorless [1].
This happens due to the fact that their electronic configuration is an exception to the well-known Aufbau principle [2] which dictates an increasing energy order for filling the atomic subshells, thus giving $[Ar]3d^9 4s^2$ for copper and $[Xe]5d^9 6s^2$ for gold. From both theoretical calculation and experimental measurements, we observe that the energy required for the 5d⟶6s transition in Au and for the 3d⟶4s in Cu is equal to 1.9 eV [3] and 2.7 eV [4] respectively, implying that these two metals absorb in the blue region giving them yellow and brown-red color respectively.
The very low transition energy value for Au is due to its high atomic mass, which leads to relativistic effects that raise the energy of the 5d band and lower the energy of the 6s band.
Silver has a similar electronic configuration (e.g. $[Kr]4d^9 5s^2$) but endures a very low relativistic effect and has a transition energy equal to 4.8 eV. For this reason, its absorption is located in the UV range, and it appears to be colorless.

1.2 DIELECTRIC CONSTANT AND REFRACTION INDEX

Supposing that the total charge density ρ is zero, Maxwell's equations in a macroscopic medium can be written in the following form:

$$\vec{\nabla} \times \vec{H} - \frac{1}{c}\frac{\partial \vec{D}}{\partial t} = \frac{4\pi}{c}\vec{j}$$
$$\vec{\nabla} \times \vec{E} + \frac{1}{c}\frac{\partial \vec{B}}{\partial t} = 0 \qquad (1.1)$$

$$\vec{\nabla} \cdot \vec{D} = 0$$
$$\vec{\nabla} \cdot \vec{B} = 0$$

Where $\vec{H}$ is the magnetic field vector, $\vec{E}$ is the electric field vector, $\vec{D}$ is the electric displacement field vector and $\vec{B}$ is the magnetic flux density vector.
For an electromagnetic field, we look for a solution to the Maxwell'sequations in the form of a plane wave:

$$\vec{E}_i(\vec{r}, t) = \vec{E}_0 \, exp(\vec{k} \cdot \vec{r} - \omega t) \tag{1.2}$$

Where the vector $\vec{k}$ is a complex vector named propagation constant and ω is the angular frequency of the wave.

It is important to note that we can decompose the propagation constant into a real part $\overrightarrow{k'}$, also named wave vector which describes the wave propagation in the medium, and an imaginary part $\overrightarrow{k''}$ which describes the damping of the field.

$$\vec{k} = \overrightarrow{k'} + i\overrightarrow{k''} \tag{1.3}$$

The modulus of the propagation constant[5] is given as:

$$|\vec{k}| = \sqrt{-\omega^2 \mu\varepsilon + j\omega\mu\sigma} \tag{1.4}$$

The norm of the propagation constant can be related to the dielectric constant ε and the magnetic permeability μ of the material through the following relation:

$$k = \frac{\omega}{c}\sqrt{\varepsilon\mu} \tag{1.5}$$

Please note that, since in the present thesis we are only dealing with non mangetic materials and with fields in the visible or near infrared (NIR) range we always assume, unless differently specified, that $\mu = 1$.
In conclusion, a refractive index (complex) $\tilde{n}$ can be defined as the square root of the ratio of the product $\varepsilon\mu$ in the medium and $\varepsilon_0\mu_0$ in vacuum.

$$\tilde{n} = \sqrt{\frac{\varepsilon\mu}{\varepsilon_0\mu_0}} \tag{1.6}$$

1.3 DRUDE AND DRUDE LORENTZ MODEL

Once we defined the meaning of the dielectric constant and how it relates to the optical properties of the material, we can introduce the microscopical mechanism which determines the optical response of the material. In the frame of this thesis, we will introduce only classical and semi-classical models, leaving the quantum mechanical approach to specialized textbooks.

Let's consider a generic electromagnetic radiation in the form of a plane wave again. For simplicity, we consider an isotropic material made of electrons bound to the nuclei that we assume to be represented as randomly oriented harmonic oscillators. In this case, we can neglect the spatial propagation in equation (1.2) and we can rewrite it as follows:

$$\vec{E} = \overrightarrow{E_0} \exp(i\omega t) \tag{1.7}$$

When interacting with a solid material, such a field exerts on its electrons a drag force $\overrightarrow{F_e}$ given by:

$$\vec{F_e} = -e\vec{E} = -e\overrightarrow{E_0} \exp(i\omega t) \tag{1.8}$$

Due to the collisions among all the moving electrons a viscous friction force $\vec{F_f}$ is developed. This friction force opposes the drag action of the electric field:

$$\vec{F_f} = -\frac{m_e \overrightarrow{v_d}}{\mu} \tag{1.9}$$

Moreover, a recall force representing the bond between the electrons and their respective nuclei should also be taken into account. However, since electrons are free to move from one nucleus to another according to the metallic bond model, we can, for the moment, neglect the contribution of such recall force. Thus, according to Newton's law, and considering the (1.7),(1.8) and (1.9), we can obtain the following equation of motion for the metal electrons:

$$m\frac{d^2\vec{x}}{dt^2} = \sum \vec{F_i} = -e\overrightarrow{E_0} \exp(i\omega t) - \frac{m_e \overrightarrow{v_d}}{\mu} \tag{1.10}$$

By considering the electron in a one-dimensional system and rearranging equation (1.10) one can obtain the following differential equation:

$$\frac{d^2x}{dt^2} + \frac{1}{\mu}\frac{dx}{dt} + \frac{eE_0}{m} \exp(i\omega t) = 0 \tag{1.11}$$

A solution to (1.11) can be found in the form:

$$x(t) = -\frac{eE_0}{-m(\omega^2 + i\gamma\omega)} \exp(i\omega t) \tag{1.12}$$

From this, it can be proven that the dielectric constant according to Drude's model [6] for the free-electron $\varepsilon_F(\omega)$ is given as in (1.13).

$$\varepsilon_F(\omega) = 1 - \frac{\omega_P^2}{\omega^2 + i\gamma\omega} \tag{1.13}$$

Where $\omega_P = \frac{N_e e^2}{\varepsilon_0 m_e}$ is a natural reference frequency of the system named *plasma frequency*.
By rearranging equation (1.13) the real and imaginary parts of the complex dielectric constant can be expanded as follows:

$$\varepsilon_F(\omega) = \varepsilon_F'(\omega) + i\,\varepsilon_F'(\omega) = \left(1 - \frac{\omega_P^2\gamma^{-2}}{1 + \omega^2\gamma^{-2}}\right) + i\left(\frac{\omega_P^2\gamma^{-1}\omega^{-1}}{1 + \omega^2\gamma^{-2}}\right) \tag{1.14}$$

In an ideal metal, the electrons fully behave as an ideal gas of electrons, and therefore, there will be no viscous damping forces, i.e. $\gamma = 0$. For this reason, the dielectric constant should become a purely real number and can be simplified in the following form.

$$\varepsilon_F(\omega) = 1 - \frac{\omega_P^2}{\omega^2} \tag{1.15}$$

The same expression is obtained even if $\gamma \neq 0$, but the metal is in the so-called high-frequency regime, i.e., the frequency is very close to plasma frequency, and therefore the damping is negligible ($\omega\gamma^{-1} \gg 1$). This situation, where we can neglect the damping term, is also known as the *transparency regime*.
All the cases analyzed so far represent a system where only intraband transitions, i.e., free-electron contribution, are considered. However, it is possible to take into account interband transitions by adding a recall force contribution. This contribution, representing the bonding interaction between the electrons and their respective nuclei, is given as:

$$\vec{F}_r = \omega_0^2\vec{x} \tag{1.16}$$

If we include this contribution to the force balance of equation (1.10), we obtain the following motion equation:

$$\frac{d^2x}{dt^2} + \frac{1}{\gamma}\frac{dx}{dt} + \omega_0^2 x + \frac{eE_0}{m}\exp(i\omega t) = 0 \tag{1.17}$$

By solving (1.17), we obtain, similar to what has been done for the Drude model, an expression for the complex amplitude of the electron motion.

$$\frac{d^2x}{dt^2} + \frac{1}{\gamma}\frac{dx}{dt} + \omega_0^2 x + \frac{eE_0}{m}\exp(i\omega t) = 0 \tag{1.18}$$

Analogously to the previous approach, the solution to this equation can be calculated as follows:

$$x(t) = \frac{qE_0}{m}\frac{1}{\omega_0^2 - \omega^2 - i\omega\gamma}\exp(i\omega t) \tag{1.19}$$

And we can obtain the dielectric constant for the bound case:

$$\varepsilon_B(\omega) = 1 - \frac{\omega_P^2}{\omega^2 - i\omega\gamma - \omega_0^2} \tag{1.20}$$

As stated previously, in some metals we can have a contribution from both intraband and interband transition so that a good representation of the dielectric constant is given by the so-called Drude-Lorentz model [6] :

$$\varepsilon(\omega) = \varepsilon_F(\omega) + \varepsilon_B(\omega) = 1 - \frac{\omega_P^2}{\omega^2 + i\gamma\omega} - \frac{\omega'^2_P}{\omega^2 - i\omega\gamma' - \omega_0^2} \tag{1.21}$$

In Figure 2a, the equation of Drude's model (1.15) is used to fit the optical data of gold obtained by Johnson and Christy[7]. Whereas the model can accurately fit the experimental data in the near-infrared region, it is unable to represent the behavior below a wavelength of 600 nm. In b), we report the same optical data by Johnson and Christy fitted with an extended Drude-Lorentz model (1.16). This model improves the accuracy of the representation until a wavelength of around 450 nm by introducing the adsorption by the interband transition.

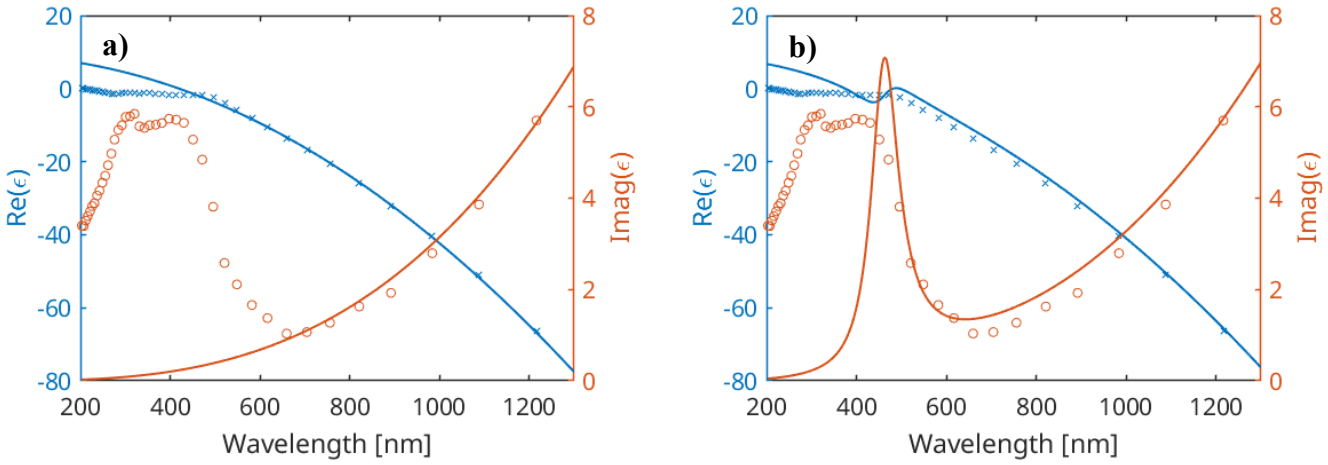

Figure 2: (a) Fitting of the dielectric constant of gold using Drude's model and (b) fitting of the dielectric constant of gold using Drude-Lorentz's model. It is clearly shown how Drude's model doesn't reproduce the interband transition.

1.4 ELECTRIC FIELD AT THE INTERFACE BETWEEN A DIELECTRIC AND A METAL

Let's now consider a single interface between a dielectric and metal layers [8], [9], as reported in Figure 3.

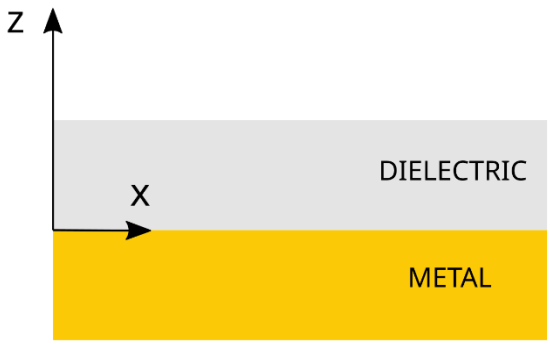

Figure 3: Geometry of the interface between a metal and a dielectric whose optical properties are discussed within this section.

In many reference textbooks, it is shown that by rearranging Maxwell's equations, assuming no external charges and current are present, one can obtain a wave equation in the form of a Helmholtz equation (1.22):

$$\nabla\vec{E} + \mu\varepsilon\frac{\omega^2}{c^2}\vec{E} = 0 \tag{1.22}$$

These equations must be solved for the two regions, i.e. metal and dielectric regions, and the obtained solution must be connected through appropriate boundary conditions.

At this point, we want to study the behavior of an electromagnetic wave propagating perpendicularly to a dielectric-metal interface. For a reason that will be clarified in the following, we start looking for a solution to the Helmholtz equation in the form of a *p*-polarized (transverse magnetic) wave.

Due to the symmetry of the system, we assume the x component of the wave vector to be constant and equal in the two mediums, i.e. $k_x = k_x^D = k_x^M$.

We can, therefore, write the following set of equations for the two media:

$$\begin{cases} E_x^D = E_0 \exp(ik_x x + ik_z^D z) & z > 0 \\ E_x^M = E_0 \exp(ik_x x - ik_z^M z) & z < 0 \end{cases} \tag{1.23}$$

The imposition of the continuity conditions at the interface requires that components of the wave-vector parallel to propagation direction in the dielectric and in the metal are given, respectively, from (1.24) and (1.25):

$$k_z^D = \sqrt{(n^D k_0)^2 - k_x^2} = \sqrt{\frac{\varepsilon_D}{c^2}\omega^2 - k_x^2} \tag{1.24}$$

$$k_z^M = \sqrt{(n^M k_0)^2 - k_x^2} = \sqrt{\frac{\varepsilon_M}{c^2}\omega^2 - k_x^2} \tag{1.25}$$

We now require that both k_Z^D and k_z^M have a positive imaginary part, so that the wave will decay exponentially within the two media, i.e. $Im(k_z^D) > 0$ and $Im(k_Z^M) > 0$. By repeating the same calculation for a TM wave it can be proved that no surface mode exists, so one can conclude that surface plasmons are photonic modes that exist only for TM-polarized waves.

$$\begin{cases} E_z^D = -\dfrac{kE_0}{k_z^D}\exp(ik_x x + ik_z^D z) & z > 0 \\ E_x^M = \dfrac{kE_0}{k_z^M}\exp(ik_x x - ik_z^M z) & z < 0 \end{cases} \tag{1.26}$$

By imposing the continuity condition of the z-component of the field across the interface one obtain the following relations:

$$\varepsilon_D k_z^M = \varepsilon_M k_z^D \tag{1.27}$$

We now replace (1.27) with (1.24) and (1.25) and solve for k_x, which is also denoted in many textbooks as $K_{SP}(\omega)$:

$$K_{SP}(\omega) = \frac{\omega}{c}\sqrt{\frac{\varepsilon_D \varepsilon_M}{\varepsilon_D + \varepsilon_M}} \tag{1.28}$$

By assuming the permittivity of the dielectric equal to 1 and replacing with Drude's model equation in the (1.15) the dispersion relation as a function of ω is easily obtained and is reported in Figure 4.

$$K_{SP}(\omega) = \frac{\omega}{c}\sqrt{\frac{\omega^2 - \omega_P^2}{2\omega^2 - \omega_P^2}} \tag{1.29}$$

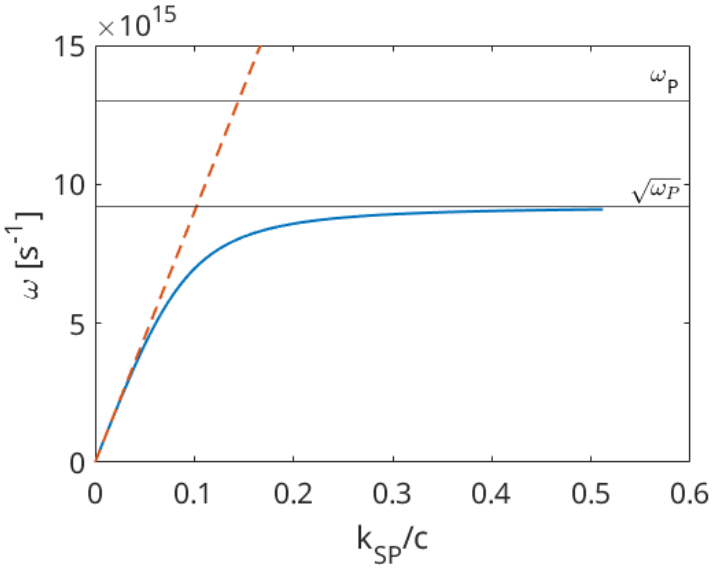

Figure 4: Dispersion relations for a surface plasmon. The red dashed line indicates the light line.

For both the dielectric and the metal, we can define the skin depth, L_D and L_M respectively, as the distance normal to the interface at which the amplitude of the field is reduced by a factor $e = 2.718$.

$$L_D = \frac{\lambda}{2\pi}\left(\frac{\varepsilon_M + \varepsilon_D}{\varepsilon_D^2}\right)^{\frac{1}{2}} \tag{1.30}$$

$$L_M = \frac{\lambda}{2\pi}\left(\frac{\varepsilon_M + \varepsilon_D}{\varepsilon_M^2}\right)^{\frac{1}{2}} \tag{1.31}$$

The values of skin depth for the metal are usually of the order of some tenths of nanometers. For example, for gold/air and silver/air interface at 630 nm, the skin depth of the metal is 29 nm and 24 nm, respectively [8].
Moreover, we can define the propagation length L_p as the distance parallel to the interface at which the amplitude of the field is reduced by a factor e.

$$L_p = \frac{1}{2\beta''} \tag{1.32}$$

1.5 LOCALIZED SURFACE PLASMONS

So far, we have dealt with plasmonic resonance at a plane dielectric-metal interface. However, by exciting the plasmon in a nanoparticle with a size smaller or comparable to the radiation wavelength, it is possible to obtain a confined mode named *localized surface plasmon*[10]. This

confinement, which, for the case of spherical nanoparticles, is along all three dimensions, is such that the particles can support only discrete plasmonic modes[9].
The confinement of the plasmonic modes essentially give two effects on the optical properties of the particle:

- The electric field is strongly enhanced in proximity of the particle surface.
- The particle shows strong adsorption with a maximum corresponding to its plasmon resonance frequency.

The localized surface plasmon in a spherical metal particle can be studied readily in a quasi-static approximation. Being the particle radius is much smaller than the wavelength, it is legitimate to assume that the field is constant over the entire particle, and the problem is reduced to one of a sphere in an electrostatic field.
Given an electrostatic $\overrightarrow{E_0}$ field impinging on a particle radius a, one can write the induced electrical potential inside ϕ_{in} and outside ϕ_{out} particle as:

$$\phi_{in} = \frac{-3\varepsilon_D}{\varepsilon_M + 2\varepsilon_D} E_0 r \cos\theta \tag{1.33}$$

$$\phi_{out} = -E_0 r \cos\theta + a^3 E_0 \frac{\varepsilon_M - \varepsilon_D}{\varepsilon_M + 2\varepsilon_D} \frac{\cos\theta}{r^2} \tag{1.34}$$

From (1.33) and (1.34), following some simple passages described by Xu, one can prove that the polarizability of the sphere is given from the Clausius-Mossotti relations:

$$\alpha = 4\pi\varepsilon_0 a^3 \frac{\varepsilon_M - \varepsilon_D}{\varepsilon_M + 2\varepsilon_D} \tag{1.35}$$

From this, it is clear that the polarizability diverges for the denominator $\varepsilon_M + 2\varepsilon_D = 0$ and therefore leads to a resonance. Suppose we can assume that the imaginary part of the metal-dielectric constant is slowly changing. In that case, the resonance condition can be rewritten in a simplified form, generally known as Frohlich conditions:

$$Re[\varepsilon_M(\omega)] = -2\varepsilon_D \tag{1.36}$$

From (1.35) and (1.36) we can observe that the magnitude of polarizability is proportional to a^3 but the frequency of resonance is determined only by the dielectric constant of the particle and the surrounding medium. However, this formula is in total disagreement with the experiments, where it is observed that the resonance peak undergoes a redshift when the particle size increases. In fact, as the particle's radius becomes closer to the radiation wavelength, the electromagnetic field can not be considered uniform within the particle anymore, and retardation effects must be considered.

Moreover, by increasing the particle size, the damping due to scattering contribution becomes relevant, and a broadening of the resonance peak is also observed. A corrected version of the polarizability is given by a modified long-wavelength approximation (MWLA):

$$\alpha_{MLWA} = \frac{\alpha}{1 - \frac{\alpha}{4\pi a}k^2 - \frac{\alpha}{6\pi}ik^3} \tag{1.37}$$

Introducing the (1.37) in the definition of absorption cross section derived from Rayleigh scattering theory one obtains:

$$C_{Abs} = \frac{P_{Abs}}{I_0} = k\, Im(\alpha) = k4\pi\varepsilon_0 a^3 Im\left(\frac{\varepsilon - \varepsilon_M}{\varepsilon - 2\varepsilon_M}\right) \tag{1.38}$$

From (1.38) it is clear that the resonance frequency is also dependent on the dielectric constant of its surroundings. Increasing the nanoparticle size will shift the resonance frequency to higher values (red-shift), whereas a decrease will cause a blue-shift.
A metal sphere immersed in an air surrounding exhibits a resonance at:

$$\omega = \frac{1}{\sqrt{3}}\omega_P \tag{1.39}$$

This localized electric field enhancement has been exploited for several photonics applications. In the rest of this section, we will focus on the use of localized surface plasmons for spectroscopic and microscopy applications.

1.6 MIE-SCATTERING FOR SPHERICAL PARTICLES

If we consider Maxwell's equations in vacuum and rearrange them, we can obtain the so-called vector Helmholtz equation:

$$\left(\vec{\nabla} + k^2\right)\vec{E} = \left(\vec{\nabla} + k^2\right)\vec{H} = 0 \tag{1.40}$$

The analytical solution to the problem of scattering by a sphere was introduced by the physicist Gustave Mie in 1908 [11], [12]. The following description is largely based on the treatise by Bohren and Huffman [11].
Due to the spherical geometry of the system, his approach is largely based on the spherical harmonics expansion of the incident wave in the inner and outer regions of the scattering sphere. As the spherical harmonics constitute a complete orthonormal set, any other function can be expressed as an infinite sum of these harmonics.
We can solve Laplace's equation in spherical coordinates the method of separation of variables, obtaining a solution that is the product of three functions:

$$E(r,\theta,\phi) = R(r)\Theta(\theta)\Phi(\phi) \tag{1.41}$$

The term Φ, which is a function of the azimuthal angle ϕ, is in the form

$$\Phi(\phi) = e^{\pm jm\phi} \tag{1.42}$$

The Θ dependent term is given by the so-called Legendre's polynomials P_n^m

$$\Theta(\theta) = P_n^m(\cos\theta) \tag{1.43}$$

And finally, the radial dependency is represented by one of the four spherical Bessel's functions z_n

$$\mathrm{R}(r) = z_n(kr) \tag{1.44}$$

Therefore we can write the function as two functions with different symmetry due to the behavior of the azimuthal terms: an even function ψ_{emn} and odd one ψ_{omn}:

$$\begin{aligned} \psi_{emn} &= z_n(kr)P_n^m(\cos\theta)\cos m\phi \\ \psi_{omn} &= z_n(kr)P_n^m(\cos\theta)\sin m\phi \end{aligned} \qquad n = 1,2,\dots,\infty \quad m = 0,\pm1,\pm2,\pm n \tag{1.45}$$

Being all the factors $z_n(kr)$, $P_n^m(\cos\theta)$ and $\cos m\phi$ a complete orthonormal set, every solution of Helmoltz equations can be expressed as a linear combination of the (1.45).

In particular, the angular part of the, known as *spherical harmonics functions***,** is a complete orthonormal set over a sphere. For this this reason all the functions define over the surface of a sphere can be expressed a sum of spherical harmonics functions.

However, Mie's method aims to find a vector field that is a solution of the wave equation in its vectorial form. We introduce another vector function, named *spherical vector functions* (SVH) [13]–[15], and defined as:

$$\vec{M}_{nm} = \vec{\nabla} \times (\psi_{nm}\ \vec{r}) \tag{1.46}$$

$$\vec{N}_{nm} = \frac{1}{k}\vec{\nabla} \times \vec{M}_{nm} \tag{1.47}$$

We can easily demonstrate that both (1.46) and (1.47) are null-divergence solutions of Helmholtz equation, i.e.:

$$\left(\vec{\nabla} + k^2\right)\vec{M}_{nm} = \left(\vec{\nabla} + k^2\right)\vec{N}_{nm} = 0 \tag{1.48}$$

$$\vec{\nabla} \cdot \vec{M}_{nm} = \vec{\nabla} \cdot \vec{N}_{nm} = 0 \tag{1.49}$$

At this point, every electric field whose solution of Maxwell's equations can be expressed as an infinite sum of these vector spherical harmonics. We obtain the following expression for the incident field $\vec{E}_{inc}$, the scattered field outside the particle $\vec{E}_{sca}$ and the field inside the particle $\vec{E}_{inn}$.

$$\begin{aligned}
\vec{E}_{inc} &= E_0 \sum_{n=1}^{\infty} \frac{i^n(2n+1)}{n(n+1)}\left[\vec{M}_{on1}(k_M) - i\vec{N}_{en1}(k_M)\right] \\
\vec{E}_{sca} &= -E_0 \sum_{n=1}^{\infty} \frac{i^n(2n+1)}{n(n+1)}\left[b_n\vec{M}_{on1}(k_M) - ia_n\vec{N}_{en1}(k_M)\right] \\
\vec{E}_{inn} &= E_0 \sum_{n=1}^{\infty} \frac{i^n(2n+1)}{n(n+1)}\left[\beta_n\vec{M}_{on1}(k_M) - i\alpha_n\vec{N}_{en1}(k_M)\right]
\end{aligned} \tag{1.50}$$

We apply the boundary conditions at the particle interface to obtain the following identities for both the field $\vec{E}$ and $\vec{H}$ of the (1.51) and (1.52) respectively.

$$\left(\vec{E}_{inc} + \vec{E}_{sca}\right) \times u_r = \vec{E}_1 \times u_r \tag{1.51}$$

$$\left(\vec{H}_{inc} + \vec{H}_{sca}\right) \times u_r = \vec{H}_1 \times u_r \tag{1.52}$$

The coefficients a_n and b_n are the coefficients from the expansion of the electrical field into spherical harmonics and are given as in (1.53) and (1.54).

$$a_n = \frac{m\psi_n(mx)\psi'_n(x) - \psi'_n(mx)\psi_n(x)}{m\psi_n(mx)\eta'_n(x) - \psi'_n(mx)\eta_n(x)} \tag{1.53}$$

$$b_n = \frac{\psi_n(mx)\psi'_n(x) - m\psi'_n(mx)\psi_n(x)}{\psi_n(mx)\eta'_n(x) - m\psi'_n(mx)\eta_n(x)} \tag{1.54}$$

The scattering cross-section is defined as the ratio between the scattered power W_s and the incident flux I_i is given as:

$$C_{sca} = \frac{W_s}{I_i} = \frac{2\pi}{k^2}\sum_{n=1}^{\infty}(2n+1)(|a_n|^2 + |b_n|^2) \tag{1.55}$$

Similarly, the extinction cross-section C_{ext} defined as the ratio between the total power scattered and absorbed by the object W_{ext} and the incident flux I_i is given as:

$$C_{ext} = \frac{W_{ext}}{I_i} = \frac{2\pi}{k^2}\sum_{n=1}^{\infty}(2n+1)Re(a_n + b_n) \tag{1.56}$$

More details and a Fortran implementation of the Mie methods for studying the light scattering by a sphere are available in the textbook by Bohren and Huffman [11].
Examples of the cross-sections for a silver and gold nanoparticle calculated with Mie's theory are reported in Figure 5 and Figure 6, respectively.

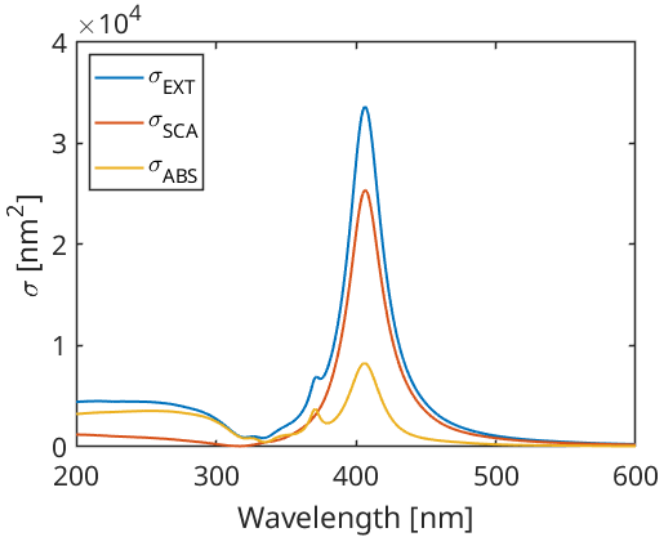

Figure 5: Extintion, Scattering, and Absorption cross section for a silver nanoparticle of diameter d=50 nm in a water media (n=1.33). Calculations have been obtained by Mie's method using the PyMieScatt [16] Python library.

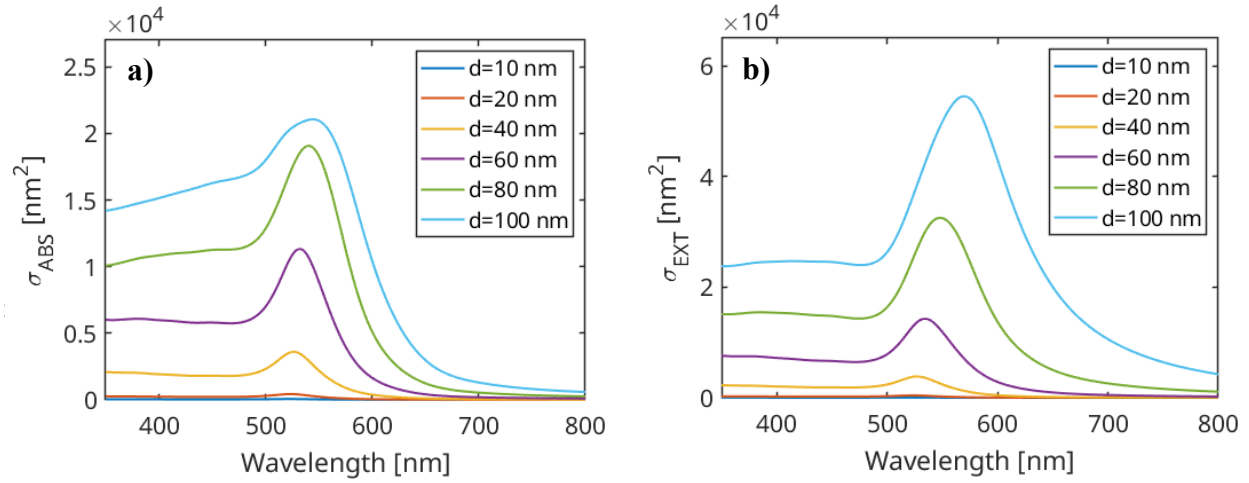

Figure 6: Absorption cross-section a) and extinction cross-section b) for gold nanoparticles of different diameters d in a water media (n=1.33). Calculations have been obtained bye Mie's method using the PyMieScatt [16] Python library.

1.7 SURFACE ENHANCED RAMAN SPECTROSCOPY

Microscopically, when light interacts with a molecule it can induce energy transition which can be classified as:

- *Electronic transitions:* if an electron is excited from an energy level to another level of higher energy.
- *Vibrational (or internal) transitions*: if the molecule is promoted to a higher vibration or rotational energy level.

On the other hand, if we consider the macroscopic behavior when electromagnetic radiation impinges on a material, different types of interactions can be observed:

- Transmission: the radiation doesn't interact with the material and is transmitted. This is the typical behavior of dielectric materials.
- Absorption: if the field can couple with some state transitions, e.g., electron or vibrational transitions, some energy is transferred from the photon to the material. This leads to the excitation of a molecule from the initial energy E_A to an excited state of energy E_B, where the transferred energy is given as $\Delta E = E_B - E_A$.

Suppose the absorption is due to electronic transition. In that case, it occurs in the UV (small molecules) or visible (dyes) region, whereas if the vibrational transition is excited, absorption occurs in the IR region. In other cases, we have the phenomenon of scattering: the light interacts with the molecule, distorting the cloud of electrons around the nuclei. The relaxation of the electrons releases energy in the form of scattered radiation.

Scattering can be, in turn, classified as elastic if the photon energy is conserved or inelastic if the photon energy is changed, either increased or decreased.
If the cloud of electrons is deformed without nuclear displacement, there is no significant change in photon energy, and the scattering is considered an elastic process. On the contrary, if the light induces a displacement of the nuclei, we observed a change, either increase or decrease, of the photon energy [17].
Nowadays we define *Raman scattering* as the inelastic scattering effect discovered by Chandrasekhara Venkata Raman in India in 1921 [18].
The main difference between fluorescence and Raman scattering is that the latter is a simultaneous process of absorption and emission. In contrast, the former requires some intermediate steps (e.g. a metastable state). Therefore, Raman scattering is also possible without direct absorption, does not require any electronics transition, and makes the use of different excitation wavelengths in the transparency region possible.
The inelastic Raman scattering can be further classified as (see Figure 7):

- *Anti-Stokes scattering*: the emitted photon has higher energy than the incident. This phenomenon occurs when the molecule is originally excited and relaxes to a lower energy state.
- *Stokes scattering*: the emitted photon has lower energy than the incident one.

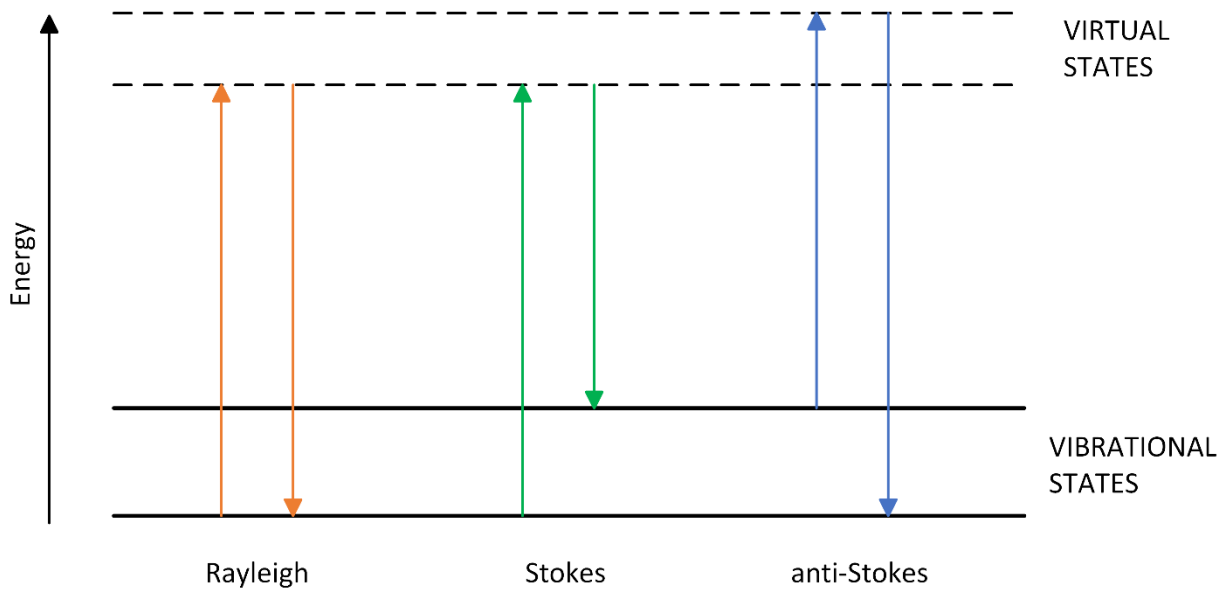

Figure 7: Energy diagram of the Rayleigh, Stokes, and anti-Stokes scattering processes.

The intensity of Raman scattering I_R is given as [19], [20]:

$$I_R \alpha \, \nu_{inc}^4 I_0 n \left(\frac{\partial \alpha}{\partial Q}\right)^2 \tag{1.57}$$

Where ν_{inc} is the frequency of the incident radiation, n is the number of scattering molecules in a given state, α is the molecule polarizability and Q is the vibration amplitude.
Due to its nature, which requires vibrational modes to be available within the molecule, the intensity of anti-stoke scattering is dependent on the temperature. In fact, the relative intensity of the anti-Stokes and Stokes scattering is given as [17]:

$$\frac{I_{AS}}{I_S} \alpha \exp\left(-\frac{h\nu_{inc}}{k_B T}\right) \tag{1.58}$$

Where I_{AS} is the anti-Stoke intensity, I_S is the Stoke intensity, k_B is the Boltzmann's constant and h is the Planck's constant.
The Raman scattering by a generic molecule can be described through the Raman tensor $\boldsymbol{A}_R$, that expresses the relationship between the exciting field $\vec{E}_0$ and the scattered field $\vec{E}_R$ [21]:

$$E_R = \boldsymbol{A}_R \, \vec{E}_R = \begin{bmatrix} \alpha_{xx} & \alpha_{xy} & \alpha_{xz} \\ \alpha_{yx} & \alpha_{yy} & \alpha_{yz} \\ \alpha_{zx} & \alpha_{zy} & \alpha_{zz} \end{bmatrix} \begin{bmatrix} E_{Rx} \\ E_{R_y} \\ E_{Rz} \end{bmatrix} \tag{1.59}$$

Where E_{Rx}, E_{Ry} and E_{Rz} are the cartesian components of $\vec{E}_R$ vector.
Scattering phenomena are generally of weak intensity. Indeed, Rayleigh and Raman's scattering have scattering cross-sections of 10^{-3} and $10^{-6} - 10^{-7}$ respectively. This very low cross section makes the application of Raman spectroscopy for the study of molecules in low concentrations difficult. To overcome this limitation and fully exploit the versatility of Raman spectroscopy, a novel technique named *Surface Enhanced Raman Spectroscopy (SERS)* was introduced in 1974 by Fleischmann [22] who studied the Raman spectra of pyridine adsorbed on a roughened silver film.
Although in this first work, the Raman signal enhancement was attributed to a higher amount of molecule that can be adsorbed on a rough surface, it was later concluded by Van Duyne [23] and Creighton [24] that it was the result of an increase of the Raman cross-section. They both observed that the enhancement factor due to the increased specific surface area introduced by the roughening should have been lower. In contrast, they observed values of several orders of magnitude higher.
In particular, Van Duyne measured a SERS enhancement factor of 10^5 for a pyridine molecule on a silver substrate and suggested the interaction of the Raman vibrational modes with the surface plasmon of the metal.

Over the years, in many works, it has been assumed that the SERS enhancement factor SEF is proportional to the fourth power of the field enhancement factor, but a rigorous proof was published only in 2006 by Le Ru et al. [25].

$$SEF = \left|\frac{\vec{E}_L}{\vec{E}_0}\right|^4 \tag{1.60}$$

Where $\vec{E}_L$ is the electric field localized on the surface of the metal structure and $\vec{E}_0$ is the electric field of the incident radiation.
In particular, Le Ru identified two main electromagnetic contributions to the SERS effects: a first term M_L due to the localization of the electric field close to the metallic surfacen and a second one M_{rad} which is related to the increase of the radiated power by Raman scattering.

$$SEF = \beta M_L(\omega_0) M_{rad}(\omega_R) \tag{1.61}$$

Where β is a constant whose value is usually close to 1. The field E_L l oscillates at ω_0 and induces a Raman dipole of momentum $\vec{d} = \alpha\, \vec{E}_L$ oscillating a frequency ω_R. Considering an isotropic Raman tensor:

$$M_L = \left|\frac{\vec{E}_L}{\vec{E}_0}\right|^2 \tag{1.62}$$

For a similar reason, also the field $\vec{E}_R$ emitted by the Raman dipole oscillating at the frequency is enhanced by field localization on the particle surface.
The SEF can be therefore expressed as product of two enhancement terms; one at the incident frequency ω_0 and the other referred to the Raman frequency ω_R, namely:

$$SEF = \left|\frac{\vec{E}_L(\omega_0)}{\vec{E}_0}\right|^2 \left|\frac{\vec{E}_L(\omega_R)}{\vec{E}_0}\right|^2 = \left|\frac{\vec{E}_L(\omega_0)}{\vec{E}_0}\right|^2 \left|\frac{\vec{E}_L(\omega_0 + \Delta\omega_R)}{\vec{E}_0}\right|^2 \tag{1.63}$$

But since the value of Raman shift is typically small if compared to the incident frequency (it is usually limited to $3000\ cm^{-1}$), in a first approximation (1.63) can be rewritten as:

$$SEF \approx \left|\frac{\vec{E}_L(\omega_0)}{\vec{E}_0}\right|^4 \tag{1.64}$$

However, SERS spectra are not particularly easy to be handled. Concerning normal Raman spectra, SERS spectra may contain bands that are usually not visible, or some others can also

become extremely weak and disappear. Moreover, the intensity of bands is usually not a linear function of the concentration.

Chapter 2
FUNDAMENTALS ON OPTICAL PROPERTIES OF METALS AND SURFACE ENHANCHED RAMAN SPECTROSCOPY

This chapter is largely based on the research paper *Synthesis of tailored nanostructured gold surfaces for SERS applications by controlled seed deposition and growth* [26], first-authored by the author of the present thesis.

Gold nanoparticles (Au NPs) are commonly employed in a plethora of different applications[27], including the development of catalysis, electronics, medical and sensing devices. Among the other applications, Au NPs are widely used to prepare surface-enhanced Raman spectroscopy (SERS) and surface-enhanced infrared spectroscopy (SEIRA) sensors. The fabrication of such sensors can be achieved by different techniques, including the deposition of gold nano seeds on a functionalized substrate and their subsequent growth. Usually, the deposition is performed onto glass, quartz, or silicon substrate that is functionalized with an organosilane exposing a $-NH_2$ or -SH group[28], [29] , which is able to chemically bind to gold seeds. The substrate is then immersed in a gold nanoparticle colloidal suspension for a certain time, and particles reaching its surface by diffusion remain bonded to the silane.

The growth of the seed is usually obtained by the reduction of a gold precursor, typically tetrachloroauric acid ($HAuCl_4$), with a reducing agent such as ascorbic acid [30] or hydrogen peroxide [31]. This method allows isotropic growth to be obtained, leading to spherical nanoparticle production. However, the addition of some proper capping agent is possible to obtain anisotropic nanostructures such as arrays of nanostars[32], nanorods[33] or forests of nanowires[34].

It was demonstrated that the performance of the SERS sensors is strongly influenced by the surface coverage factor[35], size of the particles and their center-to-center distance[36], [37]. For this reason, the possibility of accurately controlling the seed deposition onto the functionalized substrate is of utmost importance to preparing highly optimized sensors[38].

This chapter describes a novel approach for fabricating a uniform and optimized SERS substrate. Such optimization starts from estimating the geometry that maximizes the SERS signal for a given analyte Raman band at a certain excitation wavelength using Boundary Element Method (BEM) simulation.

A Monte Carlo simulation is subsequently used to determine the process conditions to functionalize the substrate by nanoparticle seed deposition and to achieve the optimal center-to-center particle distance previously studied.
The deposited particles are grown by a seed-mediated chemical reeduction of a gold precusor until particles touch and form dimers, providing a suitable optical response for SERS measurement at 785 nm. The final deviced has been tested for the detection of skatole obtaining very exciting results such as a limit of detection as low as 0.32 nM.

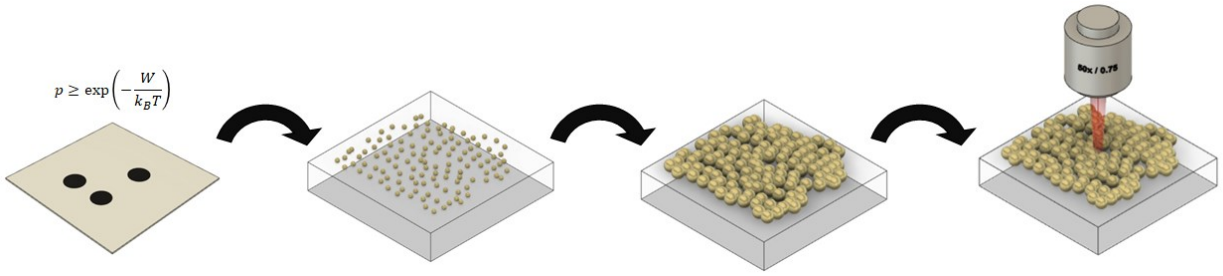

Figure 8: Fabrication process of SERS substrates from ERSA simulation to deposition of seed gold nanoparticles, and subsequent controlled growth to obtain SERS hotspots.

2.1 DESIGN AND OPTIMIZATION OF THE SUBSTRATE VIA BEM SIMULATION

In gold NPs arrays, the enhancement of the SERS signal is mediated by the field intensity amplification provided by the localized surface plasmon resonances (LSPRs) residing in the gold nanostructures, especially in the gaps or grooves (hotspots).
To enhance the response of a flat substrate and control the uniformity of the distribution of the hotspots for better sensor reliability, we turned to a controlled deposition of seed Au NPs and subsequent electroless growth of the seeds. We started from the SERS sensor's optical requirements, assuming a random distribution of various gold spherical nanoparticles with different lateral distances representing the randomly deposited NP seeds. Assuming uniform growth for each seed, we can consider the fundamental element of such SERS sensors to be a gold dimer unit with radius a and center-to-center separation distance d, as illustrated in Figure 1.
The far- and near-field properties of particle dimers in a vacuum are simulated by using the boundary-elements method (BEM) available through the Matlab-based tool MNPBEM[39]. The dimer is excited by normal-incident plane wave radiation whose polarization is directed along the dimer axis. Optical data for gold is taken from Johnson and Christy.
To take into account the field-enhancement properties of the dimer, the Surface Averaged Enhancement Factor (SAEF) was calculated as the mean over the dimer surface Σ of the square modulus of the normalized electric field $\frac{E(\lambda)}{E_0}$.

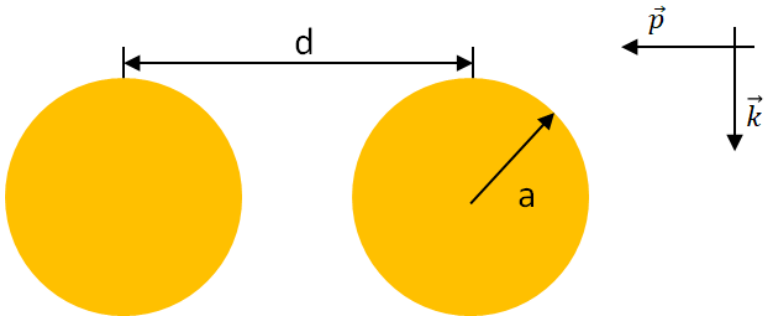

Figure 9: Schematic of the gold nanoparticle dimers and plane-wave characteristics adopted in simulations. $\vec{k}$ and $\vec{p}$ are the wavector the and the polarization vector of the incident field, respectively.

$$SAEF(\lambda) = \frac{1}{\Sigma}\oint_{\Sigma}\left|\frac{E(\lambda)}{E_0}\right|^2 d\Sigma \tag{2.65}$$

Moreover, to better compare the SERS response of different dimer systems, a SERS Enhancement Factor (SERSEF) was defined as the product between the SAEF at the laser exciting wavelength λ_{EXC} (785 nm) and the SAEF at a wavelength $\lambda_{EXC} + \Delta\lambda_{RS}$ corresponding to a Raman shift $\Delta\lambda_{RS}$:

$$SERSEF(\lambda_{EXC}, \Delta\lambda_{RS}) = SAEF(\lambda_{EXC}) \cdot SAEF(\lambda_{EXC} + \Delta\lambda_{RS}) \tag{2.66}$$

The dimer was excited with a plane wave propagating downward along the vertical direction and linearly polarized along the dimer axis. The dimer was assumed to be placed in vacuum (n=1).
Figures 2a-f present the extinction cross-sections as a function of the wavelength and the particle radius for such gold dimers with different center-to-center separation distances, ranging from 40 nm to 100 nm. For all the center-to-center distances, an abrupt change in the extinction spectra can be observed when the two spheres approach each other. This is a consequence of the classical electromagnetic model we are using. Note that this phenomenon is a quantum effect due to electron smearing and tunneling between two spheres in the nearly touching regime (sub-nanometer gaps). In this thesis we neglected such a nonlocal effect, as it is impossible to control the diameter of grown nanoparticles with such atomic-scale precision. A redshift of the resonance can be seen for touching dimers of larger sizes.
Correspondingly, as shown in Figure 11a-f), the surface-averaged near-field intensity enhancement peak follows the extinction peak trend, the maximal value of which can be above 10^3 when the two spheres are just touching. As the particles continue to grow, the dimers start resembling larger oblate spheroidal nanoparticles, and a blueshift of the extinction peak is therefore observed. As a result of the field intensity enhancement provided by those gold dimers,

we find that, for an excitation wavelength of 785 nm, the surface-averaged SERSEF can be amplified to a value of nearly 10^8 for a dimer of a = 30 nm and d = 62 nm, as shown in Figure 12. More generally, we observed that this dimer exhibits a SERSEF higher than 10^6 for all the Raman shifts in the range from 100 to 2500 cm^{-1}. When the center-to-center separation distance d increases to 80 nm (Figure 12 e), the SERS signal gets weaker due to the field intensity enhancement degradation, as shown in Figure 11e. Analogously, if the center-to-center distance is decreased to 40 nm Figure 12 a) the SERSEF will decrease and achieve values lower than 10^4.

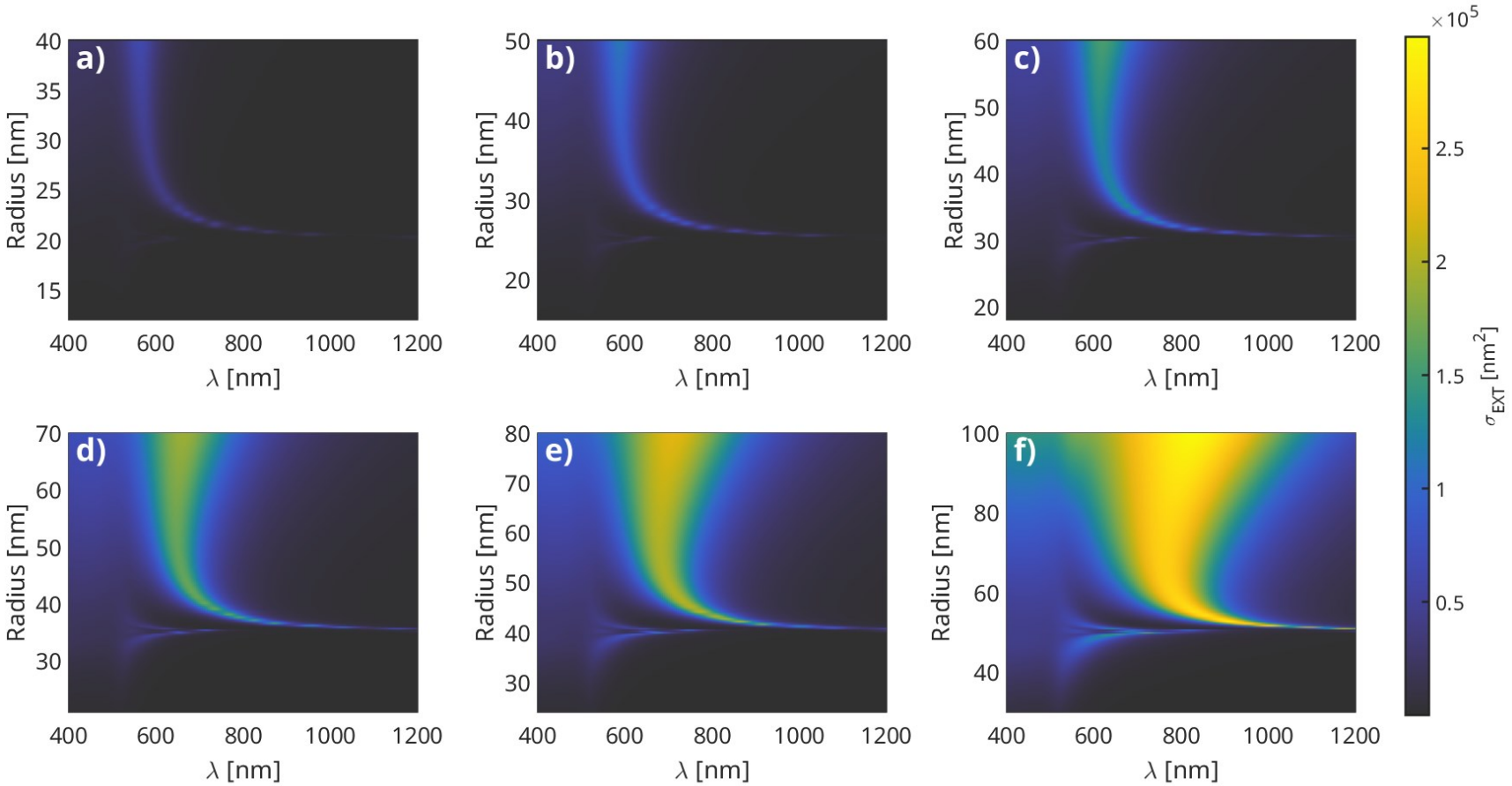

Figure 10: Calculated extintion cross section as a function of the particle radius and wavelength for dimers at different center-to-center separation distances: (a) 40 nm, (b) 50 nm, (c) 60 nm, (d) 70 nm, (e) 80 nm and (f) 100 nm.

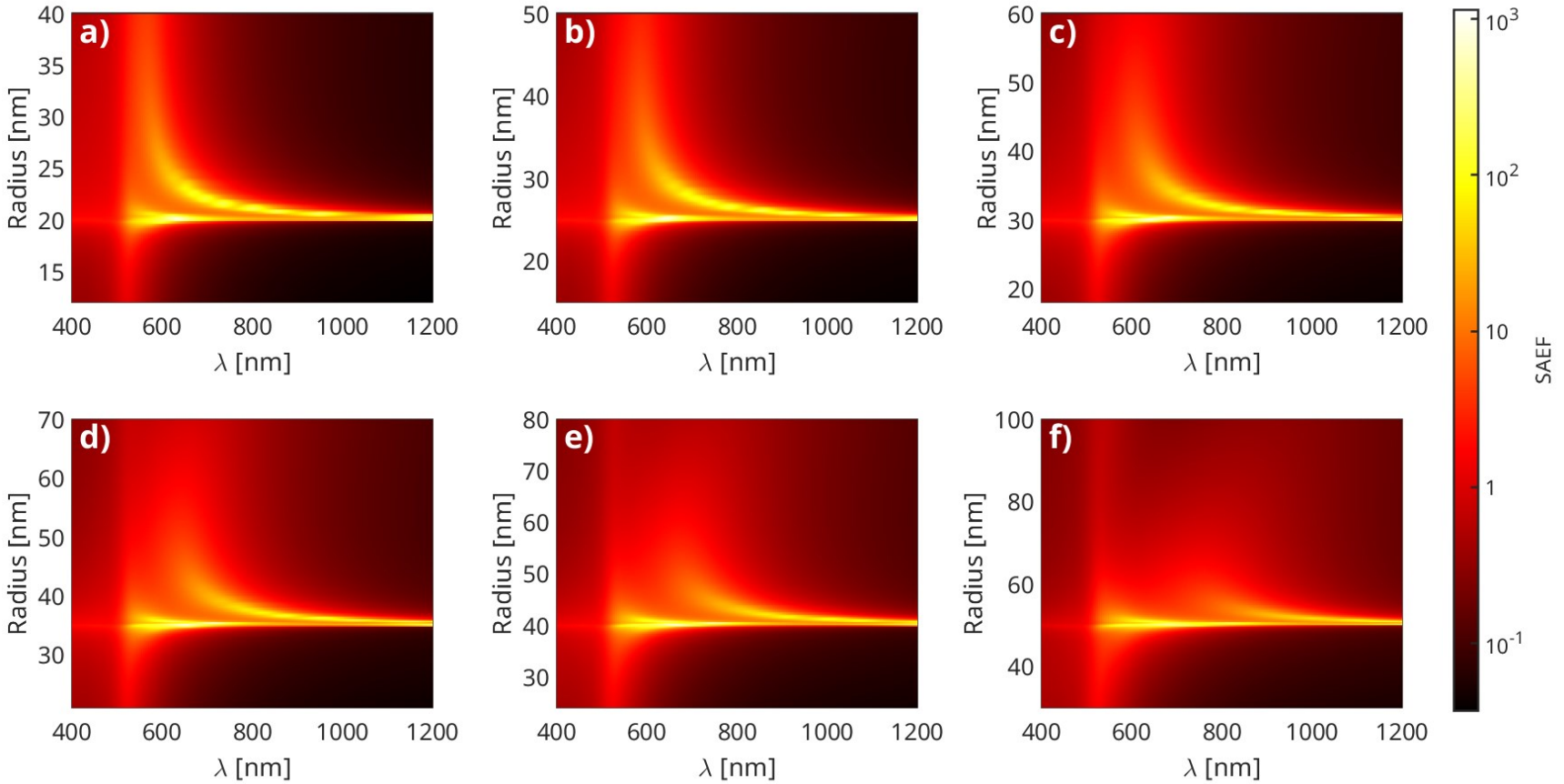

Figure 11: Calculated Surface Averaged Enhancement Factor as a function of the particle radius and wavelength for dimers at different center-to-center separation distances: (a) 40 nm, (b) 50 nm, (c) 60 nm, (d) 70 nm, (e) 80 nm and (f) 100 nm.

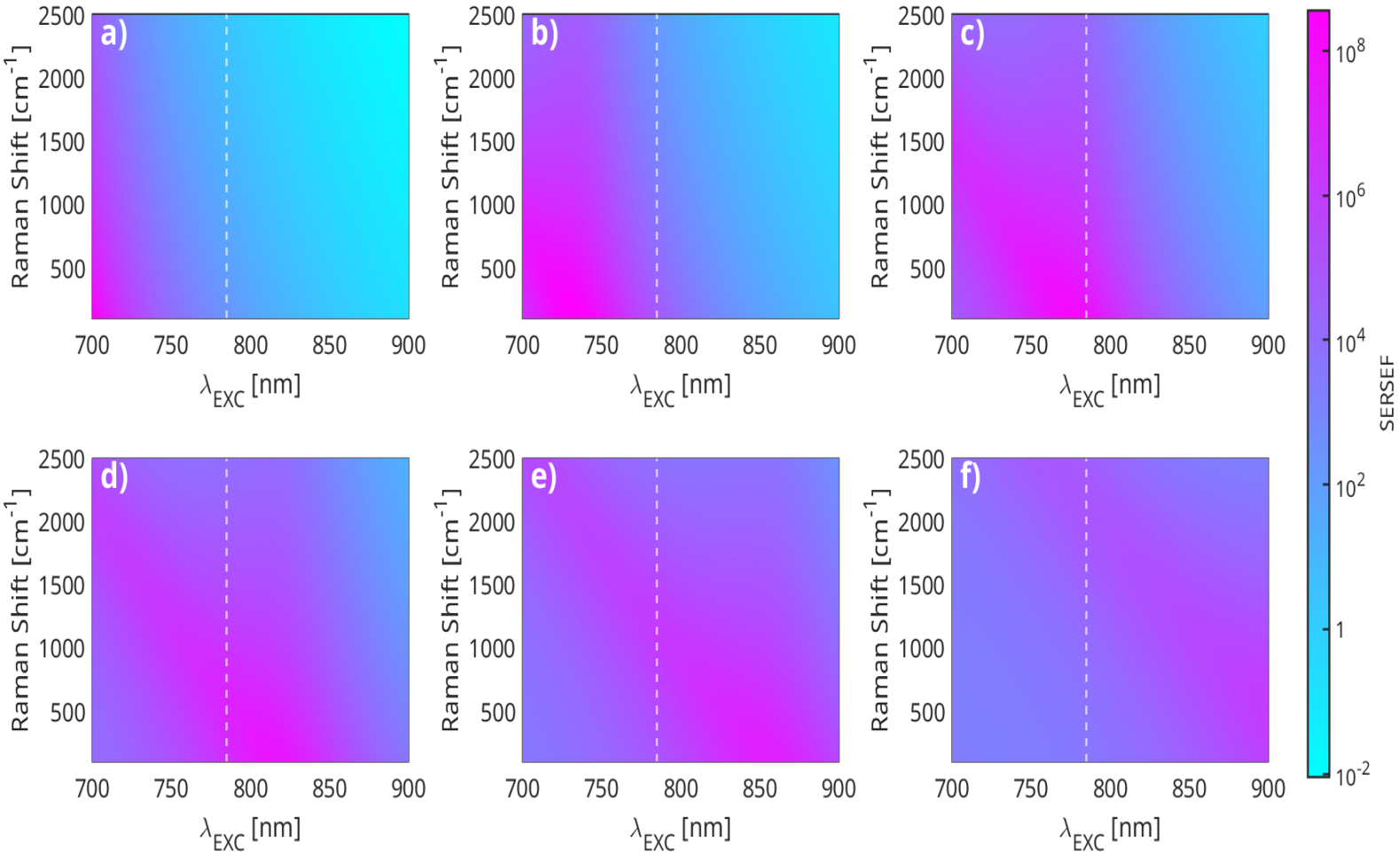

Figure 12: Calculated SERS Enhancement Factor as a function of the particle radius and Raman Shift for dimers at different center-to-center separation distances: (a) 40 nm, (b) 50 nm, (c) 60 nm, (d) 70 nm, (e) 80 nm and (f) 100 nm. The white dashed line indicates the chosen Raman excitation wavelength, i.e. 785 nm.

2.2 SUBSTRATE CLEANING AND FUNCTIONALIZATION

Assuming a certain distribution in the center-to-center distances between the seed NPs requires a tight control of the deposition process.
Gold seeds are deposited onto a glass substrate after functionalization with an appropriate molecule thant can bind to the metal and, at the same time, ensure the adhesion of the particles.
In the frame of this work, two alkoxysilane molecules are tested for this purpose, namely (3-aminopropyl)triethoxysilane (APMTS) and (3-Trimethoxysilyl-propyl)diethylene-triamine (DETA). The chemical structures of APTMS and DETA molecules are reported in Figure 13.

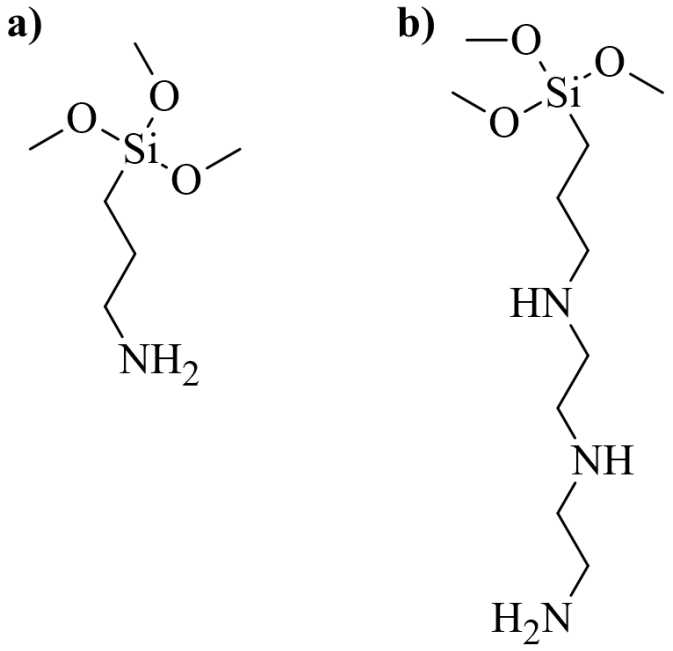

Figure 13: Chemical structures of the APTMS a) and DETA b).

As can be observed from the chemical structures, both APTMS and DETA contain a silane group that can undergo a condensation reaction with the -OH groups of the glass surface, forming a stable covalent bond[40].
This process will produce a glass surface that exposes alkyl chains containing -NH groups that form an adhesion layer with strong affinity for gold[41].
The first step towards such control is the characterization and control of the surface properties of the substrate where the seed deposition will occur. To this aim, we evaluated the impact of the cleaning procedures and functionalization on the surface zeta potential.
Different cleaning and hydroxylation techniques to prepare the glass substrate for silane functionalization are available and already used by different authors. In our work, we investigated the effect of three different cleaning procedures, i.e. oxygen plasma cleaning and treatment with acid and basic Piranha solution, on the surface properties of the glass. The zeta-potential curves,

obtained with an Antoon Paar Surpass 3 zeta potential titration, in the pH range from 2 to 10 are reported in Figure 14.

Acid piranha solution was prepared by slowly adding 3 mL of 30 %wt. hydrogen peroxide to 9 mL of sulfuric acid 98%. Basic Piranha solution was prepared by diluting 10 mL of 33% wt. ammonium hydroxide with 14 mL of water and slowly adding 2 mL of 30 %wt. hydrogen peroxide. Whereas the acid Piranha solution developed a strong exergonic reaction which cause the temperature to rise above 50°C, basic Piranha must be heated up to 60°C to sustain its reactivity.

The acid piranha solution is known to be an extremely strong oxidizer and will hydroxylate the surface by increasing silanol groups Si-OH and lowering the surface contact angle. It was observed that treating silicon dioxide with an oxygen plasma can lower its CA to about 55°[42], whereas the treatment in Acid Piranha can bring this value as low as 36.4°[43]. This, with any probability, is related to a higher density of Si-OH groups within the substrate in the piranha-treated samples.

Since the zeta-potential curves appear very similar and considered the safety concerns in using the acid piranha solution, we adopted a cleaning procedure based on basic piranha solution for the rest of this work.

The differences in the zeta-potential curve are also analyzed after the functionalization with APTMS. One may observe the plasma cleaned functionalized shows the isoelectric point (IEP) which is almost 2 pH unit lower than the piranha treated sample. Since the Au NPS are usually supplied and are most stable at pH around 6.5-7, the plasma-treated sample is not a good choice since it will be negatively charged and will repel particles during the deposition step.

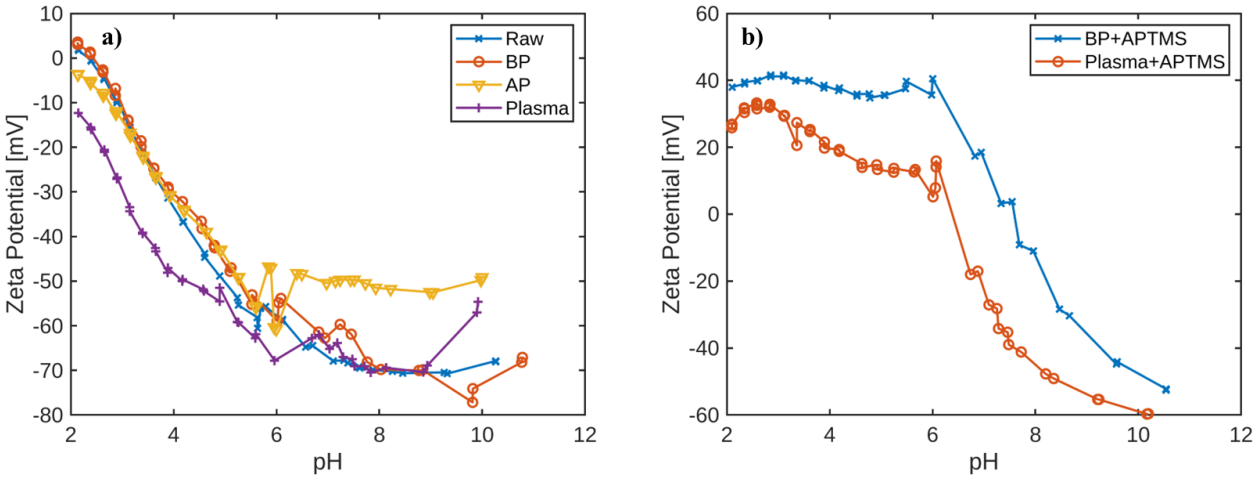

Figure 14: Zeta-potential as a function of the pH for the clean glass substrate (a) and for the same substrate after functionalization (b). BP and AP refers to Basic Piranha and Acid Piranha cleaning treatment respectively.

Since the deposition of a few nm NPs might be affected by roughness on a comparable scale, we tested the effect of the different treatments on the surface roughness. The results are reported in

Figure 15 and Table 2. In conclusion, we adopted a cleaning procedure based on basic piranha before the functionalization to have a surface that is better suited for the deposition of Au seeds.

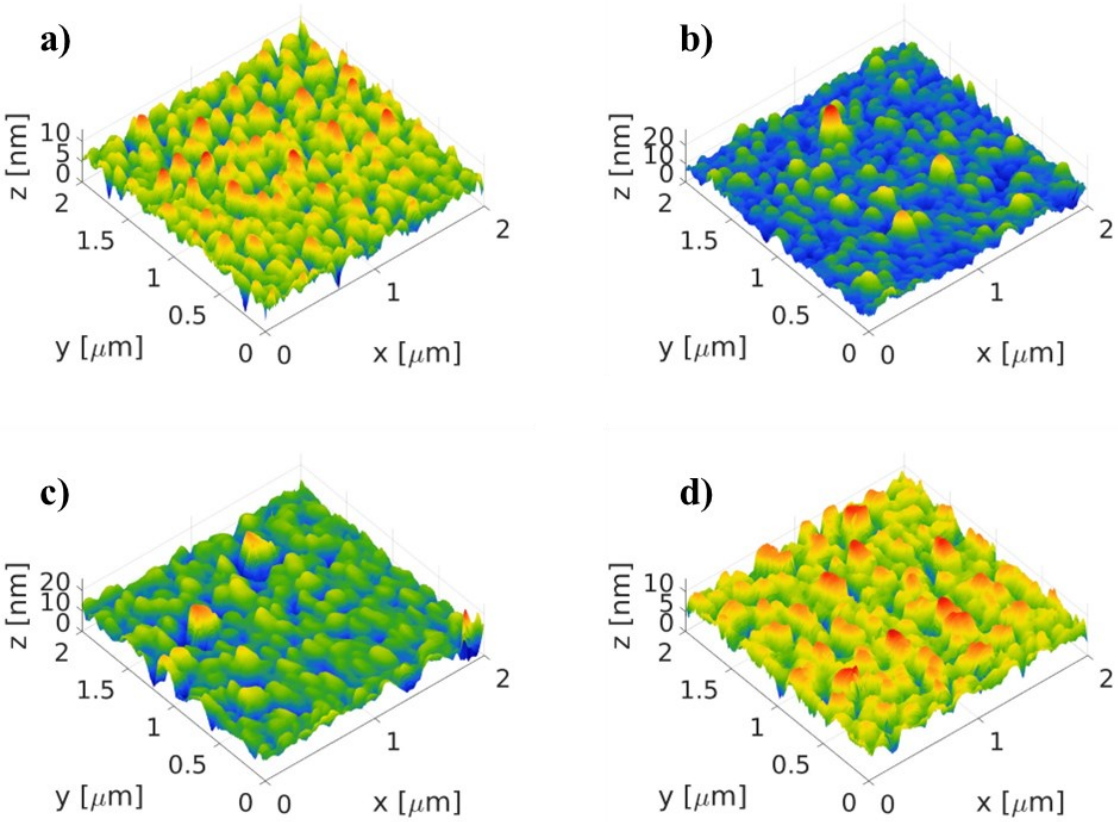

Figure 15: AFM measurement of soda-lime glass after different cleaning procedures: (a) ultrasounds, (b) oxygen plasma, (c) acid Piranha and (d) basic Piranha.

Cleaning Treatment	R_a $[nm]$	$R_q[nm]$	IEP $[mV]$
Ultrasound	1.29	1.64	2.35
Oxygen Plasma	2.07	2.78	2.41
Basic Piranha	1.34	1.71	2.03
Acid Piranha	1.79	2.43	1.54

Table 2: Effect of different cleaning treatment on the substrate surface roughness and isoelectric point.

2.3 NANOPARTICLES CHARACTERIZATION

To develop a simulation model to study and control the deposition of gold nanoparticles from a colloidal suspension onto a functionalized charged substrate, a thorough characterization of the colloidal NPs, apart from the surface characterization presented in the previous section, is required. Indeed, the fundamental parameters of such simulation are the particle size distribution, density, and zeta potential of the colloidal suspension.

In this work, we employed highly monodispersed gold nanoparticles supplied in a citrate buffer with a proprietary stabilizer surfactant based on tannic acid. Although nanoparticles in ultrapure water were also available, we opted for the stabilized type as it is less prone to aggregation in the solution and maintains its stability for longer.

Average size and particle concentration were obtained from the UV-VIS spectra following the Haiss procedure[44]. In particular, the particle diameter d can be obtained as:

$$d = \exp\left(3\frac{A_{spr}}{A_{450}} - 2.2\right) \tag{2.67}$$

Where A_{spr} is the absorbance at the maximum of the plasmonic resonance peak and A_{450} is the absorbance at 450 nm. Moreover, the particle concentration per unit volume N is given by the following equation:

$$N = \frac{A_{450} \cdot 10^{14}}{d^2\left[-0.295 + 1.36\exp\left(-\left(\frac{d - 96.8}{78.2}\right)^2\right)\right]} \tag{2.68}$$

The value A_{450} is dependent on the optical path length, which, in the fitting equation (2.68), is assumed to be equal to standard value of 1 cm.

The UV-VIS spectra were collected with a Shimadzu UV-2600i in the range from 300 to 900 nm, using a 70 µL PMMA microcuvette and are shown in Figure 16.

Hydrodynamics radius a_H and Zeta potential ζ_P distribution were measured with a Dynamic Light Scattering (DLS) Malvern Zeta Sizer nano equipped with a 633 nm He-Ne laser. Optical data for gold at 633 nm for DLS measurement were obtained from Johnson and Christy[7].

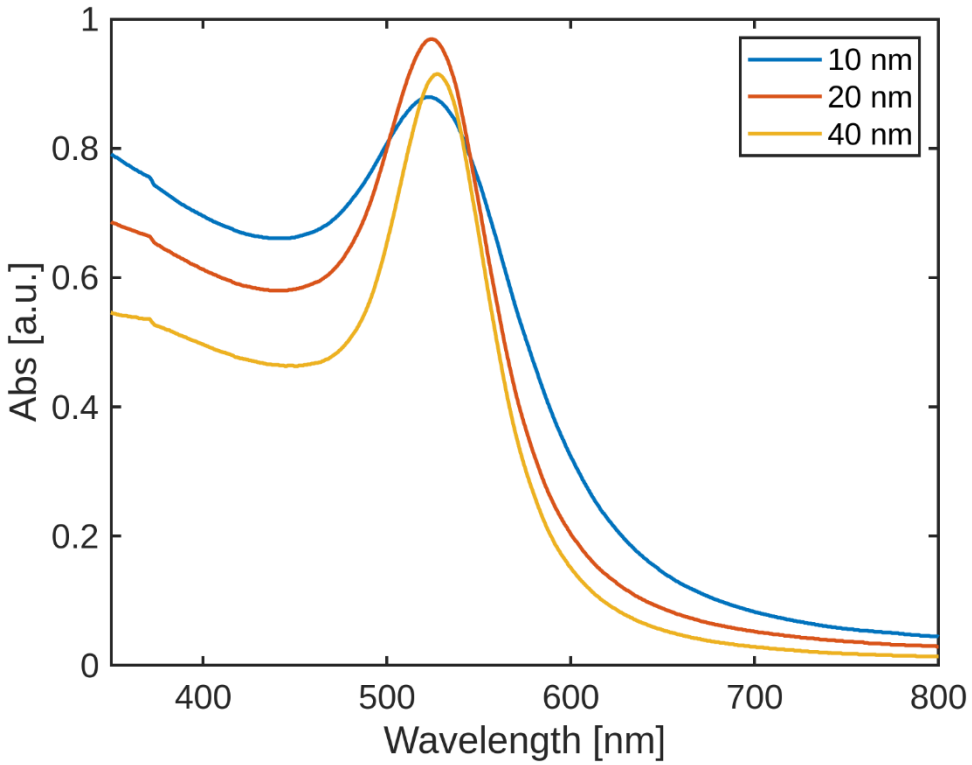

Figure 16: UV-VIS of the gold nanoparticle colloidal suspensions of different particle diameters.

Nominal diameter $[nm]$	a_H $[nm]$	$\zeta_P [nm]$	C_0 $[10^{12}\ mL^{-1}]$
10	7	-47.9	5.98
20	12	-50.8	0.65
40	22	-40.5	0.07

Table 2: Properties of the colloidal suspension of nanoparticles of different nominal diameters as provided from the supplier.

2.4MODELING AND SIMULATION OF NANOPARTICLE SEEDS DEPOSITION

Eklof et al.[45] studied the deposition process of gold nanoparticles onto a functionalized quartz substrate using a Monte Carlo simulation. In his work, largely based on the Random Sequential

Adsorption (RSA) method[46], [47], each particle is randomly placed at a position within the substrate, adsorbed if an adsorption condition is fulfilled and rejected otherwise.
The absorption condition assumes that each particle cannot overlap with any other and considers an adsorption probability related to the repulsion potential with the adjacent particles.
This approach is based on a two-body interaction, i.e., particle-particle interaction[48], and does not take into account that the functionalized substrate has its own surface charge and can strongly influence the deposition process.
Cahill et al.[49] studied the adsorption of Poly(amido amine) (PAMAM) Dendrimers on a silica substrate by a three-body interaction approach and underlined the effect of the charged substrate on the deposition process. In particular, they observed that the charged substrate causes the accumulation of an excess of counterions in the proximity of its surface and therefore the Debye's length is locally reduced with respect to the bulk of the colloidal suspension.
This Debye's length near the charged surface is named *effective Debye's length* κ_{eff} and defines as:

$$\kappa_{eff} = \kappa \cosh\left(\frac{e\zeta_S}{k_B T}\right) \tag{2.69}$$

Where κ is the Debye's length in the colloid bulk, $e = 1.6002 \cdot 10^{-19} C$ is the charge of the electron, ζ_S is the zeta-potential of the charged substrate, k_B is the Boltzmann's constant and T is the absolute temperature.
They also derived the interaction potential of two particles W_{pp} in the proximity of the charged substrate as:

$$W_{pps} = \frac{Z^2}{4\pi\varepsilon_0\varepsilon_w}\left[\frac{\exp(k_{eff}a)}{1+k_{eff}a}\right]\frac{\exp(-k_{eff}a)}{d} \tag{2.70}$$

Where Z is the surface charge, ε_0 is the vacuum dielectric constant, ε_W is water permittivity, is particle radius radius, and d is the distance between the two particles.
They assumed the zeta potential of the substrate to remain constant throughout the deposition. However, it is easy to imagine that the deposition of negatively charged nanoparticles onto the positively charged substrate will decrease its total surface charge and, therefore, its zeta potential.
This work focuses on the development of an improved interaction model, named *Self Limitating Extended Random Sequential Adsorption (SLERSA)*, for the study of gold nanoparticle deposition onto a charged functionalized substrate and its experimental validation (see Figure 18 for a flowchart of the implementation).
Given a substrate of total surface area W and colloidal suspension of particles with radius a and concentration C_0 the number of particles that arrives at the surface in a time t by diffusion are given as[50], [51]

$$N = WC_0\sqrt{\frac{k_BT}{12\pi\eta a}t} \tag{2.71}$$

Where η is the viscosity of the colloidal suspension solvent, which in the case of water is equal to $10^{-3}\ Pa \cdot s$.

The simulation iterates N times by randomly selecting a point of coordinates (x_i, y_i) within the area of the substrate for each iteration. For each point, the simulation verifies whether there is overlapping with an adjacent particle, in which case the adsorption is immediately rejected. If there is no overlapping, the interaction energy between a particle located in (x_i, y_i) and the N particles located in its neighbor is given according to the following expression:

$$W_{p,i} = \sum_{j=1}^{N} \frac{Z^2}{4\pi\varepsilon_0\varepsilon_w}\left[\frac{\exp(k_{eff}a)}{1+k_{eff}a}\right]\frac{\exp[-k_{eff}(d_{ij}-2a)]}{(d_{ij}-2a)} \tag{2.72}$$

Where Z is the total charge of the spherical nanoparticles, which can be calculated from its zeta potential, following the first-order approximation of the spherical Poisson-Boltzmann equation introduced by Ohshima et al.[52]:

$$Z = 4\pi a^2\sigma_{pe}\frac{4\pi a^2\varepsilon_0\varepsilon_R k_BT\kappa}{e}f(y_s)\left[1+\frac{2}{\kappa a f^2(y_s)}\int_0^{y_s} f(y)dy\right] \tag{2.73}$$

Where $f(y)$ is defined as:

$$f(y) = sgn\ (y)\frac{\sum^i c_i^0[\exp(-z_i y)-1]}{\sum^i c_i^0 z_i^2} \tag{2.74}$$

and $y(\zeta_P)$ is a function of the particle zeta potential ζ_P referred to as the reduced zeta potential

$$y(\zeta_P) = \frac{e\zeta_P}{k_BT} \tag{2.75}$$

A random number p from 0 to 1 is selected according to a uniform distribution. If the reduced interaction potential $\frac{W_{pp}}{k_BT}$ is greater than p, the adsorption is accepted otherwise it is rejected.
At each iteration, if the adsorption is accepted, the effective charge of the substrate is calculated as a function of the number of adsorbed particles by a charge superposition principle:

$$\sigma_{eff} = \sigma_s + \frac{4\pi a^2 N}{A_s}\sigma_P = \sigma_s + 4\theta\sigma_P \tag{2.76}$$

Where σ_S and σ_P is the surface charge density of the flat substrate and of a particle, respectively, N is the number of particles deposited onto a given substrate area A_s and $\theta = \frac{\pi a^2 N}{A_s}$ is the surface coverage factor.
The effective zeta potential is therefore obtained by solving numerically (2.73) [53] and used to calculate the effective Deybe's length κ_{eff}:

$$\zeta_{eff} = \sqrt{\frac{2\varepsilon_0 \varepsilon_R k_B T \kappa}{N_A} \sum^{i} c_i^0 \exp\left[\left(\frac{-z_i e \zeta_{eff}}{k_B T}\right) - 1\right]} \tag{2.77}$$

From the particle coordinates obtained by the Monte Carlo simulation, the Nearest Neighbor Distribution (NND) g_{NN}can be calculated as:

$$g_{NN}(r, \delta r) = \frac{1}{N} \sum_{i=1}^{N} \lambda_i(r, \delta r) \tag{2.78}$$

where N is the total number of particles and λ_i is equal to 1 if the distance between the i−th particle and its nearest neighbor lies between r and r+δr or 0 otherwise, namely:

$$\lambda_i(r, \delta r) = \begin{cases} 1, & r \leq \left|\vec{x}_i - \vec{x}_{NN}\right| < r + \delta r \\ 0, & \text{otherwise} \end{cases} \tag{2.79}$$

The average value $\langle d_{NN} \rangle$ of the center-to-center distribution was determined as the center of the fitting Gaussian of the near neighbor distribution g_{NN}:

$$D_{fit}(x) = \exp(-\frac{(x - x_0)^2}{2\sigma^2}) \ for \ x \geq x_0 \tag{2.80}$$

The distributions for the three particle diameters employed in this work are reported in Figure 17 together with their fitting Gaussians. It can be observed that, using the 10 nm seed, a nearest neighbor average distance of 53 nm can be obtained, which is very close to the optimal value of 60 nm identified with the optical response simulation. At the same time, we can conclude that using higher diameter seeds leads to a much higher average distance, i.e., 86 nm for the 20 nm seeds and 148 nm for the 40 nm seeds.
This huge difference may be due to the larger particles and the associated lower concentration typically found in stock NP. Higher particle densities could be obtained by increasing the deposition time although the deposition times can reach hundreds of hours. Using higher

concentration solution of NP is not advisable as the stability of the colloid may be lowered and particle aggregation may occur during the deposition stage.
As a conclusion of the theoretical and experimental results obtained so far, the 10 nm gold seed was selected for the sensor fabrication, as discussed in the next section.

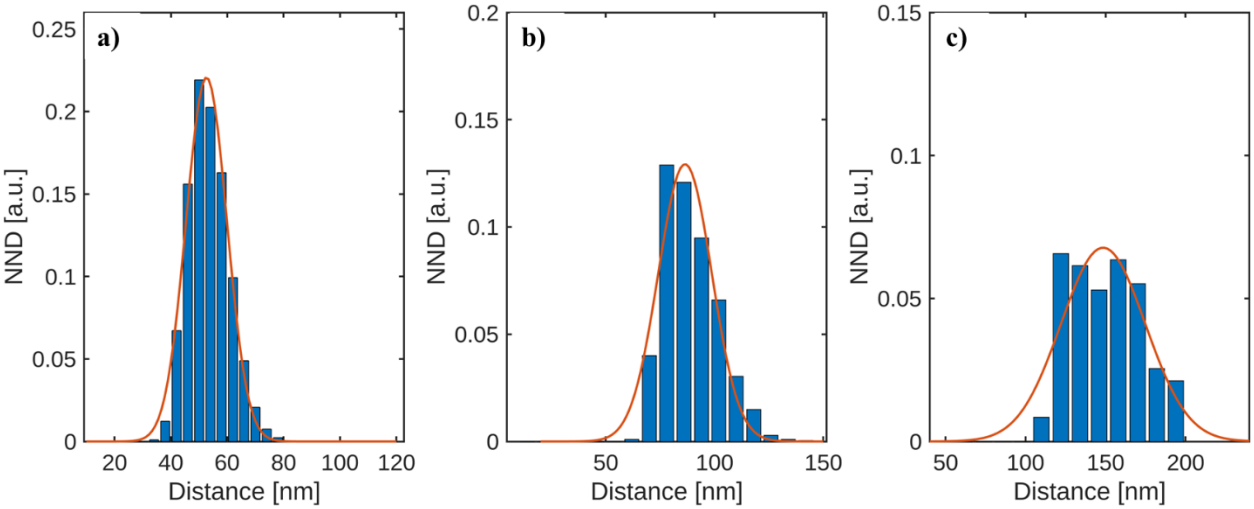

Figure 17: Nearest neighbor distribution of gold nanoseed of different diameters deposited on the functionalized glass: a)10 nm, b) 20 nm and c) 40 nm. The red line represents the least square fitting gaussian.

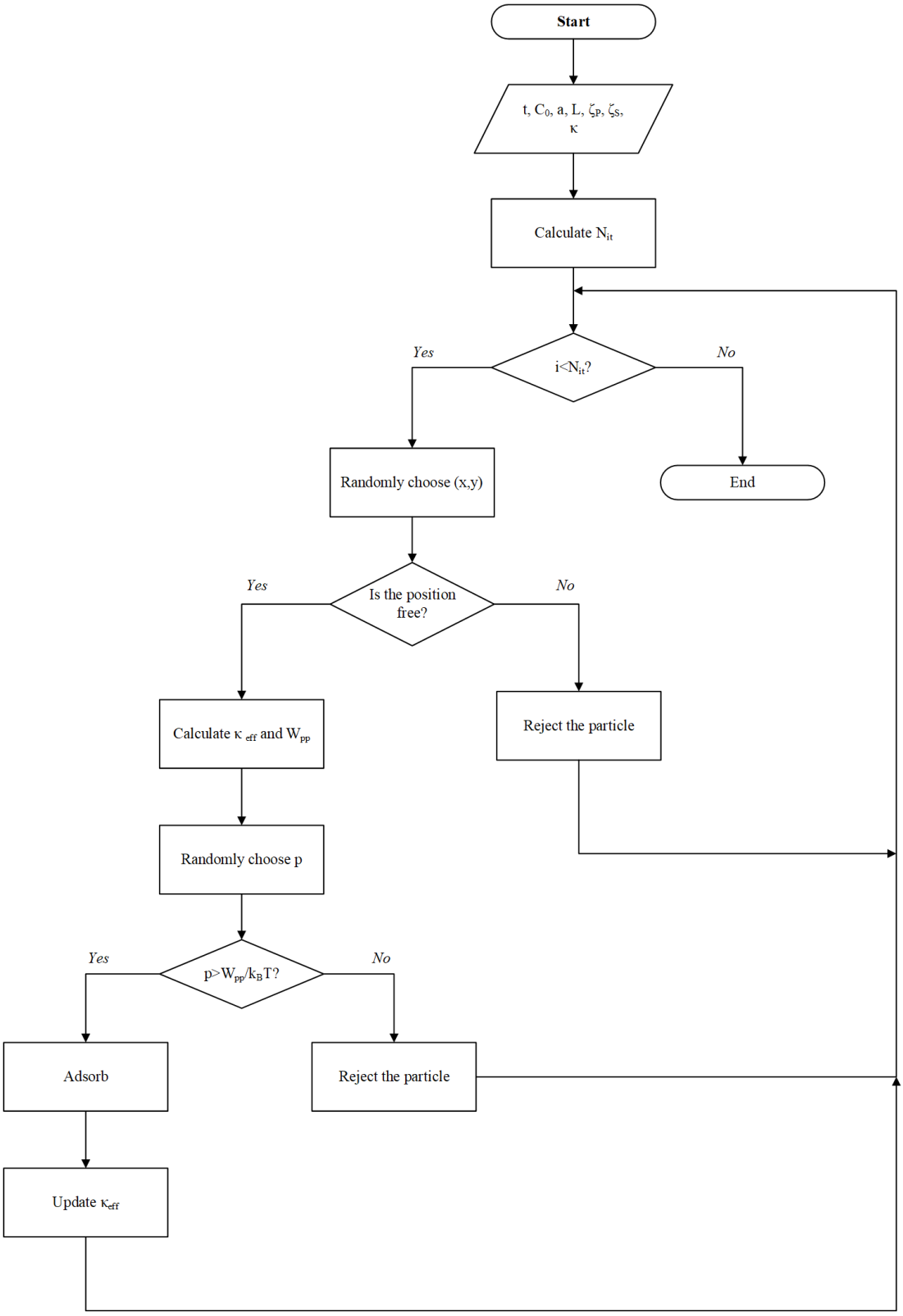

Figure 18: Flowchart of the Monte Carlo algorithm for the study of the nanoseed deposition on the functionalized substrate.

2.5 SEED-MEDIATED GROWTH AND OPTICAL RESPONSE MEASUREMENT

The APTMS functionalized substrates were placed in a polytetrafluoroethylene (PTFE) holder and immersed in a colloidal suspension of the 10 nm gold nanoparticles overnight. After such a long deposition time, we can conclude that the surface is saturated and no other particles can be accommodated.

Subsequently, those seed nanoparticles were grown by reduction of tetrachloroauric acid in the presence of hydrogen peroxide. In particular, the substrates were immersed in a 0.28 mM $HAuCl_4$ solution, and 525 mL of 30% H_2O_2 were added under magnetic stirring at 300 rpm. After a certain growth time, the substrate was removed twice in ultrapure water and once in ethanol. SEM images of particles obtained at different growth times are reported in Figure 19: SEM images of the particles growth for different times: 3 min (a), 5 min (b), 7 min (c), 8 min (d), 9 min (e) and 11 min (f).

Observing both Figure 19 and the plot of particle size and coverage factor of

Figure 20, one can note that the coverage factor increases with the growth time. However, for growth time below 8 minutes, this increase in the coverage factor does not go together with an increase in particle radius, indicating that, in this phase, some new particles are formed in addition to the growth of the originally deposited seeds. After 8 min, the particle radius, however, undergoes a strong increase.

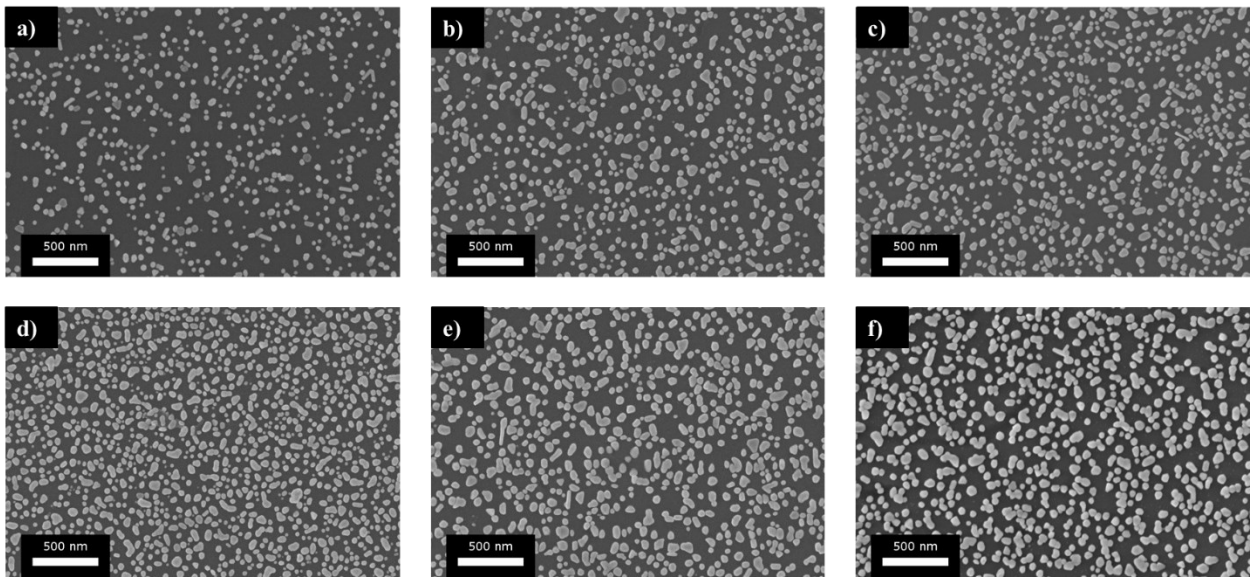

Figure 19: SEM images of the particles growth for different times: 3 min (a), 5 min (b), 7 min (c), 8 min (d), 9 min (e) and 11 min (f).

As a consequence of the particle growth, the substrate's optical response is also modified. In particular, as show in Figure 20 a), the absorbance is increased from around 0.05 at 3 minutes to

roughly 0.3 at 11 minutes. Moreover, the shape of absorbance spectra is changed: the plasmonic peak undergoes both a redshift of its maximum and broadening as the growth time increases.
This peak broadening, which is due to the formation of nanoparticles dimers that show optical response similar to the one of a nanorod, is, in particular, very beneficial for the preparation of a sensor able to work with an excitation wavelength located in the NIR (e.g. 785 nm).

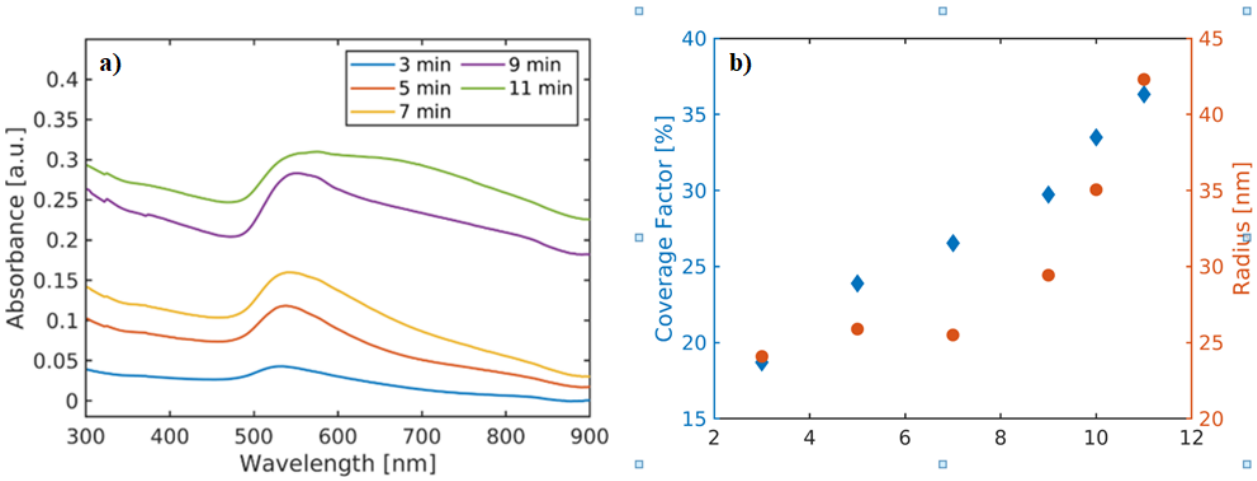

Figure 20: Evolution of the absorbance spectra (a) and of particle size (b) as a function of the growth time.

2.6 PARTICLE DEPOSITION AND CHARACTERIZATION

After particle growth, the substrates were imaged at both SEM and AFM to study their spatial distribution. Samples were mounted on SEM stubs using a conductive silver paste, coated with 3 nm of a Pt layer, and imaged in a Field Emission Scanning Electron Microscope (FESEM) FEI Inspect F at an acceleration voltage ranging from 5 kV to 20 kV.
The topological analysis of the substrates was realized by atomic force microscopy (AFM) with the Dimension D3100 AFM, performing a characterization in contact mode and obtaining both topography and lateral force signals.
A custom Python code was created to process the AFM images automatically. Images were preprocessed by background removal with a median filter, segmented determining the threshold value with the Li's method[54], [55]. The findCountours and getMoments functions provided by the Python-OpenCV library calculated the boundaries and centers of mass.
For each substrate the particle density φ was calculated as the number of adsorbed particles for unit area of substrate.

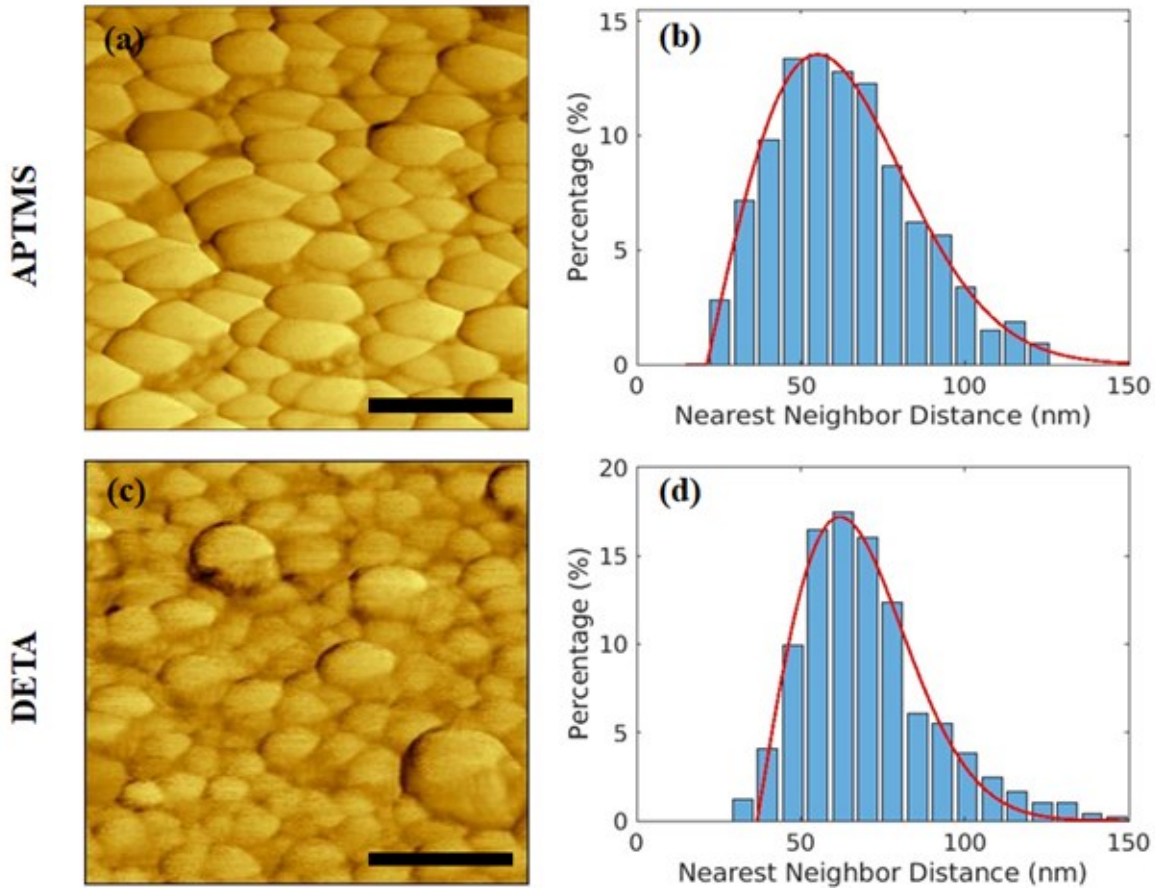

Figure 21: AFM imaged of gold nanoparticles after growh (a and c) and their respective nearest neighbor distribution (b and d). The red line represent the fitting of distribution.

2.7 SURFACE-ENHANCED RAMAN SPECTROSCOPY MEASUREMENTS

The analysis of the substrate homogeneity evaluated by coating the surface with a 4-mercaptobenzoic acid (MBA) self-assembled monolayer (SAM) is summarized in Figure 22 for both APTMS and DETA susbtrates. MBA was chosen as a model molecule in this case due to its high Raman cross-section and its capability of strongly bonding to gold nanoparticles. The Raman spectrum was recorded at different surface points, and a signal map was obtained at each point using the measurements made in a nine-point matrix. The MBA spectrum is characterized by two main peaks at 1076 cm^{-1} and 1588 $cm^{-1,}$ respectively. The first peak is associated with in-plane aromatic ring breathing and asymmetric stretching ν(C − S), whereas the second is due to the symmetric stretching ν(C −C).[56] A deviation in SERS signal expressed in percentage with respect to the average of the measured area can be defined as:

$$S_{dev}(x,y) = \left(\frac{S(x,y)}{\langle S(x,y)\rangle_{Area}} - 1\right) \times 100 \tag{2.81}$$

where $S(x,y)$ is the peak SERS signal at 1076 cm^{-1} at point (x,y), $\langle S(x,y)\rangle_{Area}$ is the average of the signal S over the entire area, and S_{dev} is the percentage deviation from that average value. Figure 4 shows the Raman map made over an area of 150x150 μm^2 and constructed using the signal of the MBA peak at 1076 cm^{-1} or 1588 cm^{-1}.

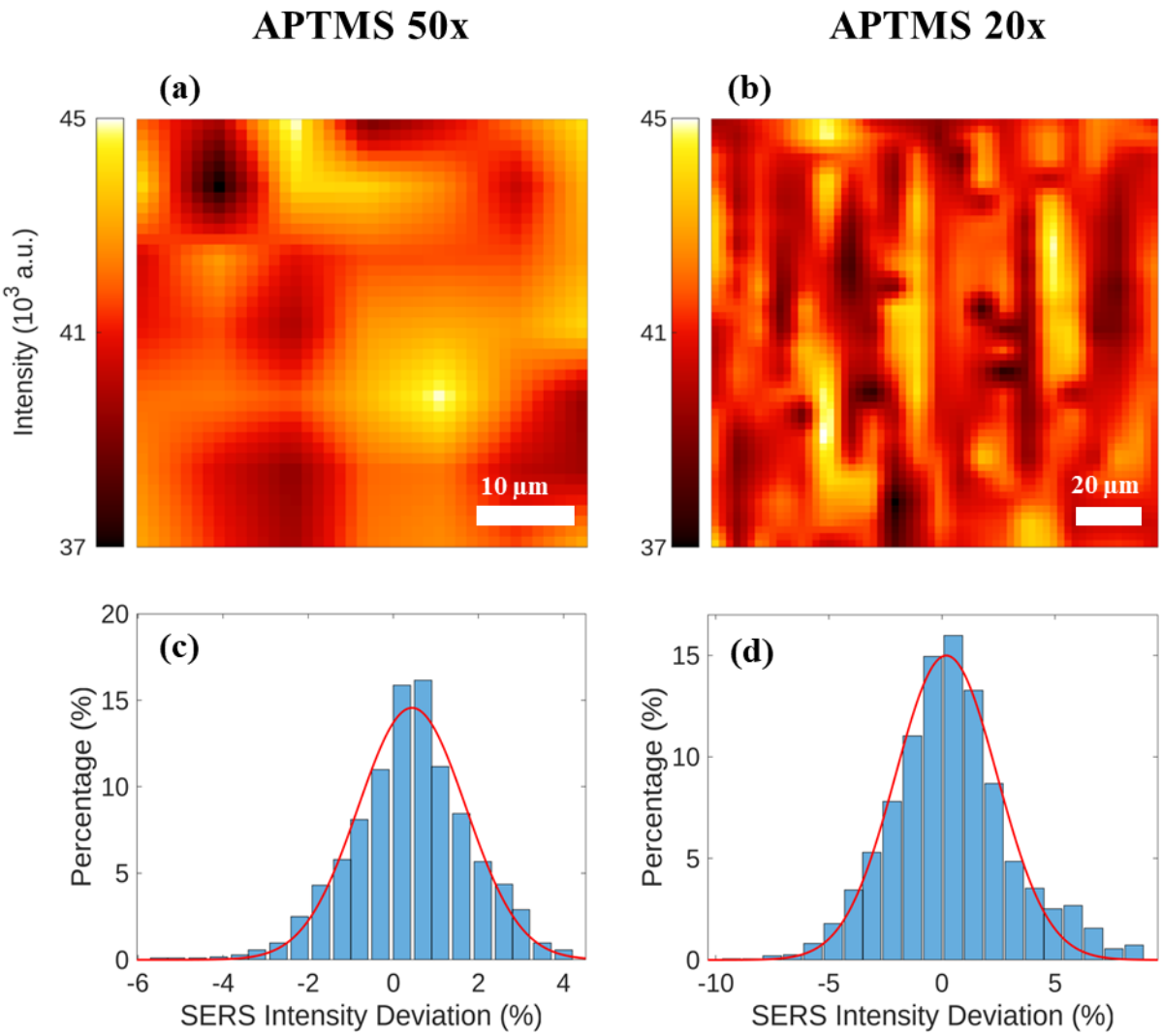

Figure 22: Maps and histograms of the SERS peak signal at 1076 cm^{-1} for samples functionalized with APTMS. We report measurements taken with 50x (a and c) and 20x (b and d) objectives. The distributions histograms (c) and (d) are fitted with Gaussians function (red-solid curves).

Moreover, we have compared the results with the Klarite [57] substrate from Renishaw (Table 2). Klarite is commercial a SERS substrates consisting of inversed piramyds, fabricated into a silicon substrate by means of chemical anistropic etching, coated with a gold thin film.
Klarite substrates were less uniform in terms of SERS Signal Intensity if compared to the substrates produced in the frame of this work. The different silanization also affected the substrate uniformity. When using a 20x objective, the APTMS substrate shows a lower standard deviation

on the SERS intensity, and we observe the opposite when using the 50X objective. The signal response has great homogeneity for both APTMS and DETA compared to Klarite and indirectly confirms the SERS hotspots' uniform distribution.

The same samples used for the homogeneity study have been cleaned by 30 min UV-O_3 treatment, and the SERS measurements, made afterward, demonstrate that the MBA has been completely removed. A new cycle of measures with MBA SAM has given the same results as before, demonstrating that the substrate is very stable and can be reused for more measurements by a simple cleaning procedure.

	Substrate	**σ (%)**	**3σ (%)**
20x	APTMS	1.3	3.9
	DETA	2.2	6.5
	Klarite	3.1	9.3
50x	APTMS	3.06	9.17
	DETA	1.95	5.85
	Klarite	ND	ND

Table 2: Comparison of relative deviation with respect to the average of the signal at 1077 cm^{-1} for the maps reported here and Klarite (ND: Not Detected).

After optimizing the growth time and deposition processes assessed as described above, SERS signals of 3-methylindole (skatole) solutions in the concentration range between (1 nM - 10 µM) were measured to evaluate the analytical performances. Previously cleaned by UV-O_3 treatment, substrates were immersed for one hour in solutions containing 3-methylindole at increasing concentrations. The Raman signal was measured from different points of the substrate at each concentration. Especially at the lowest concentrations, there are very few molecules of the analyte on the substrate. A significant number of measurements were needed to make a statistic and demonstrate the high sensitivity that the substrate allows.

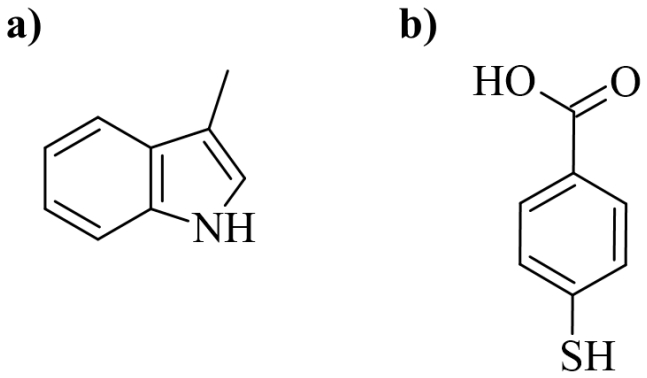

Figure 23: Chemical structures of the 3-methylindole (skatole) a) and of the 4-mercaptobenzoic acid b).

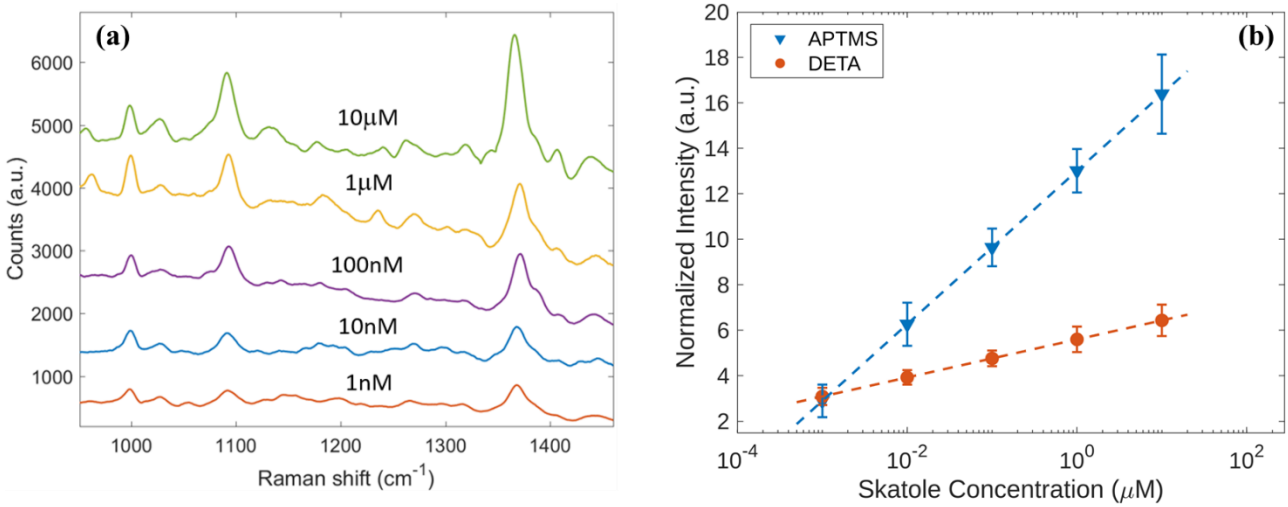

Figure 24: (a) Raman spectra for skatole at different concentrations obtained on the APTMS substrate. (b) Calibration lines for skatole detection on APTMS and DETA substrates.

Figure 24 resumes the analytical performances of the substrate. For both substrates (APTMS and DETA), the relation between skatole concentration and Raman signal is linear against a logarithmic axis for the concentration. The equation describing the substrate fabricated using APTMS is (y =0.136 x + 0.800), with R^2 = 0.989. Similarly, the linear fitting equation for the DETA based substrate is (y =0.033 x + 3.091), with R^2 = 0.969. The analyzed concentration range includes the accepted threshold levels for skatole, within the range of 0.5–1 µg/ml (1.8–3.6 µM), indicating that the proposed system can detect 3-methylindole at concentrations well below the ones at which the human being is sensitive. These results have been compared with skatole signal with Klarite, where at a skatole concentration of 100 µM the Raman signal is as low as 0.94

counts/(W s) for the most intense peak (Figure 22 a-b). The estimated limit of detection (LOD) and limit of quantification (LOQ) for the sensors prepared with the different silanes are reported in Table 3 and shows for both APTMS and DETA a LOD in the part-per-trilion range, achieving 42.2ppt for APTMS, orders of magnitude better than what is required by practical applications. In Figure 24 b), we compare SERS signals obtained for 10 µM skatole solution deposited on APTMS 2.5%, and DETA 4%.

Substrate	**LOD (nM)**	**LOD (ppt)**	**LOQ (nM)**	**LOQ (ppt)**
APTMS	0.32	42.2	0.98	129.1
DETA	2.22	292.4	6.67	878.7

Table 3: Detection limit and quantification for DETA and APTMS SERS substrates.

Chapter 3
SERS SUBSTRATE BY VAPOUR-PHASE CHEMICAL DEWETTING OF THIN FILM

The previous chapter focused on the wet-chemistry fabrication of gold nanoparticles, as they are chemically stable and UV-O_3 cleaning treatments are possible without affecting the SERS performances.
Cleaning treatments[58] are usually performed to remove the capping agents or other molecules adsorbed on the particle surface that may interfere with the SERS measurements
Unfortunately, this process its not possible when dealing with silver nanostructures that are known to be sensitive to oxidation and tarnishing phenomena[59]. Even though some combinated O_2-Ar plasma treatment for the cleaning of Ag-based SERS substrates have been developed[60], they have a significant impact on the particle optical response properties.
For this reason, this chapter describes a novel chemical method for the fabrication of Ag nanoparticle arrays via an innovative procedure, that does not require the use of cleaning treatments after the synthesis.
It is already well known that the dewetting of *thin films* (TFs) and *ultra-thin films* (UTFs) can prepare nanoparticle arrays[61], [62]. Currently, the most common methods to induce dewetting are based on rapid thermal treatments or laser processing, and for some polymers, the exposure to organic solvent vapor. This chapter aims to develop and discuss an alternative method for dewetting metal UTFs and TFs based on exposure to inorganic acid vapor. In particular, the research activity described in this chapter focuses on silver due to its limited reactivity with many acids, such as hydrochloric and nitric acids. Surprisingly, the exposure to hot water (70°C) vapor was also successfully tested for the preparation of silver nanoparticles by dewetting. At the end of the chapter, the non-reactive case of silver is compared with copper, which shows reactivity with the abovementioned chemicals, leading to particle formation with different morphologies.

3.1 DEWETTING OF METALS THIN FILM

Synthesis of metal nanoparticles is possible by different techniques, including chemical synthesis[63], laser ablation[64], and dewetting[65], [66] of thin or ultra-thin films. In particular, dewetting consists of the destabilization of the thin film, followed by its rupture to form nanoparticles or aggregated nanoislands[67].

Thin film dewetting can, in principle, occur following two different mechanisms[68], [69]: *spinodal decomposition* (SD) or *hole nucleation-growth* (HNG). Dewetting by SD mechanism was described for the first time in 1965 by Cahn[70] for systems characterized by a negative value of the second derivative of the Gibbs free energy, i.e., $\frac{\partial^2 G}{\partial h^2} < 0$. If we consider a thin film deposited onto a substrate, there will be, in general, a competition between the film-substrate adhesion forces and surface tension of the metallic layer. When some spontaneous fluctuations of the film thickness h are induced, they may grow exponentially with time. If the amplitude of such oscillations equals the initial thickness h_0, the film breaks up, losing its continuity.

On the other hand, dewetting by nucleation and growth of holes consists of an initial nucleation event that leads to the formation of a hole followed by a growth process comprised of transporting material away from the nucleation site to a retreating rim surrounding the hole.

As adjacent holes continue to grow, at a certain point, they merge and form ribbons of materials along their contact line.

Dewetting by HNG mechanisms for silver thin films was extensively described by Jacquet et al.[71], who proposed a new mechanism based on three steps (induction, hole propagation, and sintering) that are all governed by grain growth.

Dewetting is often a competition between spinodal decomposition and the hole nucleation-growth mechanisms[67]. The conditions $\frac{\partial^2 G}{\partial h^2} < 0$ is satisfied for thin film thickness above 5-6 nm, whereas for lower thickness the second derivative values rapidly increases, favoring the heterogenous nucleation and suppressing the spinodal decomposition[72]. The two mechanisms can be differentiated by looking at the influence of the film thickness on the dewetting pattern[68], [73]. In particular, according to the spinodal decomposition model, it is possible to define a characteristic length Λ, which shows a correlation the film thickness h_0.

$$\Lambda = \sqrt{\frac{16\pi^3\gamma}{A}} h^2 \propto h^2 \tag{3.82}$$

From the characteristic length, it is possible to calculate the interparticle distance L as:

$$L = a\Lambda = a\sqrt{\frac{16\pi^3\gamma}{A}} h^2 \propto h^2 \tag{3.83}$$

Moreover, also the particle diameter D and the particle density N have a dependence on h_0[73], namely:

$$D = \sqrt[3]{\frac{24\pi^3 a^2\gamma}{Af(\theta)}} h^{\frac{5}{3}} \propto h^{\frac{5}{3}} \tag{3.84}$$

$$N = \frac{A}{4\pi^4\gamma} h^{-4} \propto h^{-4} \tag{3.85}$$

Where A is the Hamaker's constant, γ is the surface tension, and $f(\theta)$ is a geometric factor related to the fraction of the NPs sphere above the substrate.

On the contrary, it was demonstrated by Jacobs et al.[74] that in dewetting by HNG, there is no spatial correlation with the film thickness, and particles are randomly distributed[75].
So far, rapid thermal annealing[76]–[78] or process with fast[79], [80] or ultra-fast laser[81] are the preferred way to perturbate the stability of the thin film and obtain its dewetting. Unfortunately, these processes require dedicated equipment, and for the use with non-noble metals, they usually require a protective atmosphere to prevent the oxidation of the nanoparticles. Also, these methods are unsuitable for dewetting particles on substrates that are heat-sensitive, e.g., polymeric substrates.
For example, Kumar et al.[82] described the effect of the process atmosphere in the thermal dewetting of a copper thin film, observing a lower dewetting rate in the air due to the competition between the film oxidation and decomposition. Moreover, using ovens and lasers implicates high energy costs and is likely to become relevant in industrial contexts, requiring specialized equipment. In addition, the dewetting processes based on laser processing and thermal treatment are unsuitable for polymeric substrates due to their low thermal stability.
Bhandaru et al.[83] developed a novel technique for dewetting polymer thin film, which they named solvent-vapor-assisted dewetting. This process involves exposing a thin polymeric film to a closed atmosphere saturated with a suitable solvent for the polymer. Also, the dewetting induced by poor solvent[84] or non-solvent (water vapor) [85] has been studied extensively.
The main difference between thermal and solvent dewetting is that the cause of instability is the long-range force of van der Waals interactions in the former. At the same time, it is the short-range force of polar interaction in the latter[86].
However, none of the previous works have considered using similar strategies for preparing metal NPs by dewetting thin films.

3.2 NANOPARTICLES SYNTHESIS

A silicon (100) p-doped wafer was cut into 10 by 10 mm substrates and subsequently sonicated in acetone, ethanol, and water for 1 minute. The substrates were cleaned in a basic piranha solution for 20 minutes, washed three times in ultrapure water, and dried under a chemical hood in a clean environment. Finally, silver thin films of different thicknesses, ranging from 4 nm to 14 nm, were deposited onto the silicon through a RF sputtering (Moorfield UK), keeping the pressure and the RF power fixed at 3 Pa and 75W, respectively, and changing only the deposition time.

The thin film, as deposited, was imaged with both SEM (Figure 25a) and AFM (Figure 25c), and despite containing holes and defects, it does not show any signal of spontaneous dewetting. This was also confirmed by imaging the sample after 24 hrs (Figure 25b) and observing no appreciable evolution of the film. Additionally, by means of UV-visible measurements, as reported in Figure 28, we can confirm that no spontaneous thin film dewetting occurs as the Ag TF's extinction spectra on silicon substrate do not show any LSPR peaks in the range from 250 to 800 nm.
On the contrary, after the chemical vapor dewetting of the film, a strong adsorption band due to LSPR is observed at around 374 nm, which matches with the result of the optical response for a silver nanoparticle of 80 nm diameter on a silicon substrate, obtained by BEM simulation and reported in Figure 26.
From the same simulations, it is evident that such a peak is absent for the case of AgCl nanoparticles. This can be considered as a first evidence of the the synthesis of silver nanoparticles.

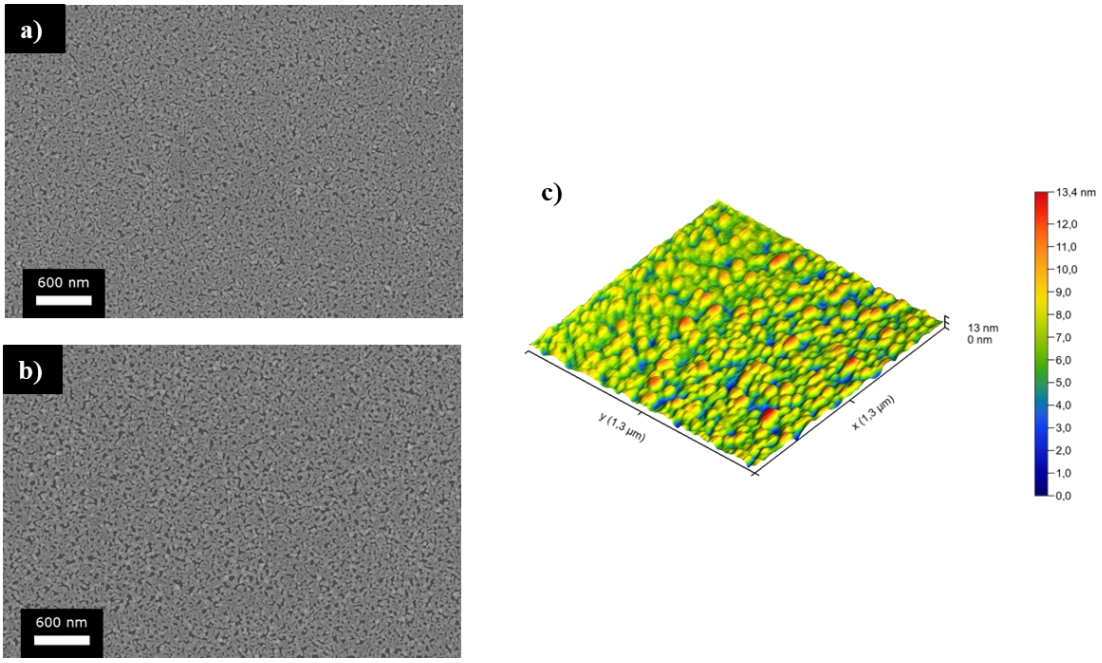

Figure 25: 6nm silver thin film as deposited on a Si wafer observed in the FESEM as deposited (a) and after 24 hours of exposure to air b). The film as deposited measured at the AFM c).

Subsequently, vapor-phase chemical dewetting was induced by exposing the substrates to nitric acid, hydrochloric acid vapors, or hot water vapors for a specific time, using the custom setup shown in Figure 27. After the exposure, the substrates were left drying under a chemical hood in a clean environment for 10 minutes and sealed in a vacuum bag to prevent silver oxidation or tarnishing.

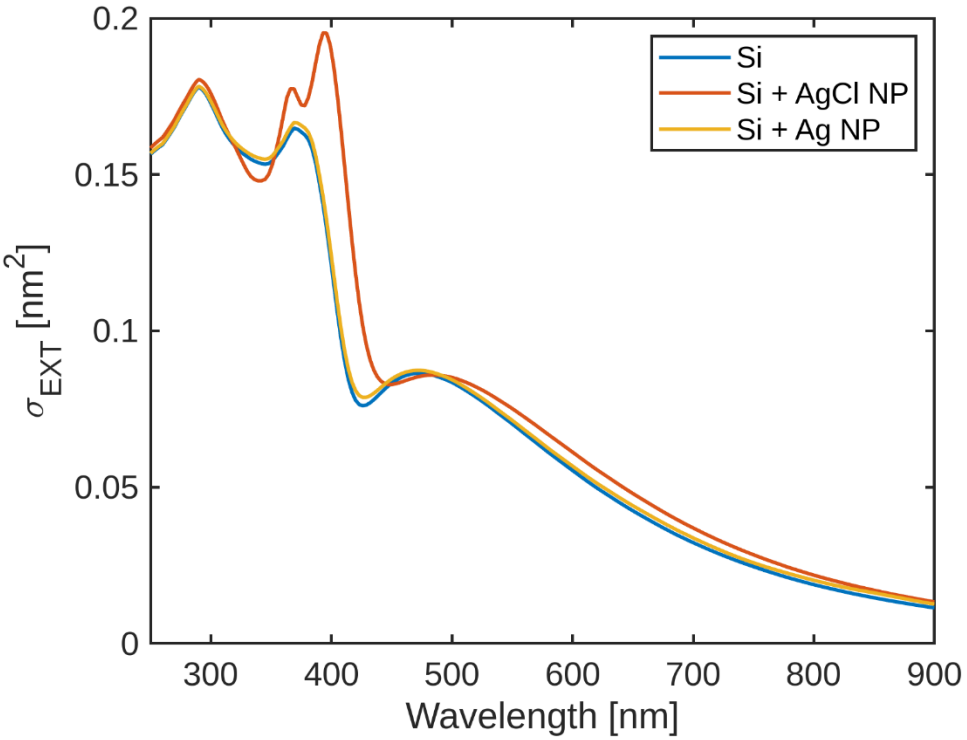

Figure 26: Simulated scattering cross-section of a silicon slab (Si), of a 80 nm AgCl nanoparticle on a silicon slab (Si+AgCl NP) and of a 80 nm Ag nanoparticle on a silicon slab (Si+Ag NP). Simulations were performed using the SCUFF-EM code[87].

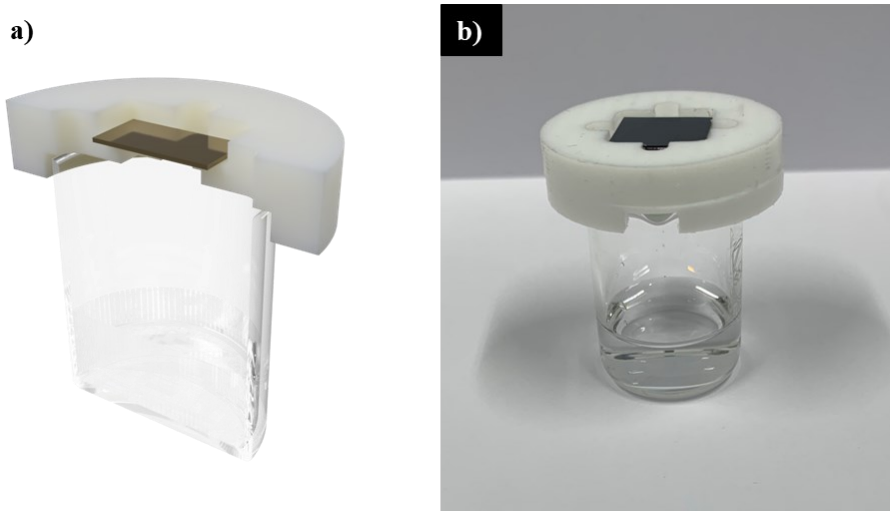

Figure 27: Tridimensional model (a) and photograph (b) of the setup adopted to expose the silicon-coated sample to the acid or hot water vapor.

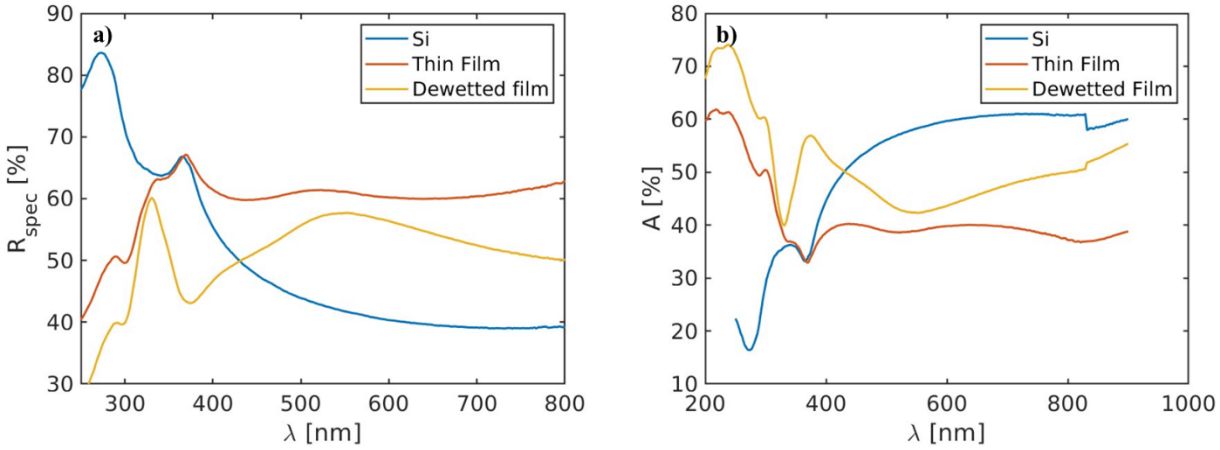

Figure 28: UV-visible spectra for a silicon substrate as provided (Si), coated with a 6 nm silver TF, and after the dewetting by exposure for 20 s to 6 M HCl vapor measured with an 8° incidence reflectance configuration (a). The same samples' absorption spectra are calculated from the reflectance spectra (b).

3.2.1 Effect of thin film thickness

The study of the effect of initial film thickness h_0 is of utmost importance to understand the dewetting mechanisms[68], [73], [88]. It has been widely observed that contrary to dewetting by hole nucleation and growth, spinodal decomposition exhibits spatial correlation with the film thickness[68]. TFs of different thicknesses in the range from 4 nm to 14 nm were exposed to 6 M HCl solution vapor for 20 seconds. The samples were named from A1 to A6 according to Table 1 and analyzed at FESEM; the obtained images are reported in Figure 29.

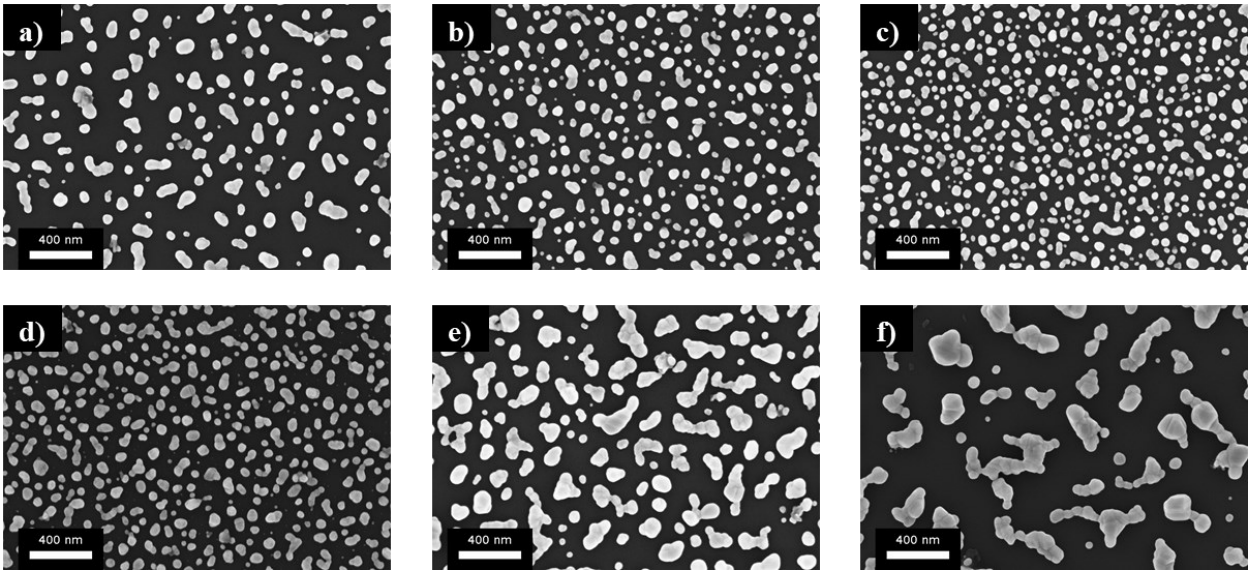

Figure 29: FESEM images showing the Ag NPs in samples from A1 to A6 (a-f).

For the electron microscopy analysis we used a Zeiss Supra 40 Field Emission Scanning Electron Microscope (FESEM) equipped with an Oxford EDS analyzer and a morphological and compositional characterization of the samples was carried out. Due to their excellent electrical conductivity, silicon samples were imaged without specific preparation.
To complete the morphology characterization of the NPs, Atomic Force Microscope (AFM) images were obtained with a Nanonics Multiview 2000 AFM, operated in phase feedback mode with a standard 20nm quartz tip. The scanning lateral resolution was set to 3.75nm, and the scanning step time to 22 ms. The average particle height was calculated by processing the AFM measurement as the average of the heights of each local maxima. AFM measurements for the different thicknesses are reported in Figure 30 and Table 1 summarizes the results of the particle morphology characterization.

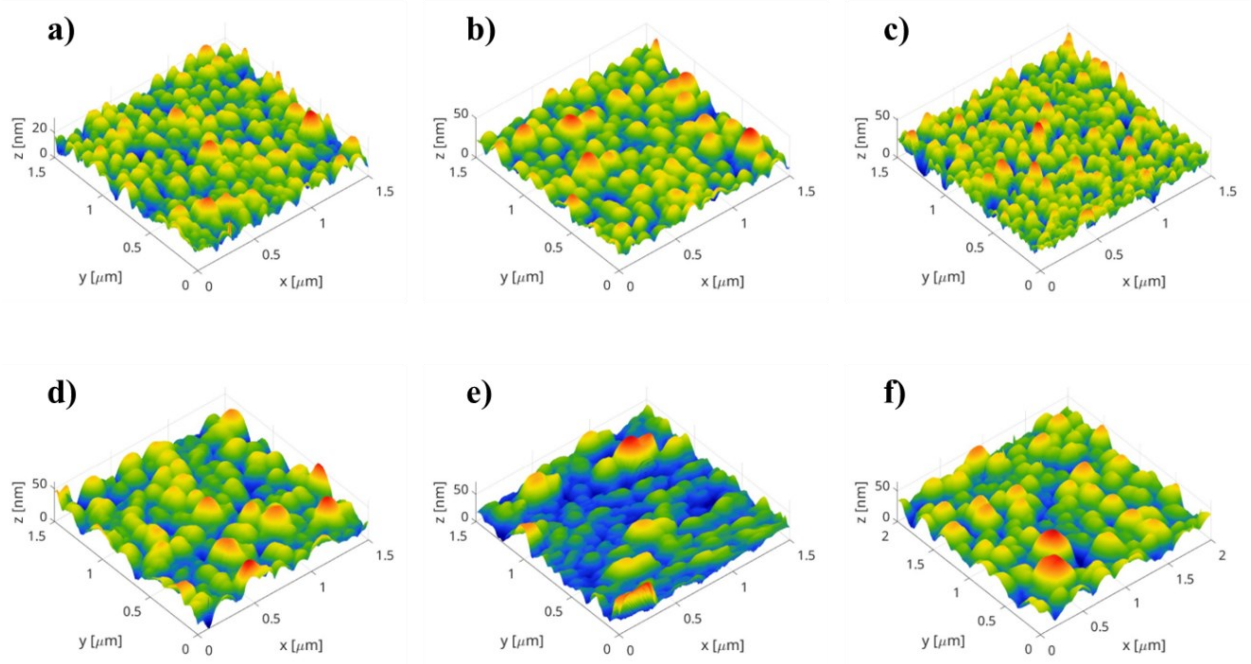

Figure 30: Dewetting samples from A1 to A6 observed at the Atomic Force Microscope (AFM).

The radial-integrated power spectrum density (RPSD) was computed from the FESEM images to study the morphology of the obtained particles, and the results are reported in Figure 31. The radial-integrated spectrum density is simply obtained by integrating the *power spectrum density* over the 2π angle.

$$RPSD(k) = \int_0^{2\pi} PSD(k\cos\phi\,, k\sin\phi)\; k\; d\phi \qquad (3.86)$$

Sample name	Film thickness [nm]	Density [NPs/um^2]	Mean Radius [nm]	Std Radius [nm]	Mean Elongation	Mean height [nm]
A1	4	37	38	16	1.33	20
A2	5	93	27	12	1.29	29
A3	6	131	25	10	1.43	36
A4	8	86	31	11	1.49	37
A5	10	30	52	26	1.54	35
A6	14	12	73	37	2.36	40

Table 1: Morphological characterization of the NPs obtained by dewetting Ag thin films of different thicknesses by exposure for 20 seconds to 6 M HCl vapor.

Where the PSD is the *power spectrum density* defined as:

$$PSD(\vec{k}) = \left| \int_0^\infty I(x,y) e^{i\vec{k}\cdot\vec{r}} dx\, dy \right|^2 \tag{3.87}$$

After fitting the RPSD with a gaussian function, the dewetting characteristic length Λ was finally determined as the :

$$\Lambda = \frac{2\pi}{k_{CENTER}} \tag{3.88}$$

Where k_{CENTER} is the frequency corresponding to the center of the fitting gaussian function.

Image segmentation and subsequent detection of each particle boundary using the *findCountours* function included in the Python OpenCV[89] library allowed the estimation of average diameter and particle density.

From Figure 32 (a) and (b), one can observe that, over the entire studied thickness range, i.e., 4 nm to 14 nm, no univocal correlation between the film initial thickness and particle diameter can be observed, and two regimes are distinguished. For thicknesses lower than 6 nm, the density of the particle increases with h_0 whereas the particle diameter *D* decreases. Above 6nm thickness, such trend is the reversed.

However, if the considered thickness range is narrowed down to 6 to 14 nm, a linear correlation of λ_{DEW} to h^2 ($R^2 = 0.97$), D to $h^{\frac{5}{3}}$ ($R^2 = 0.98$) and ρ to h^{-4} ($R^2 = 0.95$) is observed, as shown in Figure 33. This confirms that, for $h \geq 6$ nm the dewetting mainly occurs by a spinodal

decomposition mechanism. In general, it is known that the dewetting process sees a competition between the hole's nucleation and spinodal mechanisms. In our case, the hole nucleation and growth mechanism appear to be predominant for lower thickness, where the film defect density is higher[7], [29]. In contrast, for higher thickness, the spinodal decomposition prevails.

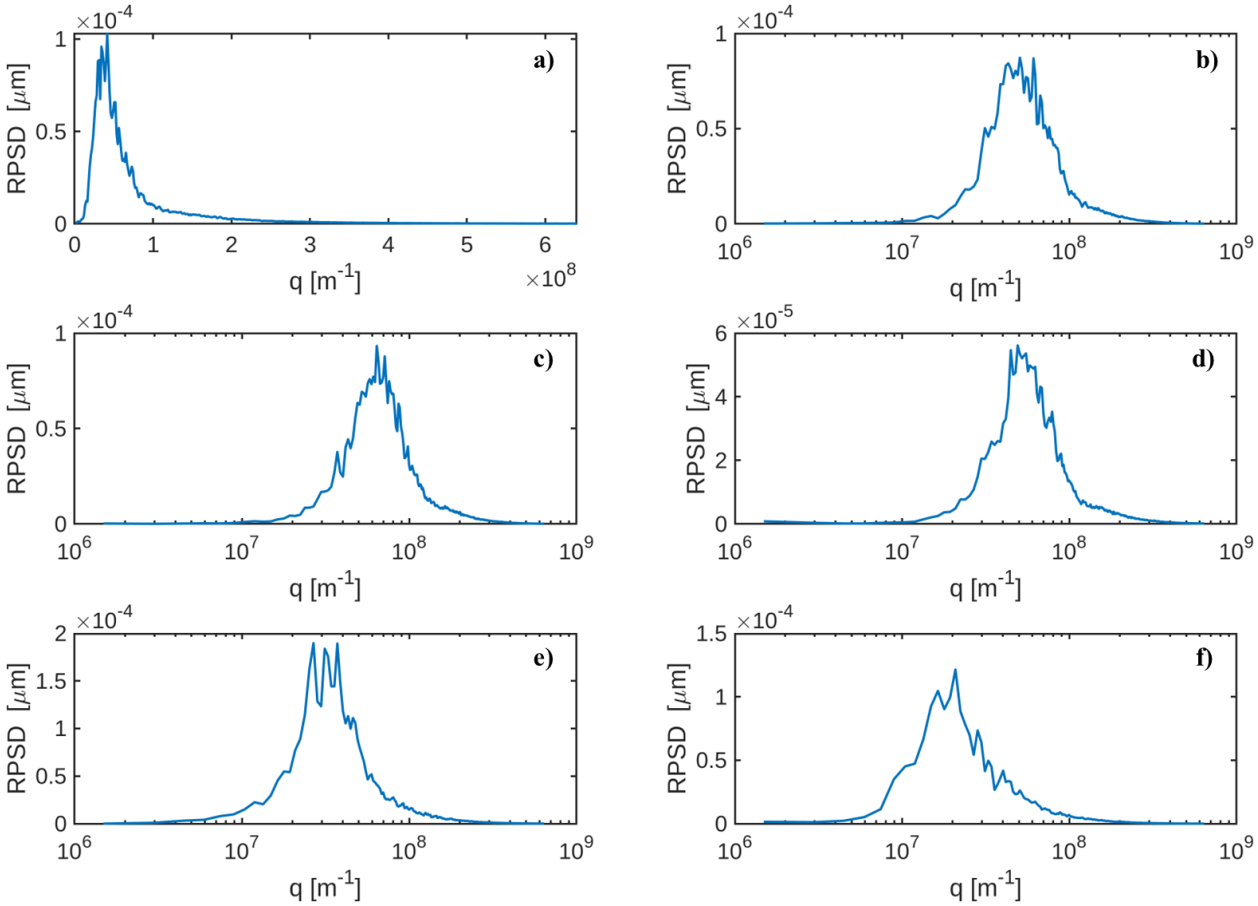

Figure 31: Radial integrated power spectral density (RPSD) for different Ag thin-film thickness: (a) 4 nm, (b) 5 nm, (c) 6 nm, (d) 8 nm, (e) 10 nm, and (f) 14 nm.

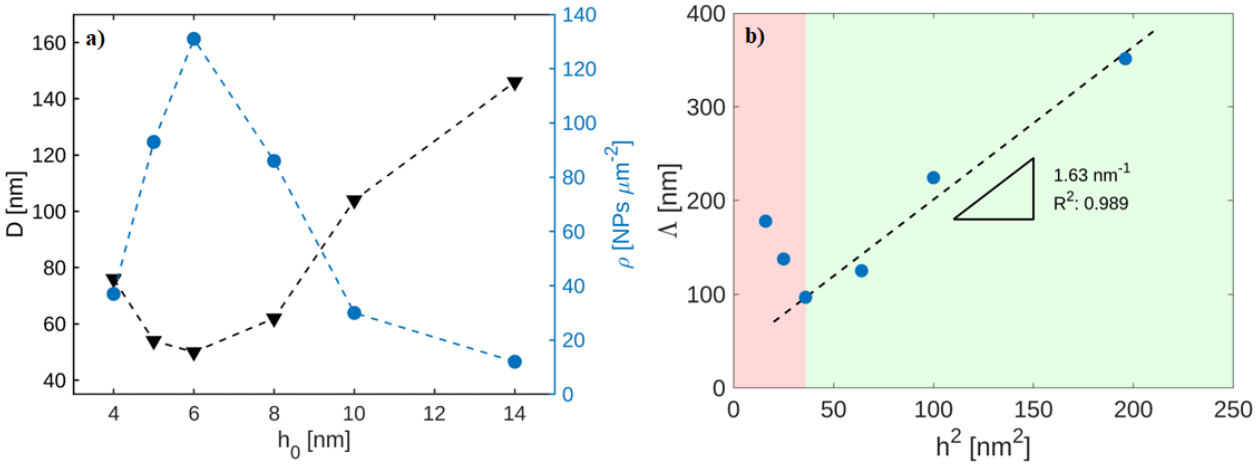

Figure 32: Average diameter and particle density as a function of the initial thickness h_0 (a) and correlation between the characteristic length Λ and h_0^2 (b). Dashed lines in (a) are drawn only as a guide for eyes.

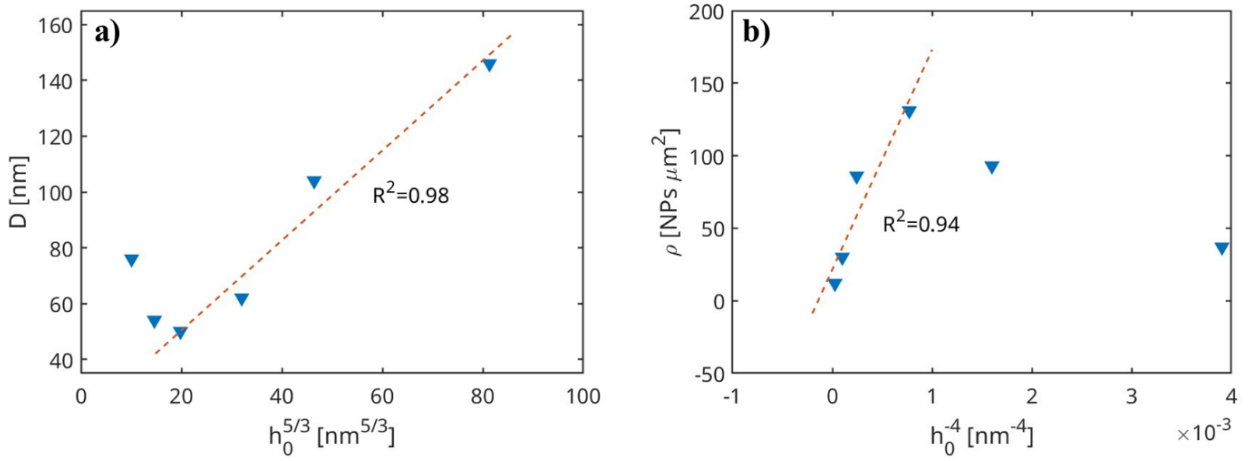

Figure 33: Correlation between the particle diameter D and $h^{\frac{5}{3}}$ (a) and between particle density ρ and h_0^{-4}(b).

3.2.2 Effect of dewetting agent

Another aspect of the chemical vapor dewetting studied in this work was the effect of the different dewetting agents on the morphology and chemical composition of the obtained nanoparticles. To this aim, we devised a set of experiments that used as the dewetting agent HCl at different concentrations, HNO_3 and H_2O as reported in Table 2. In particular, the exposure to the vapor of HCl at concentrations of 3 M, 6 M, and 12 M, HNO_3 (14 M), and water vapor was tested. The water was heated to 70°C and removed from the heating plate immediately before the substrate treatment to obtain significant amount of water vapor in the reaction chamber previously described.

All the test agents that induced the TF dewetting and the corresponding SEM images are reported in Figure 34 and Figure 35. As far as hot water vapor is concerned, the exposure time was reduced to 5 s, as the exposure for longer times leaded to the formation of particles with a diameter in the order of some µm, as shown in Figure 35.

The composition of the nanoparticles was studied employing *Energy Dispersion Spectroscopy* (EDS), *X-ray Photoelectron Spectroscopy* (XPS), and *X-ray Diffraction* (XRD). A first rough estimation of the particle composition was obtained by Energy Dispersion Spectroscopy (EDS) analysis, performed with a 60 µm aperture at an acceleration tension of 7 kV to limit the penetration depth of the electron beam as much as possible. In fact, Castaign's formula (3.89)[90], allows us to calculate an analytical volume of 151 nm for this working condition, which is comparable to the nanoparticle characteristic length.

$$z_m = 0.033(E_0^{1.7} - E_c^{1.7})\frac{A}{\rho Z} = 151\ nm \tag{3.89}$$

Where $E_0 = 7\ kV$ is the electron beam acceleration voltage, $E_c = 2.984\ kV$ is the lower characteristic X-ray emission energy, $A = 107.97\ u$ is the atomic mass of silver, $Z = 47$ is the atomic number of silver, and is $\rho_{Ag} = 10.49\ kg\ cm^{-3}$ the density of silver.

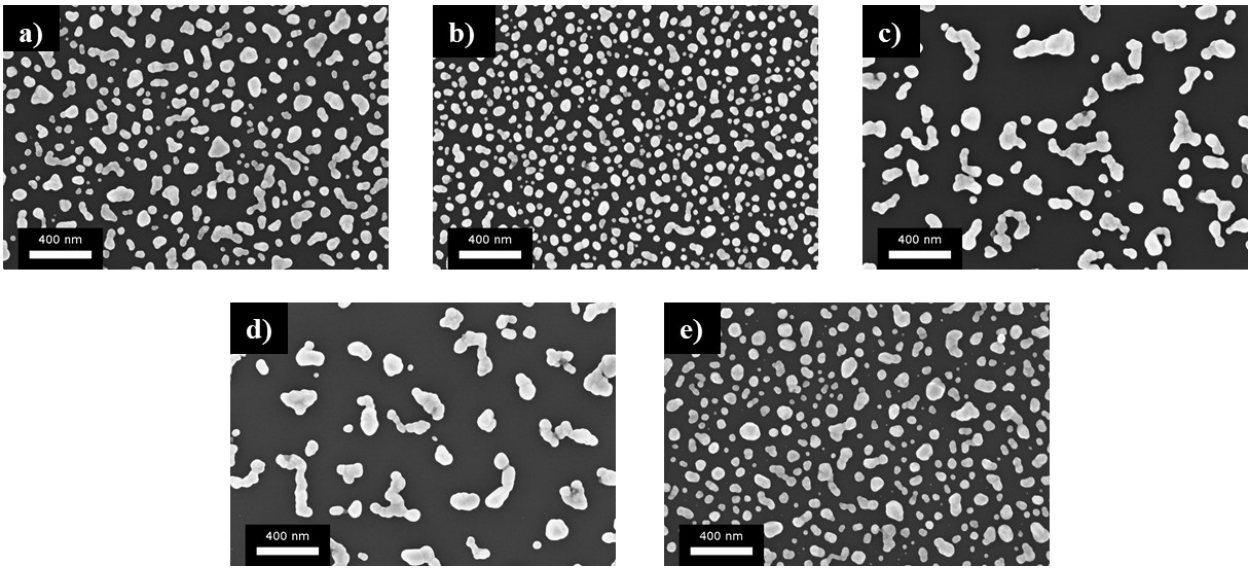

Figure 34: FESEM images showing the Ag NPs in samples B1(a), B2(b), B3(c), B4(d), and B5(e).

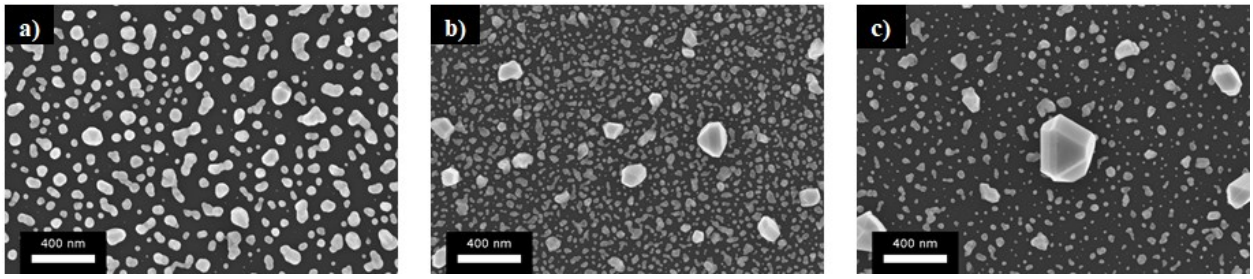

Figure 35: Dewetting of a 6 nm silver thin film obtained by exposure to 70°C water vapor for 5 s (a), 10 s (b), and 30 s (c).

Sample Name	Dewetting Agent	Exposure Time [s]	Density [NPs/um^2]	Mean R [nm]	Std R [nm]	Mean Elongation
B1	HCl 3 M	20	68	33	15	1.54
B2	HCl 6 M	20	131	25	10	1.43
B3	HCl 12 M	20	16	58	25	2.05
B4	HNO_3 65%	20	11	67	29	2.22
B5	H_2O 70°C	5	76	31	14	1.40

Table 2: Effect of the dewetting agent on particle density and morphological parameters of Ag NPs.

Grazing angle incidence X-ray diffraction measurements were performed in a Panalytical X'Pert Pro diffractometer with a Cu Kα source operated at 40 kV and 30 mA. The incidence angle was fixed to 1°, the scan step to 0.013°, and the scan speed to 600 s/°.
The X-ray diffraction pattern of both samples shows five diffraction peaks located at 38.1°, 44.2°, 64.4°, 77.4° and 81.7° which correspond, respectively, to the (111), (200), (220), (311) and (331) planes in silver. Although a diffraction peak at 55.8° is observed due to the presence of the silicon substrate, no peaks indicating the presence of AgCl, AgO, or $AgNO_3$ phases are visible.
XRD and EDS analyses are reported in Figure 34, from which we see that only the presence of Si and Ag was revealed from EDS spectra, excluding the formation of silver salt nanoparticles.

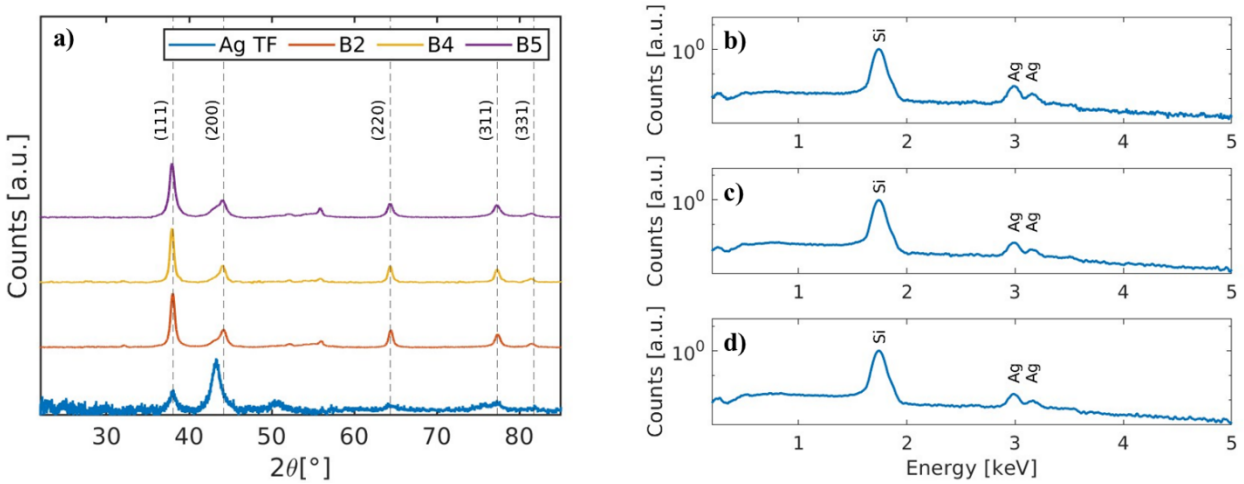

Figure 36: X-ray diffraction measurements on different samples a). Chemical composition of the nanoparticles studied through Energy Dispersion Spectroscopy on samples B2 b), B4 c) and B5 d).

Nonetheless, due to their low sensitivity and high analytical depth, both XRD and EDS analyses cannot completely exclude the presence of a reacted surface layer on the top of the NPs.

For this reason, XPS analysis, able to probe the outermost layer (< 10 nm) with a sensitivity as low as 0.01 % atoms, was employed, and the obtained spectra are reported in Figure 37 and Figure 38. Samples for XPS measurement were prepared and kept in a vacuum chamber at 10^{-5} mbar overnight and removed from the vacuum only some minutes before the analysis. X-ray photoelectron spectroscopy (XPS) was performed using a PHI Versaprobe 5000 instrument with a monochromated Al K-alpha source (1486.6 eV) and a double charge compensation source (Ar^+ and electron beams). The C1s peak (284.5 eV) has been set as a reference for charge compensation shift.

Whereas EDS did not reveal any element other than Si and Ag in any samples, XPS revealed the presence of a small concentration of reacted metal. In fact, for the HCl 6 M and HCl 12 M samples, there is a concentration of Cl of 2.6 %at. and 2.7 %at., respectively, and this can be interpreted as the presence of a very thin surface layer of AgCl on the nanoparticles. The samples treated with HNO_3 14 M did not show any traces of N or O, indicating the absence of a significative reacted layer.

For the sample in H_2O, however, results are inconclusive and do not allow any considerations on the outer reacted layer on the NPs. However, two broad bands located at 371.5 eV and 377.7 eV are visible in the analyzed samples, and plasmon loss bands are revealed in the high-resolution XPS spectra (see Figure 38). These bands, related to electron energy losses due to plasmonic modes in the metals, are only present in metallic silver and not in its salt.

	B2		B3		B4		B5	
	XPS [%at.]	*EDS* [%at.]	*XPS* [%at.]	*EDS* [%at.]	*XPS* [%at.]	*EDS* [%at.]	*XPS* [%at.]	*EDS* [%at.]
Ag	23.6	3.2	21.8	2.9	25.1	2.8	25.9	2.6
C	15.3	3.2	22.5	6.7	16.2	3.6	23.3	4.1
Cl	2.6	-	2.7	-	0.3	-	0.2	-
O	24.6	0.2	23.1	0.8	27.7	0.4	20.8	0.6
S	5.1	-	4.4	-	4.4	-	3.7	-
Si	28.8	93.4	25.6	89.6	26.4	93.2	26.1	92.7

Table 3: Compositional analysis through Energy Dispersion Spectrscopy (EDS) and X-Ray Photoelectron spectroscopy (XPS) of the samples B2-B5.

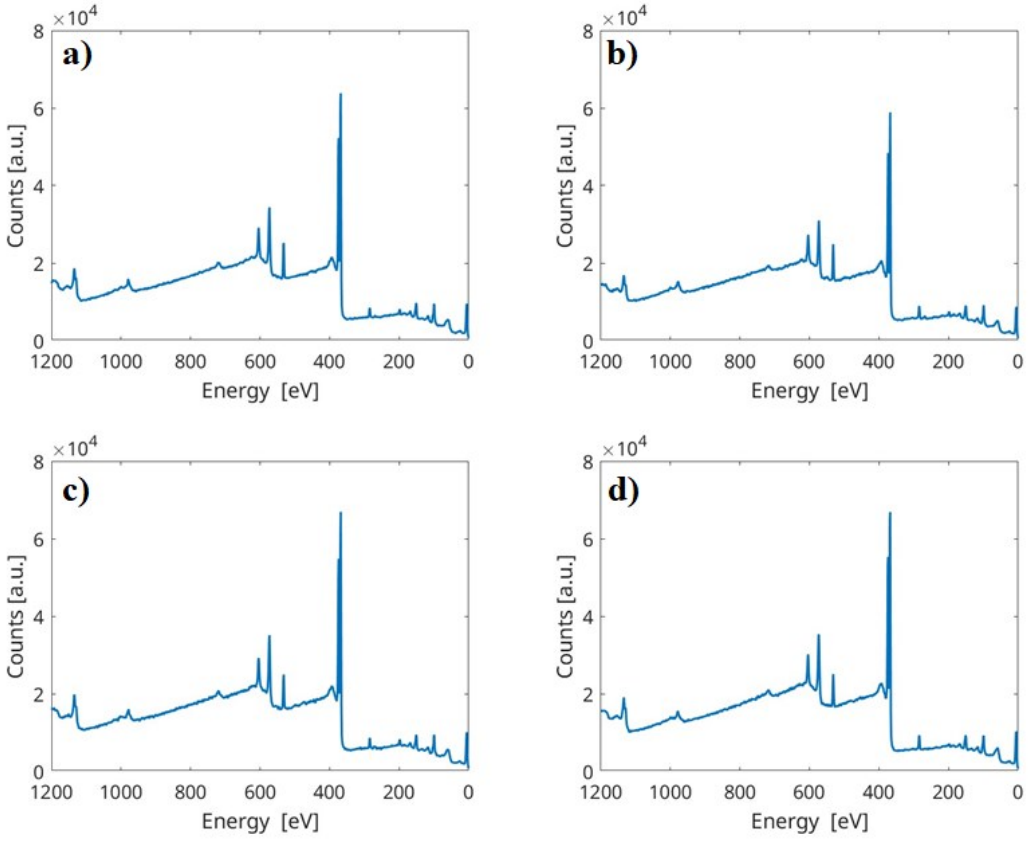

Figure 37: X-Ray photoelectron spectroscopy (XPS) survey in the bonding energy range from 0 to 1200 eV performed on Sample B2 (a), B3(b) , B4 (c) and B5(d).

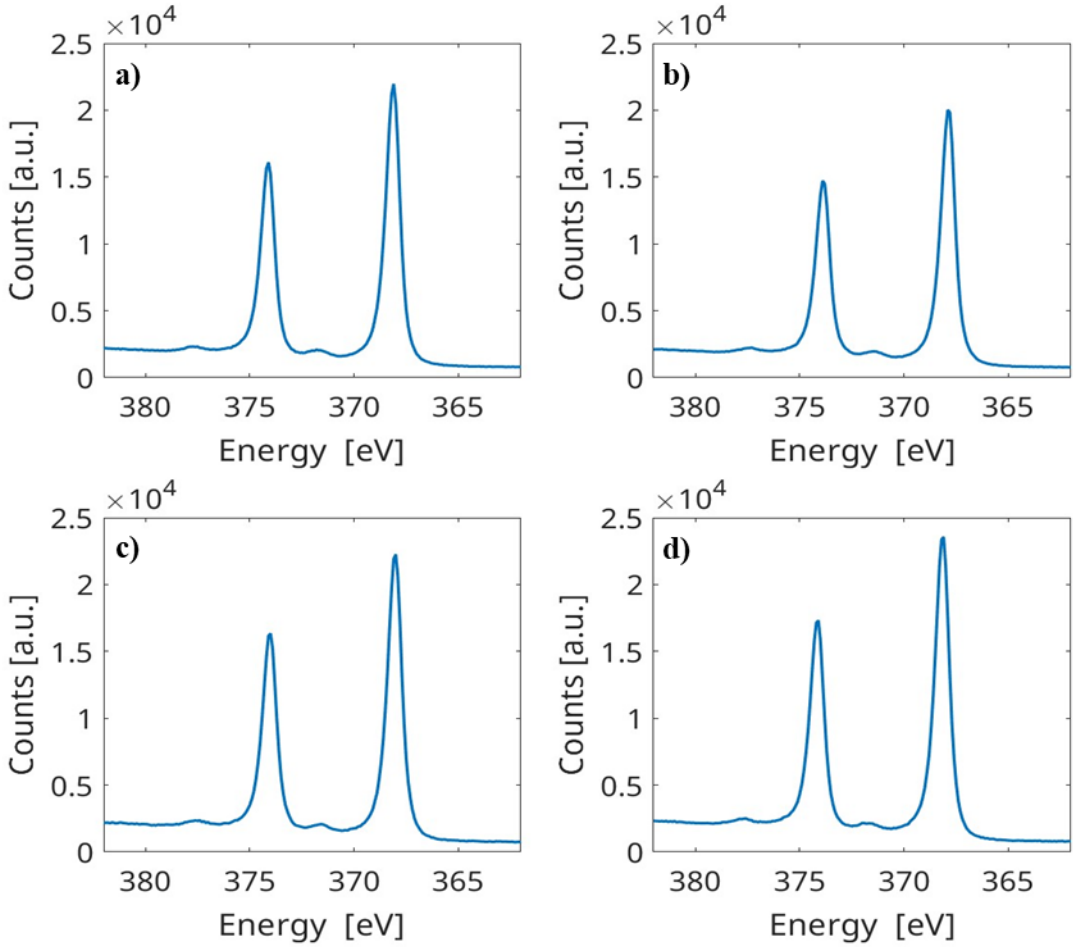

Figure 38: High-resolution XPS analysis focused on silver $Ag3d_{3/2}$ and $Ag3d_{5/2}$ peaks performed on Sample C2 (a), C3(b) , C4 (c) and C5(d).

3.2.3 Reactive dewetting on Copper

A 6 nm thin film of copper was deposited on the silicon wafer and exposed for 20 seconds to dewetting agent. In Figure 39, we report the dewetting structures obtained by exposing the copper film to HCl 6 M (a), HCl 12 M (b), and HNO_3 14 M (c). Samples were named C1, C2, and C3, respectively.

Contrary to what we obtained for the silver film, copper forms nanostructures with different morphology for each tested dewetting agent. This phenomenon indicates a chemical reaction that drives the formation of copper salts that crystallize along a preferential direction.

The composition of these nanostructures was studied utilizing EDX analysis, which indicated that a chemical reaction occurred in all three cases.

This phenomenon, we named *vapor phase reactive chemical dewetting*, is a process that consists of both film dewetting and chemical reactions. In sight of the limited state of the art and due to the

complexity of the involved mechanisms, further considerations are not included in the present thesis. A confirmation of the presence of products of reaction is given by the EDS analysis reported in Figure 40.

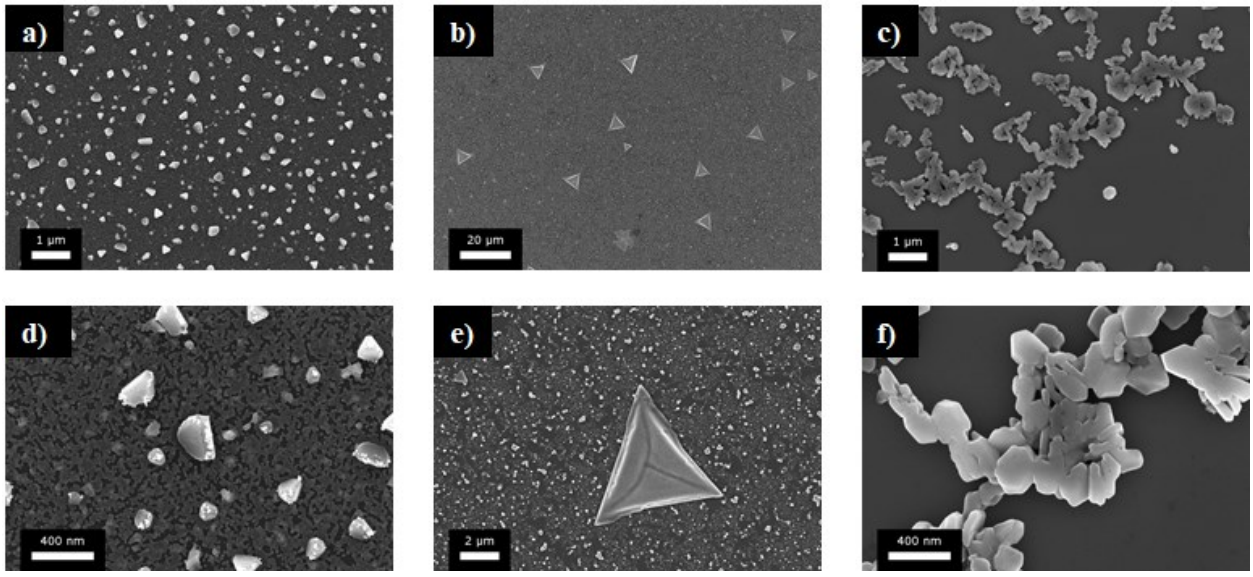

Figure 39: FESEM images showing the Cu NPs obtained by exposing a 6nm TF to different dewetting agents: C1 (a), C2 (b) and C3 (c). The same samples were observed at FESEM at higher magnification (d-f).

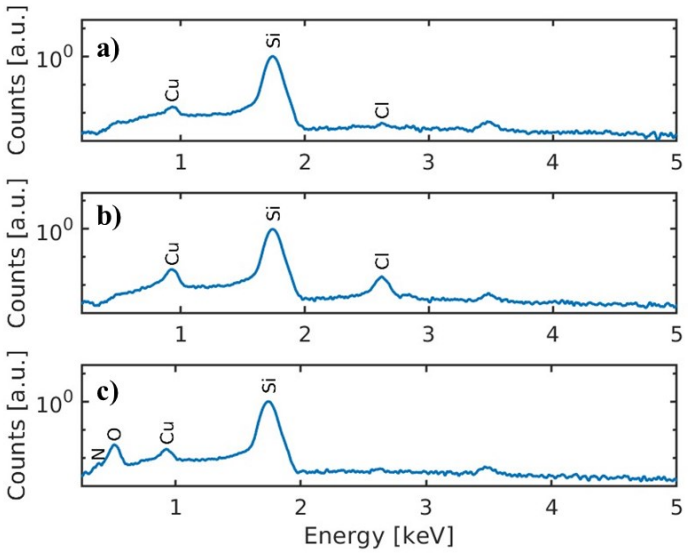

Figure 40: EDS analysis of the samples C1 (a), C2 (b) and C3 (c).

3.3 SERS MEASUREMENT

After fabricating the Silver nanoparticles by chemical vapor dewetting, we tested their performance as SERS substrates. To obtain the substrates meant for SERS, silver thin films of 6, 10, and 14 nm thickness were deposited onto quartz substrates and exposed for 20 s to the vapor of an HCl 6 M solution. The axial transmission spectra of the samples in the wavelength range from 300 nm to 900 nm were measured with a Shimadzu UV-2600i UV-visible spectrophotometer. Assuming the reflection to be negligible if compared to adsorption, the Absorbance was calculated as follows:

$$Abs = 2 - \log_{10}(\%T) \tag{4.90}$$

The 6 nm sample presents the typical extinction spectra of silver spherical nanoparticles, with a LSPR peak located at 420 nm[91]. As the initial thin-film thickness increases, agglomerates of nanoparticles are produced, and a redshift and broadening of the LSPR are observed. Moreover, the maximum extinction undergoes a slight decrease as a result of the lower particle density[91], [92]. This broadening[93] of the LSPR is of utmost importance as the substrate exhibits electrical field enhancement over a larger range of the visible region. Therefore, they are suitable for SERS measurements under different laser excitation wavelengths.

We employed a Renishaw InVia Raman microscope with a laser excitation wavelength of 532nm for the SERS measurement. Power and exposure time were tuned from 30 μW to 300 μW and 3s to 30 s, respectively, to obtain an appropriate signal-to-noise ratio for all the studied analyte concentrations and avoid the detector saturation for the most concentrated samples. The number of accumulations was kept fixed at 5 for all the measurements. All the spectra we converted into a normalized intensity I_{norm} spectra according to Figure 41(b). Where P is the laser excitation power, NA is the numerical aperture of the use objective, t_{exp} is the exposure time and n_{acc} is the total number of accumulations for each spectrum.

Therefore, considering that the Raman excitation wavelength is 532 nm, the 14nm film was chosen to prepare the SERS substrate as it shows the highest extinction cross section at this wavelength. For the SERS measurement, we tested different concentrations Rhodamine 6G in the range from 10^{-6} to 10^{-10} M, and 30 uL drop of water solutions was deposited onto different sensors, which were dried under an Argon flow to prevent the oxidation and contamination of the NPs.

The Raman band located at a Raman shift of 611 cm^{-1} (C-C-C in-plane bending) was selected for the quantification of the analyte. A calibration curve, reported in Figure 41(b), was obtained plotting the normalized intensity I_{norm} as a function of the sample concentration. The Limit of quantification (LOQ) and the Limit of detection (LOD) were calculated, according to the *International Conference on Harmonization of technical requirements for registration of Pharmaceuticals for Human (ICH)* method[94] as illustrated in Chapter 2. We obtained LOD and LOQ equal to $1.9 \cdot 10^{-11}$ M (9.1 ppt) and $3.5 \cdot 10^{-11}$ M (18 ppt), respectively.

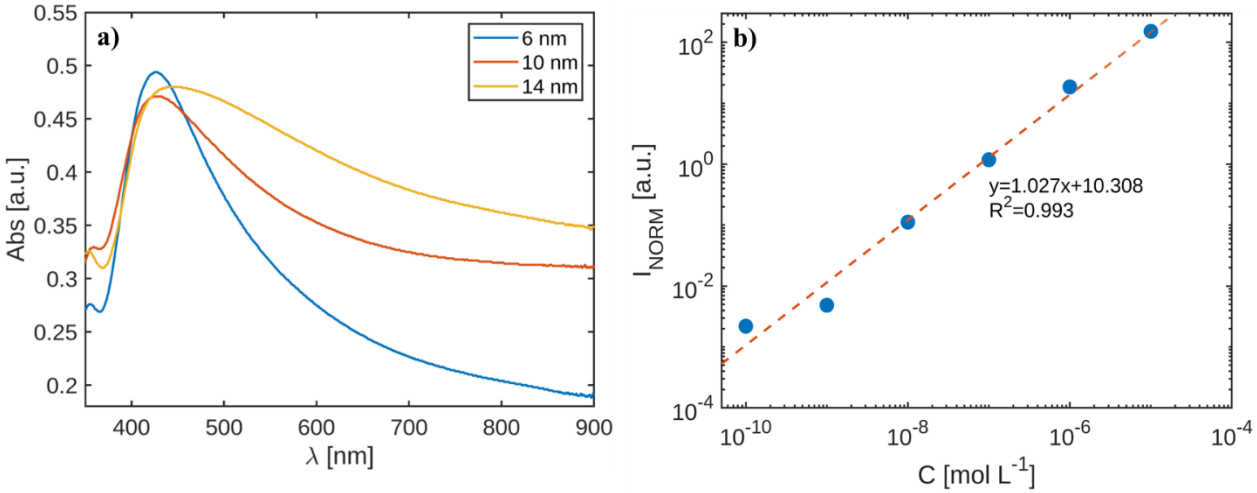

Figure 41: Extintion spectra for SERS substrate obtained by dewetting of different thickness Ag TF (a) and calibration curve for SERS measurement on Rhodamine 6G (b).

3.4 NANOSTRUCTURED COLORING

The use of CF_4 for silicon dry etching in a Reactive Ion Etching (RIE) system is nowadays widespread, and its fundamental mechanism has been widely discussed [95], [96]. For this reason, after the formation of NPs, the substrates were etched in a CF_4 atmosphere using a SAMCO RIE-10NR for 2, 4, and 8 minutes. The etching pressure was fixed at 11 Pa, the gas flow to 30 sccm, and the generator power to 200W. Before processing the samples, the chamber was conditioned with a 5-minute treatment in O_2 plasma at 100W and 50 Pa to remove any carbon contaminants that may interfere with the chemistry of the CF_4 plasma.

After the RIE process, samples were cleaned for 12 minutes in 12 mL of acid piranha solution to remove the silver nanoparticles and any residue deriving from the CF_4 polymerization. Substrates were washed twice in ultrapure water and ethanol and dried under a chemical hood in a clean environment. Such a volume of acid piranha solution was prepared by slowly adding 3 mL of H_2O_2 33% wt. to 9 mL of H_2SO_4 98% wt.

The pillar height obtained for the three values of etching times is 110 nm, 221 nm, and 316 nm, respectively, as shown in Figure 42, resulting in an average etching rate of 27.2 nm min^{-1}. The etched substrates were coated with a 35 nm layer of silver utilizing a Moorfield RF Sputtering at a pressure of 5 Pa and power of 75W. The pillar structure was therefore coated by the deposition of a 40 nm layer of silver through RF sputtering at a pressure of 5 Pa to ensure good conformity of the deposited layer.

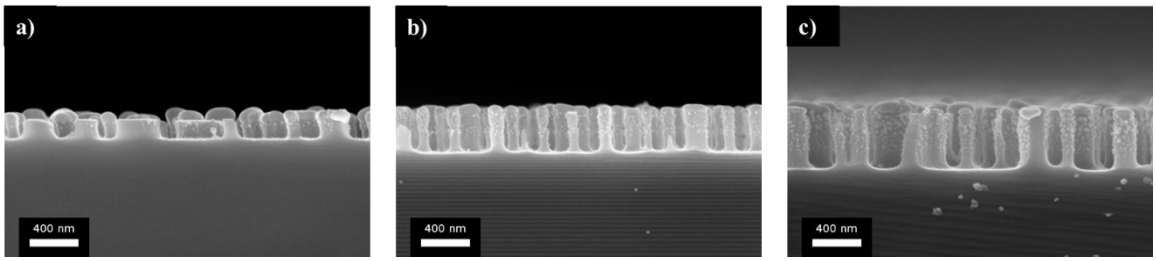

Figure 42: Cross section of the silicon pillar observed at the FESEM for different etching times: 4 min (a), 8 min (b) and 12 min (c).

The obtained structures show an intense coloring as illustrated in
Figure 43. From Figure 44, it can be observed that the position of the maximum reflectance undergoes a redshift as the pillar length is increased; moreover, a broadening of the peaks also occurrs. We can thefore conclude that the position of the reflectance peak is a function of the pillar height and is tunable to obtain the desired color.

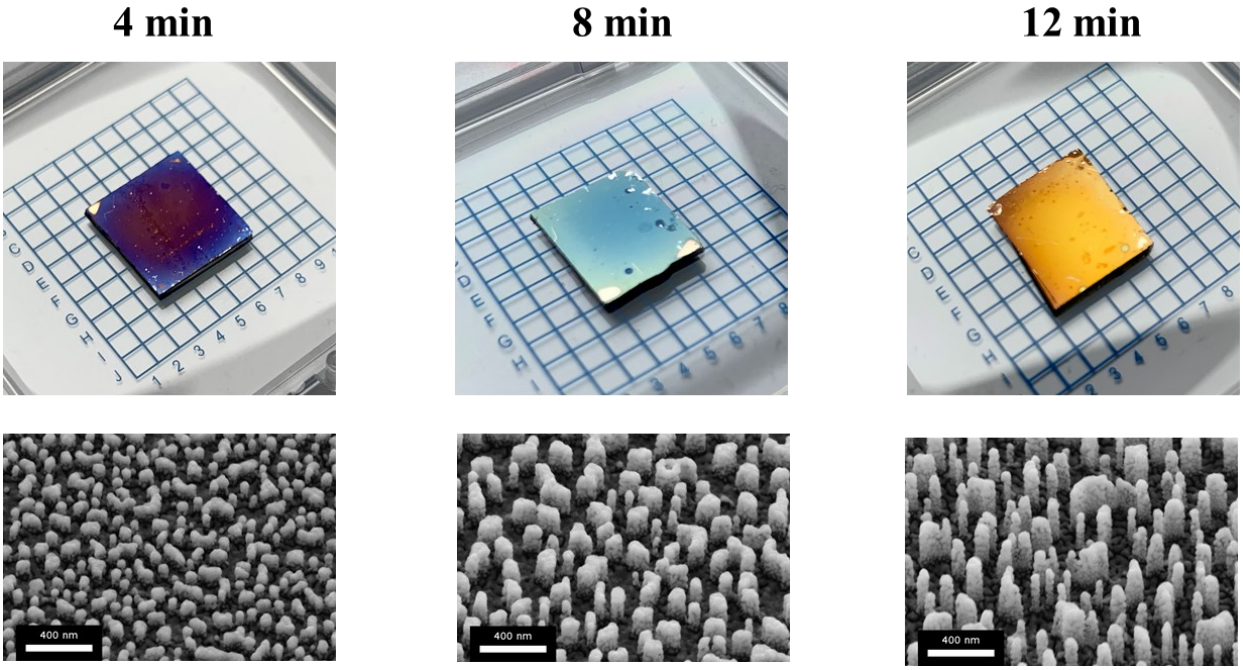

Figure 43: Nanostructured coloring obtained by coating with 40 nm layer of silver the pillar obtained by etching the silicon with particle mask for different etching times.

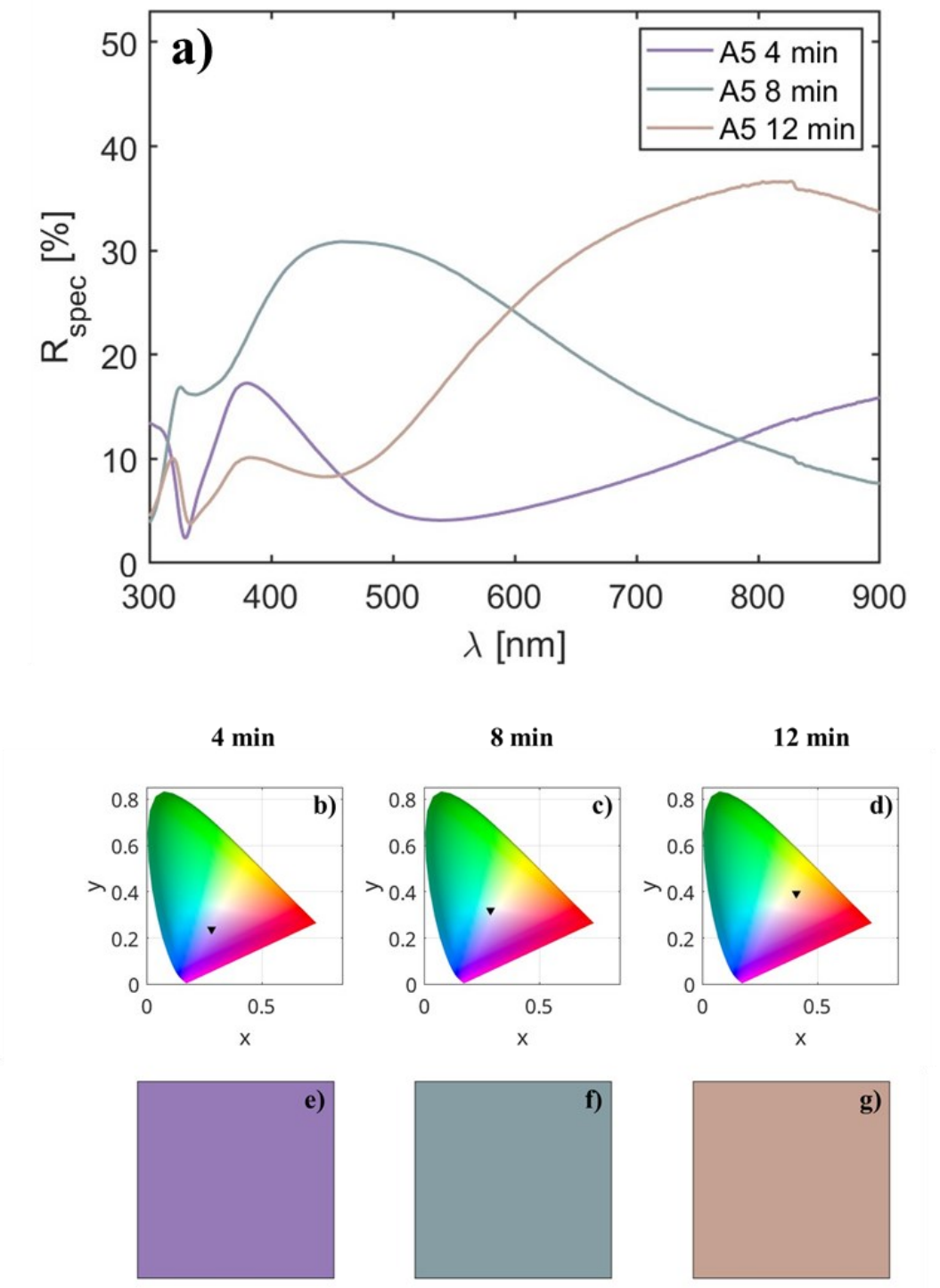

Figure 44: Reflectance measured as a specular reflection at 8° of the nanostructured color samples (a). Color representation in CIE color space(b-d) and RGB reconstruction obtained from reflection spectra (e-g) using the spectrum2XYZ [97] Matlab library.

Chapter 4
SERS SENSORS BY THIN-FILM DEPOSITION ON NANOSTRUCTURED SUBSTRATES

While the previous chapter describes an innovative method for dewetting thin film by exposure to chemical vapor, this chapter introduces another approach based on the thin-film dewetting of a copper ultra-thin film (UTF). In this case, the dewetting is achieved by treatment with a pulsed laser in the nanosecond regime. The process was realized in the absence of a protective atmosphere; thus, the particles undergo oxidation and do not have LSPR response, but they were used as a low-cost etching shadow mask to create nanopillar-based functional surfaces on soda-lime glass for different applications, e.g., superhydrophobic surface and SERS nanostructured substrate.
A particular emphasis is given to SERS measurement for the detection of nanoplastics, where the obtained limit of detection is roughly three orders of magnitude higher than the record value reported in the literature, paving the way for more widespread use and a better characterization of this kind of contaminant.

4.1 LASER-INDUCED DEWETTING

Laser induced dewetting (LID) of metal-thin and ultra-thin film has already been used to prepare isolated nanoparticles or arrays of them. When a metal thin film is quickly heated to its melting point within the duration of a laser pulse, it breaks and can self-assemble to form nanostructures.
Indeed, recently, thin and ultra-thin film dewetting has been obtained through processing with fast[98] or ultra-fast laser[99]. The main advantage of using a laser to induce a thin film dewetting is the possibility of finely tuning the particle size by changing the beam fluence and selectively processing the substrates easily defining patterns and areas where the nanoparticles are generated.
Horwood et al.[100] studied the dewetting of a 4 nm Au thin-film on tantalum pentoxide substrate with a nanosecond-pulsed laser operated at a wavelength of 500 nm and a pulse width of 9 ns. Using different fluences, they observed that the minimum fluence required to obtain the thin film dewetting was 250 mJ cm^{-2} at a 5 s irradiation time, suggesting the existence of a threshold required to destabilize the thin film. In fact, for lower fluence, they reported no dewetting or only partial dewetting, even for much longer irradiation time.
Experimental evidence confirms that laser-induced dewetting is mainly based on spinodal decomposition. In fact, it was demonstrated by Owusu et al. [101], for dewetting of an Au thin film on a Ta substrate, that characteristic length *L* has quadratic dependence on thin film thickness

h ($L = 5.13h^{2.04}$), whereas the particle density N depends on the fourth power of h^{-1} ($N = 2.93 \cdot 10^{12}h^{-4.03}$). All these experimental results are in total agreement with the spinodal decomposition theory formulated by Cahn.

Also, the morphology of the substrate has an evident influence on the dewetting dynamics of the thin film. It was observed by Torrisi et al.[102] that a critical initial thickness exists below which the surface roughness does not affect the average size and distance between particles. Above this value, they observed that increasing the roughness leads to a bimodal size distribution of the obtained particles. In this work, authors irradiated Pt and Au thin films of different thicknesses deposited on an fluorine-doped tin oxide (FTO) glass substrate with a 532 nm Nd:YAG (neodymium-doped yttrium aluminum garnet) nanosecond laser. They studied the effect of surface roughness on the nanoparticle size distribution. The critical thickness value d_c was estimated to be $3\ nm < d_c < 7.5\ nm$ for Pt and $7.5\ nm < d_c < 12.2\ nm$ for Au.

4.2 NANOPARTICLES SYNTHESIS BY LASER-INDUCED DEWETTING

In our experiment, a soda-lime glass microscope slide with a roughness of R_a~1nm was cut into 20 mm by 20 mm substrates and sonicated in acetone, ethanol, and water for 5 minutes at each step. Next, the substrates were cleaned in a basic piranha solution for 20 minutes at 70°C, washed three times in ultrapure water, and dried under a stream of N_2. Finally, copper ultra-thin films of different thicknesses, ranging from 4 nm to 7 nm, were deposited onto the substrate by PVD (Moorfield RF Sputtering) at a pressure of 3 Pa and power of 75 W.

Laser processing of the samples was performed in air employing an industrial-grade infrared fiber nanosecond laser (DATALOGIC AREX 20MW, Bologna, Italy). The output laser beam was scanned at a speed of 3 mm s^{-1} across the substrate in predefined patterns, with a galvanometric scan system coupled to an F-Theta lens, providing a beam spot size of ~60 μm. To perform the dewetting, the laser parameters were set at a pulse repetition rate of 20 kHz at an average power of 2.6 W, resulting in a peak fluence of 4.6 J cm^{-2} at 400 pulses per spot. The distance between the laser scan lines was set at 20 μm to obtain uniform coverage of the patterned surface and the desired dewetting results.

The topographic and morphological analyses of the processed samples were carried out using a Zeiss Supra 40 Field Emission Scanning Electron Microscope (FESEM) and Nanonics Multiview 2000 Atomic Force Microscope (AFM). SEM and AFM images of the 4 nm sample treated with different laser powers and used to identify the optimal power are shown in Figure 45.

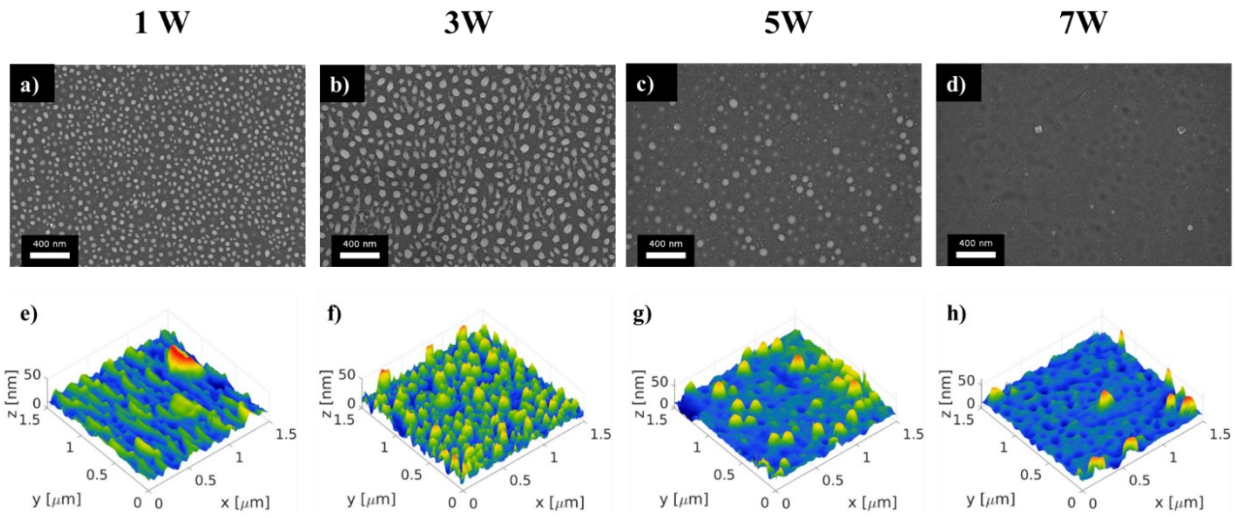

Figure 45: Effect of laser power on the dewetting behavior of 4 nm Cu TF.

As visible in the figure, low power (1 W) did not induce a complete thin film dewetting, leaving a significant number of elongated nanoparticles. In contrast, the treatment at 7 W obtained the almost complete removal of the metal film from the substrate. After those tests varying the power, we found that the optimal condition for dewetting nanoparticles was 2.6 W. Such value was kept fixed throughout the work.

To ascertain the mechanisms of the laser-induced dewetting and confirm the nature of the process, a morphological analysis was conducted on the dewetted particles for different film thicknesses. The average size increases with the thin film initial thickness in 4 nm, 5nm, and 6 nm samples, whereas for 7 nm, the particle average diameter decreases. For the 4 nm, 5nm, and 6 nm samples, the particle average diameter correlates with $h^{5/3}$ ($R^2 = 0.986$), indicating that the observed process follows a spinodal decomposition mechanism (Figure 46 g). However, on the 7 nm sample (Figure 45 d and h), it can be observed that some particles were removed, leaving empty hollows in the glass substrate. Such deviation from the trend can be attributed to the increased absorption of the 7 nm thick Cu film, given the initial presence of a thicker film with respect to the other cases.

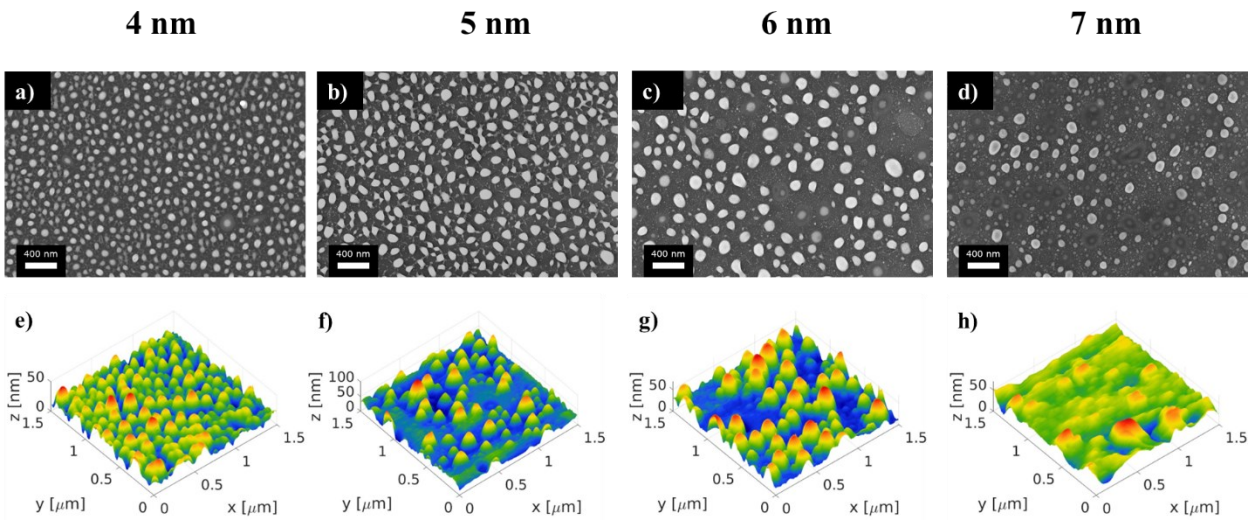

Figure 46: Copper nanoparticles obtained by LID of a Cu thin film of different thicknesses from 4 nm to 6 nm observed at the FESEM (a-d) and the AFM (e-h).

In Figure 47, the correlation between the average particle diameter and $h_0^{\frac{5}{3}}$ is shown together with the particle size distributions obtained from the different initial thicknesses. From Figure 47 a) it can be observed a very good linear correlation exists ($R^2 = 0.986$) for thickness up to 6 nm confirming the dewetting follows a spinodal mechanism. However, this trend is not observed as the initial thickness reaches 7 nm.

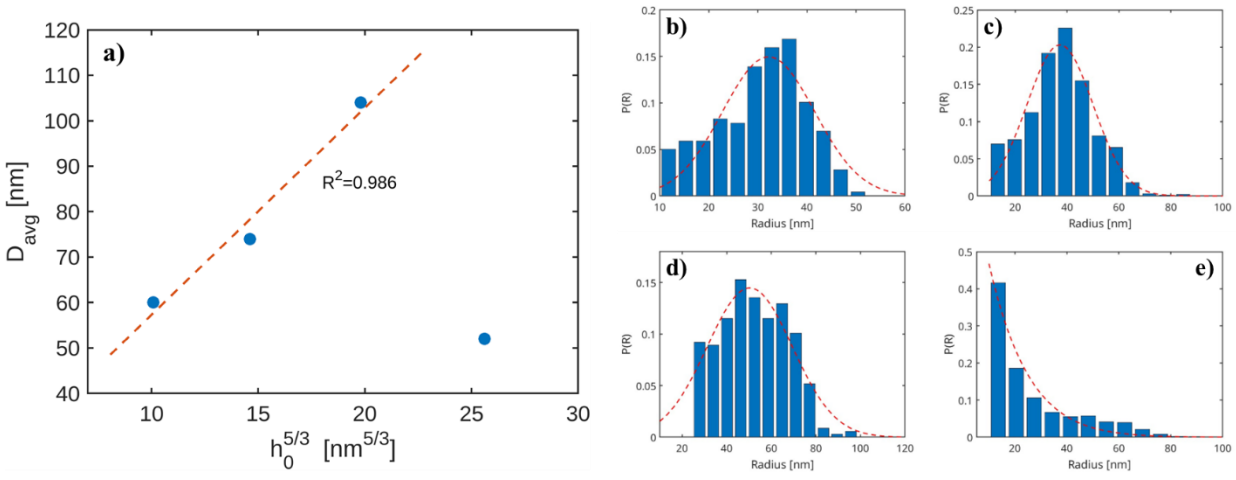

Figure 47: Average particle diameter as function of the initial film thickness a). Size distribution of the particles obtained by dewetting of different initial film thickness: 4 nm b), 5 nm c), 6 nm d) and 7 nm e).

4.3 GLASS ETCHING

After obtaining the nanoparticles on the substrates, plasma etching was used to obtain a nanopillar structure using the nanoparticles as masks. Pure silica substrates can be etched in a reactive ion etching (RIE) system using a fluorine-based atmosphere such as CF_4 or CHF_3. However, ordinary soda-lime glass contains a non-negligible amount of non-volatile oxides (Na_2O, CaO, and Al_2O_3), which the sole action of the fluorine plasma cannot remove. For this reason, we choose a mixed atmosphere containing both CF_4 and Ar. The former produces high-volatility Si compounds, whereas the latter exerts a physical etching action to remove the other oxides not removed by chemical reactions.

However, adding Ar in the etching atmosphere can affect the duration of the shadow mask and limit the maximum etching depth. In fact, even if Cu forms non-volatile compounds with fluorine, it is susceptible to the action of physical sputtering of Ar ions. For this reason, the redeposition of non-volatile oxides produces self-masking in the RIE process. This can produce smaller nanoscale features that introduce a roughness on a much shorter scale than the nanopillar size to be obtained.

For our processes, the substrates were etched in Ar/CF_4 (30/20 sccm) plasma using a SAMCO-RIE 10NR for 2, 4, 6, 8, and 10 minutes. The chamber pressure was fixed at 11 Pa, and the RF generator power was set to 200 W. Before starting the process, the chamber was conditioned with a 5-minute treatment in O_2 plasma at 100 W and 50 Pa to remove any possible carbon contaminants that may interfere with the chemistry of CF_4 plasma. After etching, samples were cleaned for 10 minutes in a $FeCl_3$ 0.1 M solution, washed twice in water, and cleaned again in an acid piranha solution. Substrates were washed twice in ultrapure water and ethanol and dried under a chemical hood in a clean environment.

To explore the effect of the etching process on the nanopillar and their surface roughness, we changed the RIE process duration i.e., 2 min, 4 min, 6 min, 8 min, and 10 min, obtaining pillars with a height of 26 nm, 68 nm, 112 nm, 98 nm, and 79 nm respectively (see Figure 48 and Figure 50). From the SEM analysis, etching for times up to 6 minutes produced an increase in the depth of the nanopillar formed. At the same time, it is clear that the nanopillar height decreases for longer etching times (8 and 10 min), producing an increasing secondary roughness that originates from the so-called grassing phenomenon in the RIE process.

The secondary or small-scale roughness generated can be estimated from SEM analysis, illustrated in Figure 49, to be on the order of 10-15 nm. For this reason, the duration of the process with the proposed parameters can be used to control the depth of the nanopillar and the small-scale roughness, providing the nano-hierarchical features.

The following experiments found optimal results for 6 min etching, providing enough depth and secondary roughness to obtain the nano-hierarchical structures for the targeted applications (Superhydrophobic surfaces and SERS).

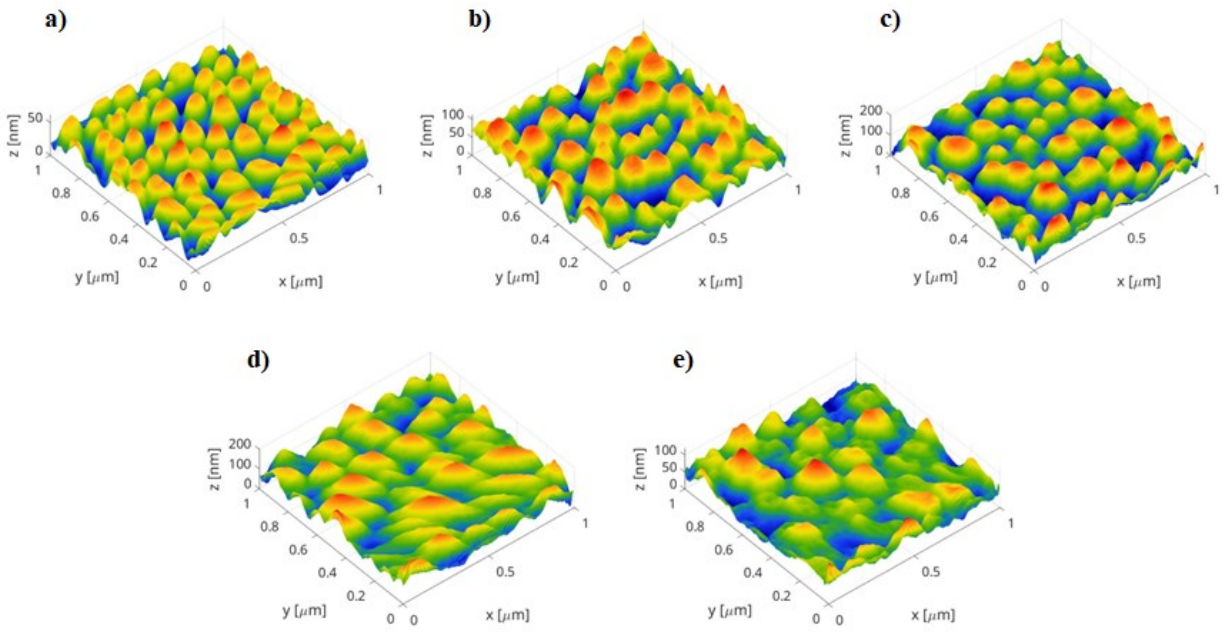

Figure 48: Atomic Force Microscopy (AFM) image of the soda-lime glass etched for different times: 2 min (a), 4 min (b), 6 min (c), 8 min (d) and 10 min (e).

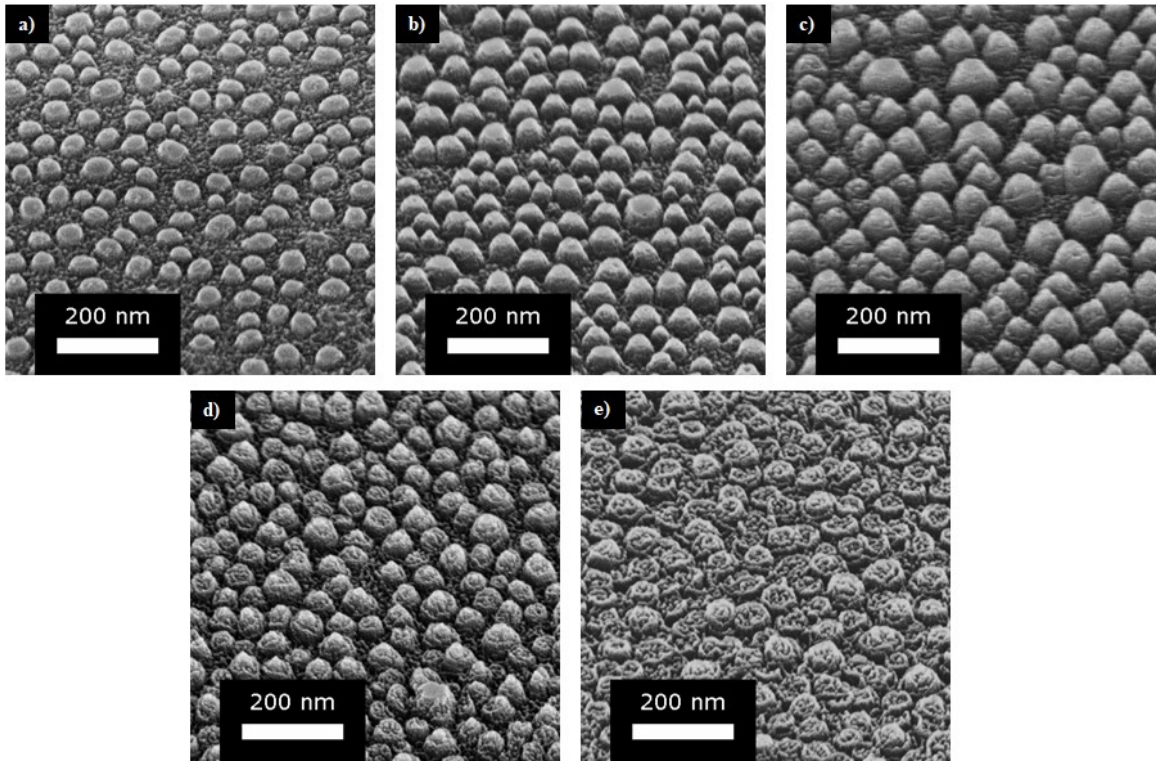

Figure 49: Tilted (50°) SEM images of the soda-lime glass etched for different times: 2 min (a), 4 min (b), 6 min (c), 8 min (d) and 10 min e).

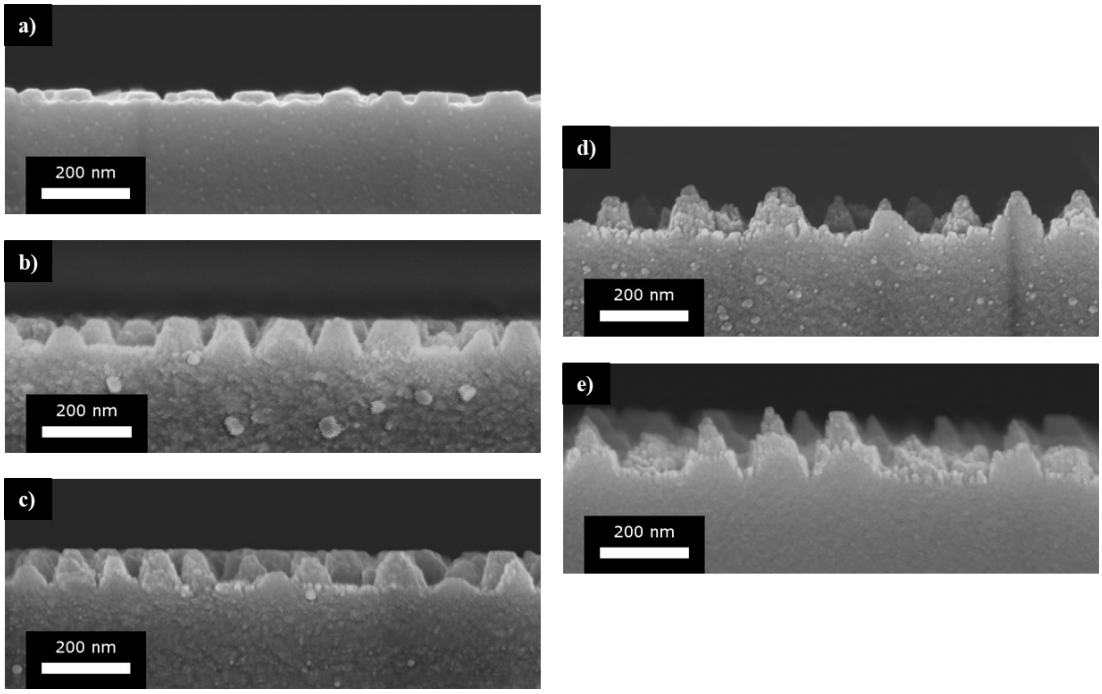

Figure 50: Cross-section SEM images of the soda-lime glass etched for different times: 2 min (a), 4 min (b), 6 min (c), 8 min (d) and 10 min e).

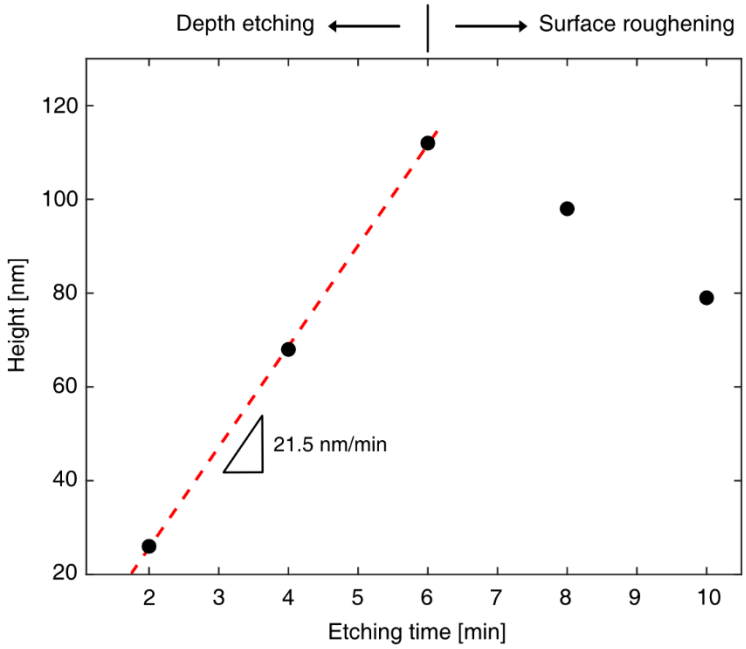

Figure 51: Plot of the pillar height as a function of the etching time.

4.4 SUPERHYDROPHOBIC FUNCTIONALIZATION

Nanopillar substrates can be treated with chemical coating to produce water repelling substrates. At present, very deep nanopillars are needed to obtain such interfaces (typically higher than 200nm), and usually, they are realized on pure silica glass substrates, which are very expensive and mostly used in niche applications. In our case, we used the nanopillar obtained by the method exposed above with a hierarchical nanoscale roughness as a base to obtain superhydrophobic surfaces.

We recall here that a surface is called wettable if the liquid surface tension is lower than a critical surface tension value γ_C. For instance, given a water surface tension γ_W=72.3 mN m^{-1}, a surface is considered hydrophobic if its critical surface tension is below the threshold of 35 mN m^{-1}. Different fluorinated silanes, including perfluorooctyltriethoxysilane[103], perfluorooctyltrimethoxysilane[103], and perfluorodecyltrichlorosilane[31], have been so far used for the functionalization of glass substrates, aiming at reducing the glass critical surface tension (275 mN m^{-1})[104] to prepare superhydrophobic surfaces.

However, no previous work has employed heneicosafluorododecyltrichlorosilane (HFDS) for the functionalization of pillar-based nanostructure, even if this fluorosilane is reported to be the molecule allowing the preparation of functionalized surfaces with the lowest critical surface tension[105], i.e., 6-7 mN m^{-1}. Unfortunately, HFDS is only slightly soluble in most solvents, and due to the length of its side chain, its solutions tend to polymerize due to the adsorption of water from air moisture[106]. For this reason, we explored the usage of HFDS by employing a vapor phase deposition approach [107].

The glass sample coated with the 5 nm Cu thin film was processed with a nanosecond laser, treated for 8 min in RIE, and functionalized with the HFDS. A small quantity of the silane was placed with the sample in a desiccated glass vessel and treated for 2h30min at 120°C. The sample was removed from the vessel and treated at 100°C for 30 minutes to remove the physisorbed molecule from its surface. After washing the samples in methanol, toluene, and water and drying them under a chemical hood, the contact angle of the surface was measured with a 2 µl volume drop.

The outcome of the process was a superhydrophobic substrate (Figure 52), exhibiting a water contact angle of 157° (Figure 52c). For comparison, the water contact angle on a flat glass surface was 114° (Figure 52a). As shown in the figure, the thermal desorption treatment at 100°C was of utmost importance to enhance the contact angle since, for non-treated samples, it was lowered to only 143° not reaching superhydrophobicity (Figure 52b). Such a high contact angle for a nanotextured structure was obtained for nanopillars of 110nm height, which is unprecedented in the literature where more considerable heights must commonly be employed. The nano-hierarchical design lowers the surface energy and, combined with the nanopillar shape, achieves such a high contact angle.

In addition, one of the most significant advantages offered by LID is the possibility of patterning the surfaces to create nanostructured zones selectively and made superhydrophobic upon functionalization in contrast to the non-patterned zones (Figure 52d).

Due to their multiple applications, the obtained structures are of great technological interest. For instance, they can also be used to create anti-reflection surfaces as they give a continuous and smoother refractive index transition between the ambient air and the substrate if compared to the abrupt change of a flat surface [108].

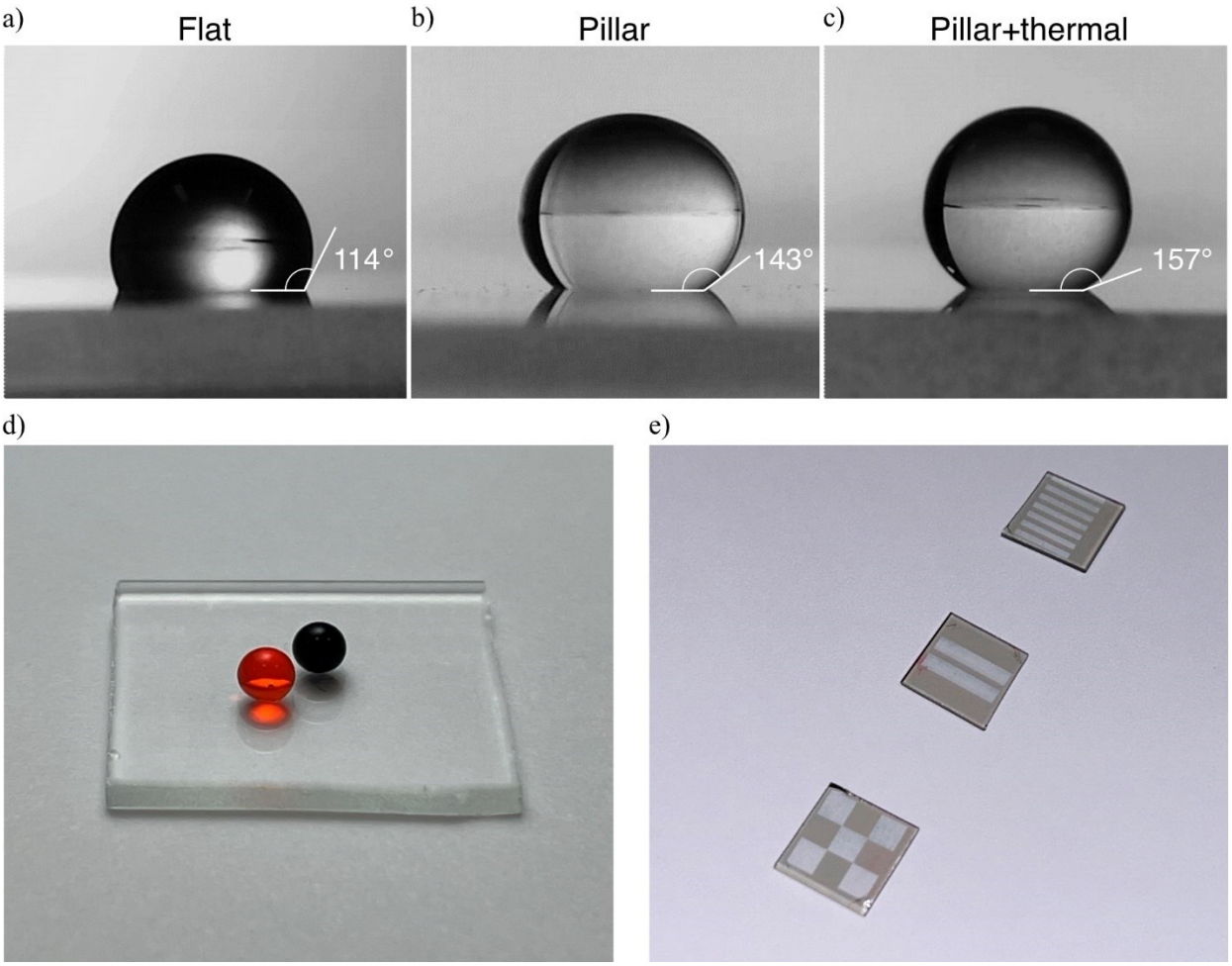

Figure 52: Contact angle of a water droplet on the fluorosilane functionalized flat glass (a) and nanostructured glass without (b) and with (c) thermal treatment after functionalization. Droplets of dye water solutions on the superhydrophobic nanostructured glass (d). Different LID patterns of a 5nm Cu thin film on a glass substrate to obtain selective superhydrophobic regions (e).

4.5 THIN-FILM DEPOSITION AND FABRICATION OF THE SERS SENSOR

A 40 nm thickness silver and gold thin film was deposited by RF sputtering (Moorfield) at a pressure of 3 Pa and RF power of 75 W onto the etched substrate immediately after the acid piranha cleaning. The diffuse transmittance $\%T_{diff}$ and diffuse reflectance $\%R_{diff}$ spectra of the samples

in the wavelength range from 350 to 900nm were recorded with a Shimadzu UV-2600i UV-visible spectrophotometer. Absorbance Abs of the samples were calculated as:

$$\text{Abs} = log_{10}\left(\frac{1}{A}\right) = -\log_{10}\left(\frac{100 - \%T_{diff} - \%R_{diff}}{100}\right) \quad (4.91)$$

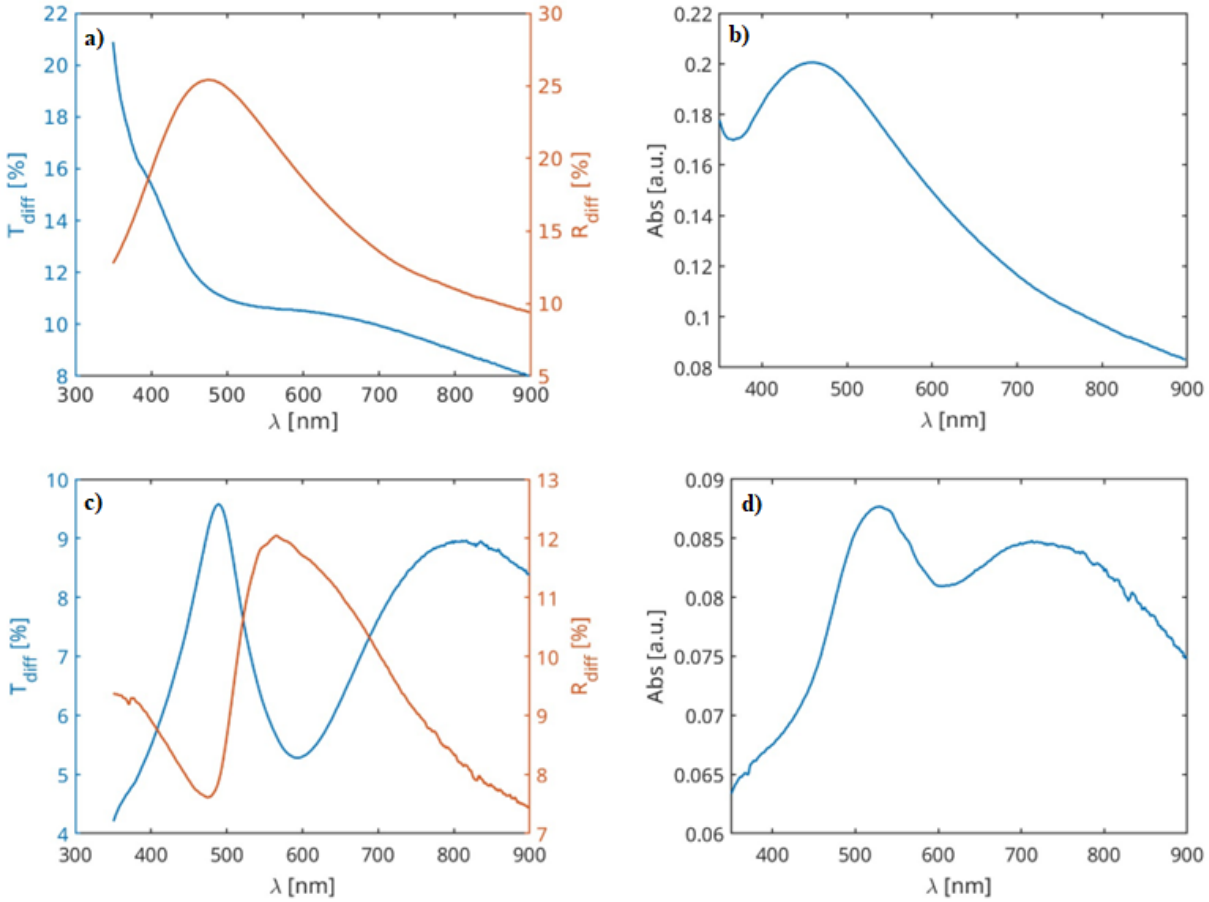

Figure 53: UV-visible spectra obtained in diffuse transmission and diffuse reflection for the silver-coated (a) and gold-coated (c) sensors. Calculated absorbance for the silver-coated (b) and gold-coated (d) sensors.

Substrates were imaged at FESEM after coating with a platinum coating layer (~ 5nm) in a Quorum 150 DC sputtering, and images of both sensors are reported in Figure 54.

To study the utility of the prepared sensor for SERS application, the optical response of the pillar at the excitation and Raman scattering wavelength were studied by means of near-field simulations. The total electrical field E in the surrounding of a single coated pillar (see Figures Figure 55 and Figure 56), induced by plane wave excitation, was calculated using a BEM approach in SCUFF-EM [109]. Optical data for gold and silver were taken from Johnson and Christy. The refractive index of soda-lime glass was assumed to equal 1.52 [110].

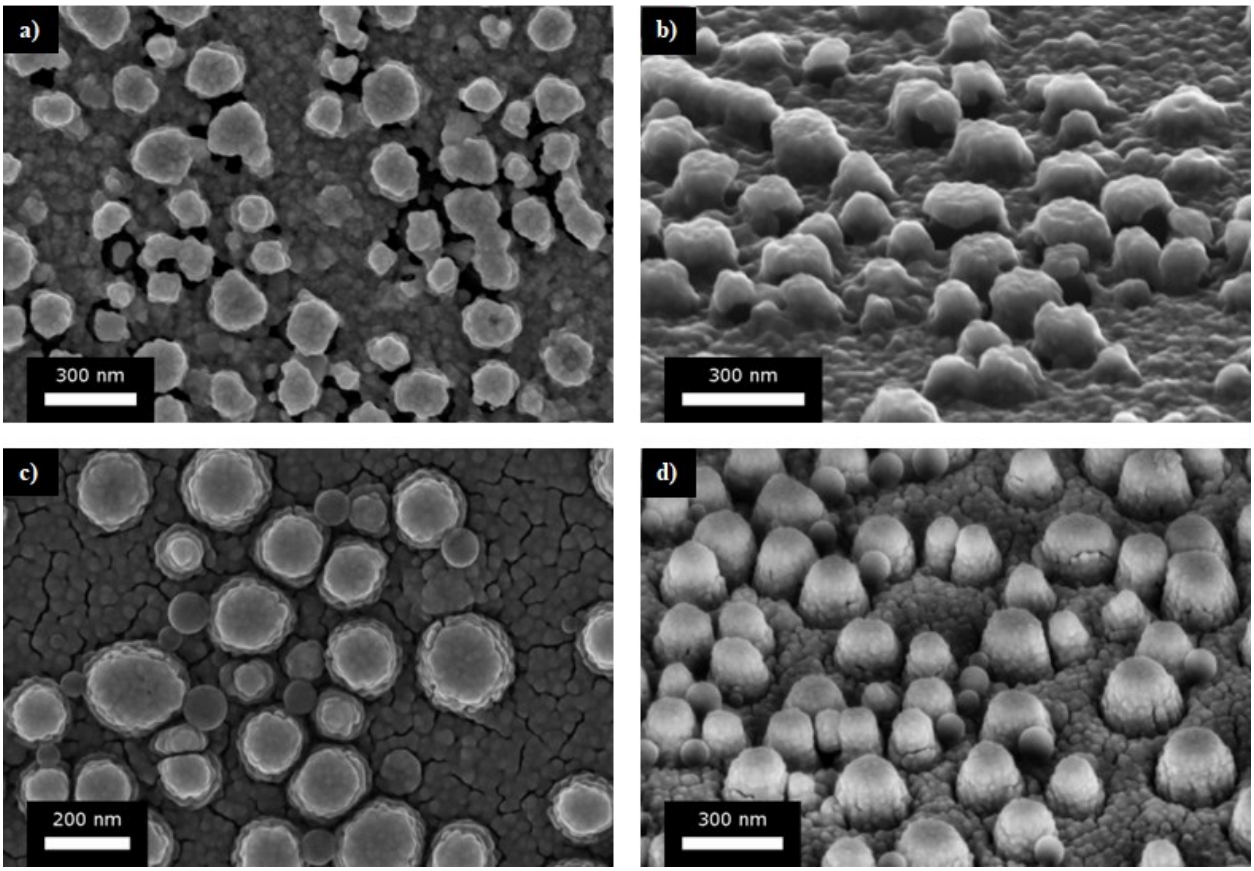

Figure 54: SEM images of silver-coated samples a) and b). SEM images of the gold-coated samples after the deposition of the nanoplastic contaminants c) and d).

The SERS Enhancement Factor (SEF) at a point $\vec{x}$ has been calculated as the product between the field enhancement factor at the excitation wavelength λ and the one at the Raman scattering wavelength $\lambda_{exc} + \Delta\lambda_{RS}$.

$$SEF(\vec{x}, \lambda_{exc}, \lambda_{RS}) = \left|\frac{E(\vec{x}, \lambda_{exc})}{E_0}\right|^2 \cdot \left|\frac{E(\vec{x}, \lambda_{exc} + \Delta\lambda_{RS})}{E_0}\right|^2 \quad (4.92)$$

where $E(\vec{x})$ is the total electrical field in the point $\vec{x}$ and E_0 is the incident electrical field.
The SEF values were calculated for both sensors at three different excitation wavelengths, i.e. 532 nm, 633 nm, and 785 nm, according to the chosen analyte band, see Figure 57 and Figure 58. In particular, the Raman bands of interest are the aromatic breathing mode of MBA (1586 cm^{-1}) for the silver-coated sensor and the aromatic breathing mode of polystyrene (1001 cm^{-1}) for the gold-coated one.
A Surface Averaged SERS Enhancement Factor (SASEF) has been calculated as the integral mean of the SEF over the upper pillar section profile γ:

$$SASEF(\lambda_{exc}, \lambda_{RS}) = \frac{1}{\gamma} \oint_{\Sigma} SEF(\vec{x}, \lambda_{exc}, \lambda_{RS}) d\gamma \tag{4.93}$$

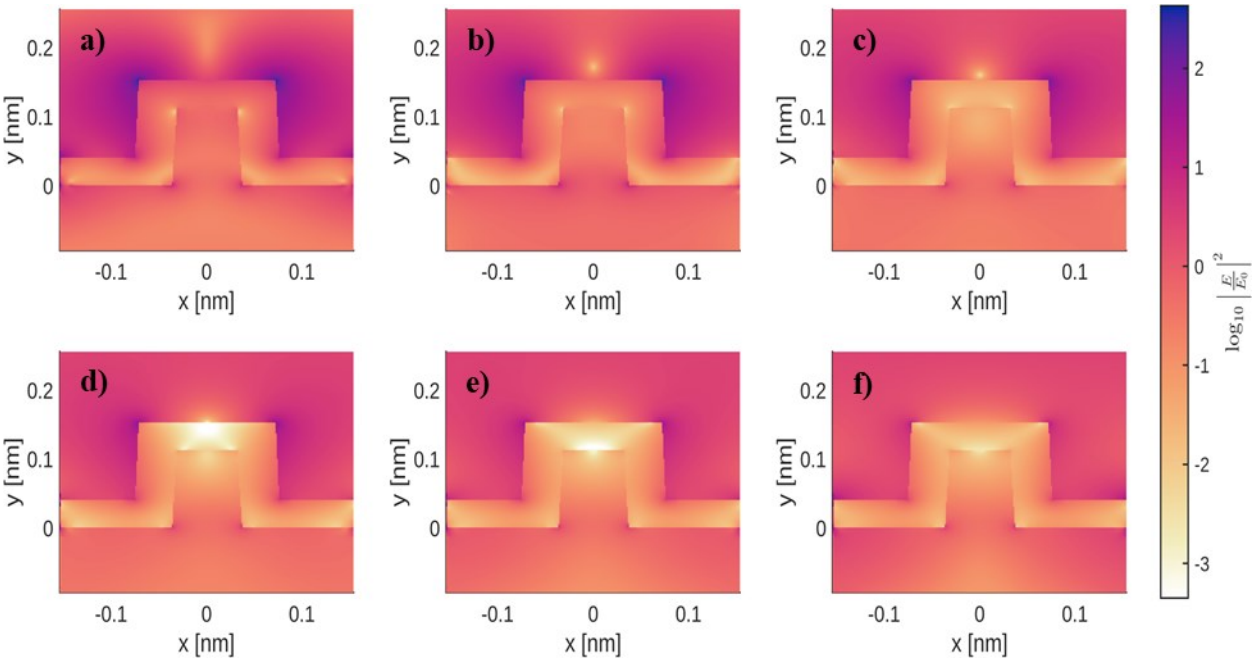

Figure 55: Electric field enhancement factor for a single silver-coated pillar at different wavelengths.

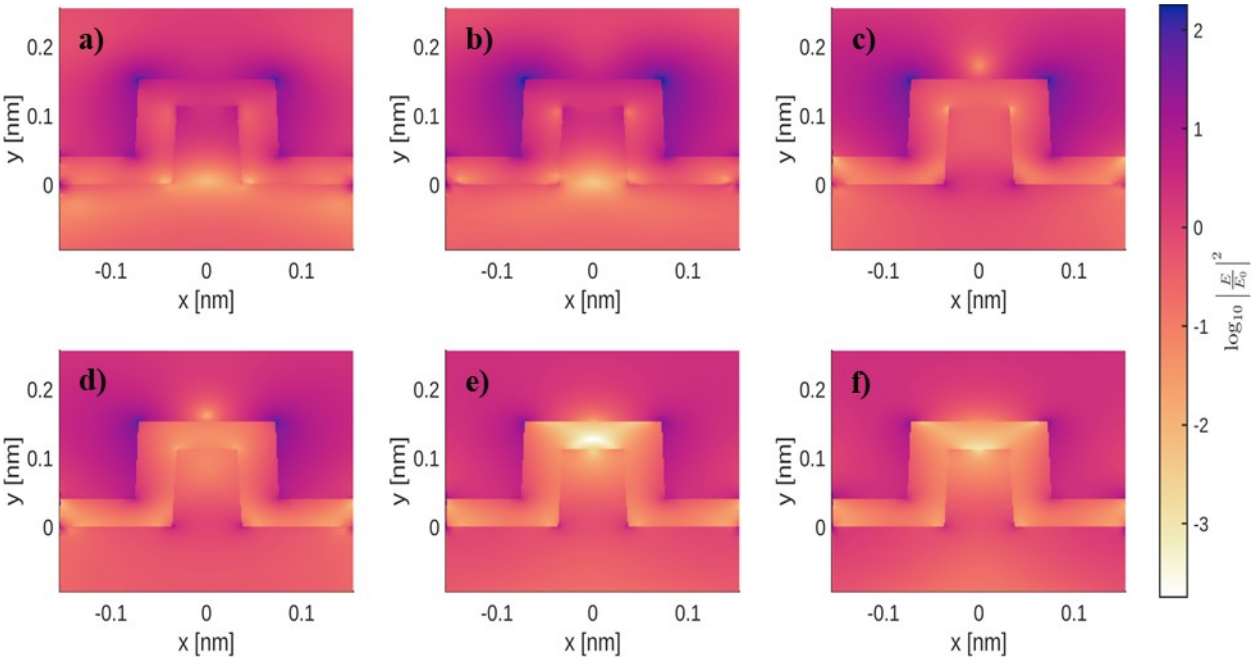

Figure 56: Electric field enhancement factor for a single gold-coated pillar at different wavelengths.

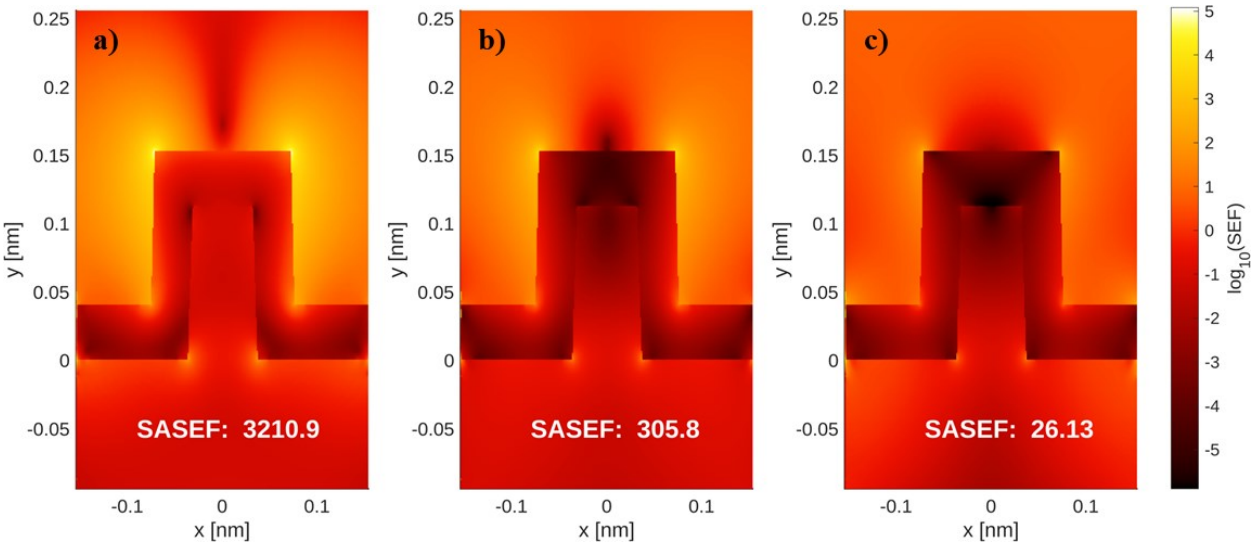

Figure 57: SERS enhancement factor (SEF) for a single silver-coated pillar at different wavelengths.

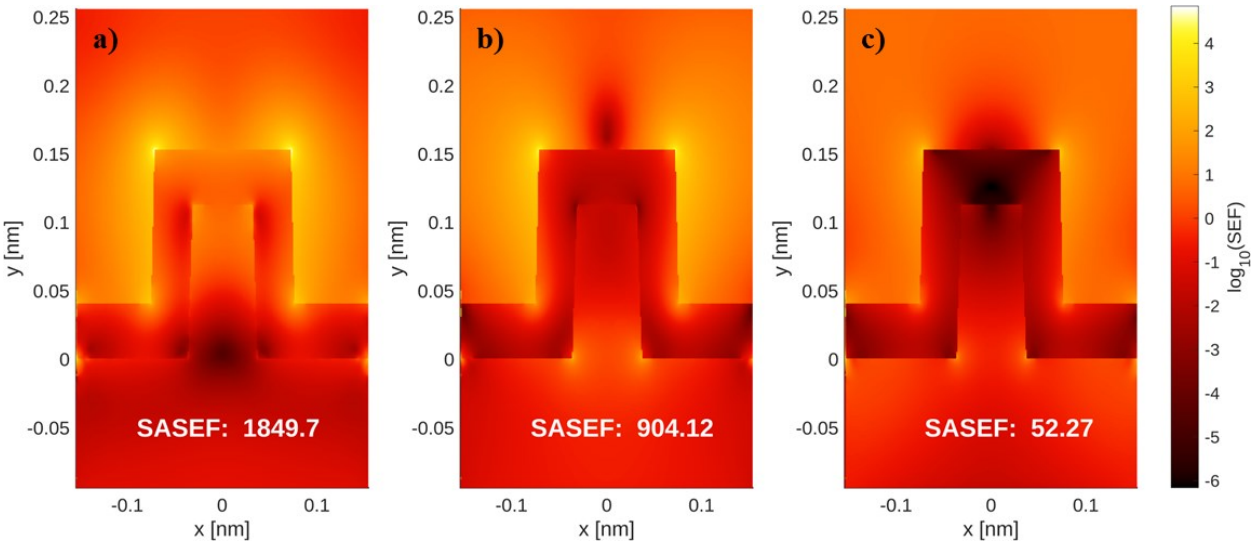

Figure 58: SERS enhancement factor (SEF) for a single silver-coated pillar at different wavelengths.

The calculated SASEF suggests that the silver-coated and gold-coated perform best at an excitation wavelength of 532 nm, with the former offering almost a double enhancement if compared to the latter. At 633 nm, the gold performs around three times better than silver, offering a SASEF of 904.12 vs 305.8. Finally, for an excitation wavelength of 785 nm, both the sensors could be more effective, due to their much lower SASEF. Under these conditions, a structure with a higher aspect ratio, offering longitudinal resonance modes towards the near-infrared region, could be more efficient.

4.6 SERS MEASUREMENTS

The realization of SERS substrate on gold-coated pillar has already been intensely studied by Yue et al., 2022[111]. However, Yue's paper uses a complicated and expensive fabrication process involving an electron beam lithography step. We employed the nano-hierarchical glass substrates coated with a 40 nm layer of silver and gold by RF sputtering to obtain SERS sensors. From the SEM analysis (Figure 54 a-b)), the nanoscale roughness is present on the silver-coated substrates where the underlying glass roughness has favored the roughness of the deposited Ag layer. Those substrates exhibit a broad LSPR band with a maximum located at a wavelength of 461 nm due to the transversal resonance mode in the coated nanopillar (Figure 53 a) and b)).

To test the performance of the Ag-coated substrates, we employed 500 nM 4-mercaptobenzoic acid (MBA) in water, which is commonly used to this aim. Indeed, due to aromatic ring vibrations, MBA shows two very intense bands located at a Raman shift of 1076 cm^{-1} and 1586 cm^{-1}, respectively. A 20 µL drop of 500 nM water solution of 4-mercaptobenzoic acid (MBA) was deposited onto the silver-coated sensor and a silver-coated flat glass.

The laser excitation wavelength was selected according to the absorption spectra (Figure 53), and the results of the near-field simulation to achieve an optimal Surface Averaged SERS Enhancement Factor (SASEF)Figure 57 and Figure 58 offered by our pillar-base sensor.

In the previous paragraph, the SASEF was employed to quantitatively indicate the field enhancement due to LSPR modes for a specific Raman band at a particular excitation wavelength. In our case, we observe that for the 1586 cm^{-1} MBA band that SASEF at $\lambda_{EXC} = 532\ nm$ is roughly ten times higher than SASEF at $\lambda_{EXC} = 633\ nm$ and around 120 times higher than SASEF at $\lambda_{EXC} = 785\ nm$ (see Figure 3e).

For this reason, we fixed the excitation wavelength to 532 nm, and the intensity of the strongest band obtained from MBA measurement on the SERS sensor, i.e., 1586 cm^{-1}, was compared with the intensity of the same band obtained on a 40 nm flat silver film (see Figure 59).

The intensity enhancement factor (IEF) for the silver-coated sensor was calculated as:

$$IEF(\lambda) = \frac{I_{SERS}(\lambda_{EXC}, R_s)}{I_{flat}(\lambda_{EXC}, R_s)} \tag{4.94}$$

Where $I_{SERS}(\lambda_{EXC}, R_s)$ and $I_{flat}(\lambda_{EXC}, R_s)$ are the intensity of the band at 1586 cm^{-1}, obtained on the silver-coated SERS sensor and flat glass, respectively, at a given excitation wavelength λ_{EXC} and Raman Shift R_s.

As a result, the IEF given by the nanotextured surface coated with Ag, calculated with (4.94)(4.96) is equal to 176.7.

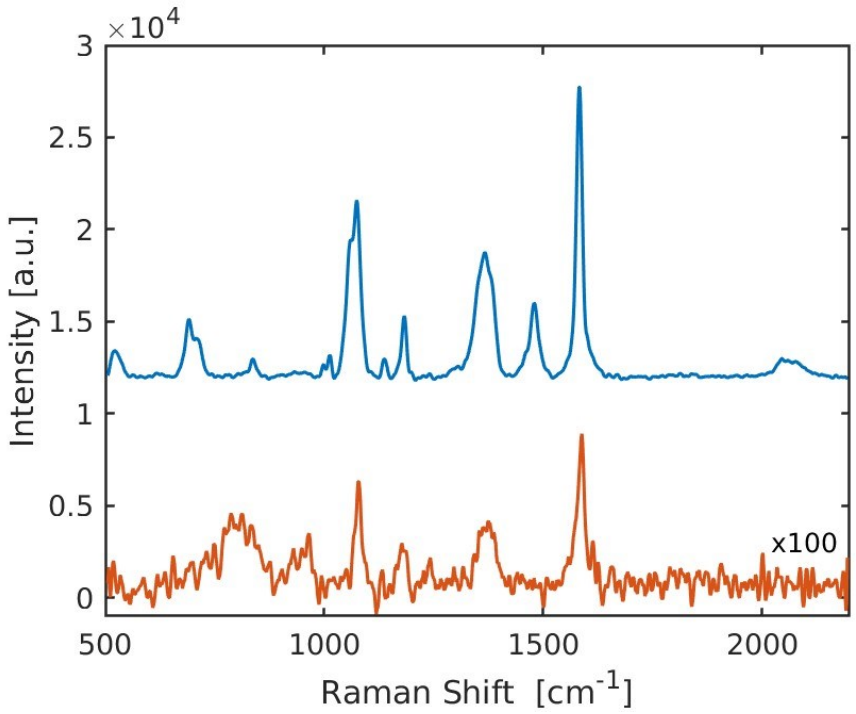

Figure 59: SERS spectra of an MBA 500 nM solution obtained on a flat Ag thin film (red line) and on the silver-coated pillar-based sensor (blue line).

In addition, the gold-coated sensor was tested for nanoplastic detection. For this purpose, a 5 µL colloidal suspension of 100 nm latex nanobeads diluted from the purchased solution at different concentrations (700 µg mL^{-1}, 70 µg mL^{-1}, 7 µg mL^{-1}, 700 ng mL^{-1}, 70 ng mL^{-1}) was deposited on the gold-coated sensor. After droplet deposition, the samples were slowly dried under a gentle Ar flow before the measurements.

For the SERS measurement on the silver and gold sensors, we employed a Renishaw InVia Raman microscope with a 50x objective (NA=0.75) and laser excitation wavelength of 532nm and 633 nm, respectively. Before running the measurement, the system was calibrated by referencing the Silicon band peak at 520 cm^{-1}.

To create a calibration curve, the Normalized Raman Intensity I_{NORM} has been calculated for each spectrum as follows:

$$I_{NORM} = \frac{I}{P_{exc} \cdot t_{exp} \cdot n_{acc} \cdot NA} \tag{4.95}$$

where P_{exc} is the power of the exiciting laser (in mW), t_{exp} is the exposure time, n_{acc} is the total number of accumulations and NA is the microscope objective numerical aperture.

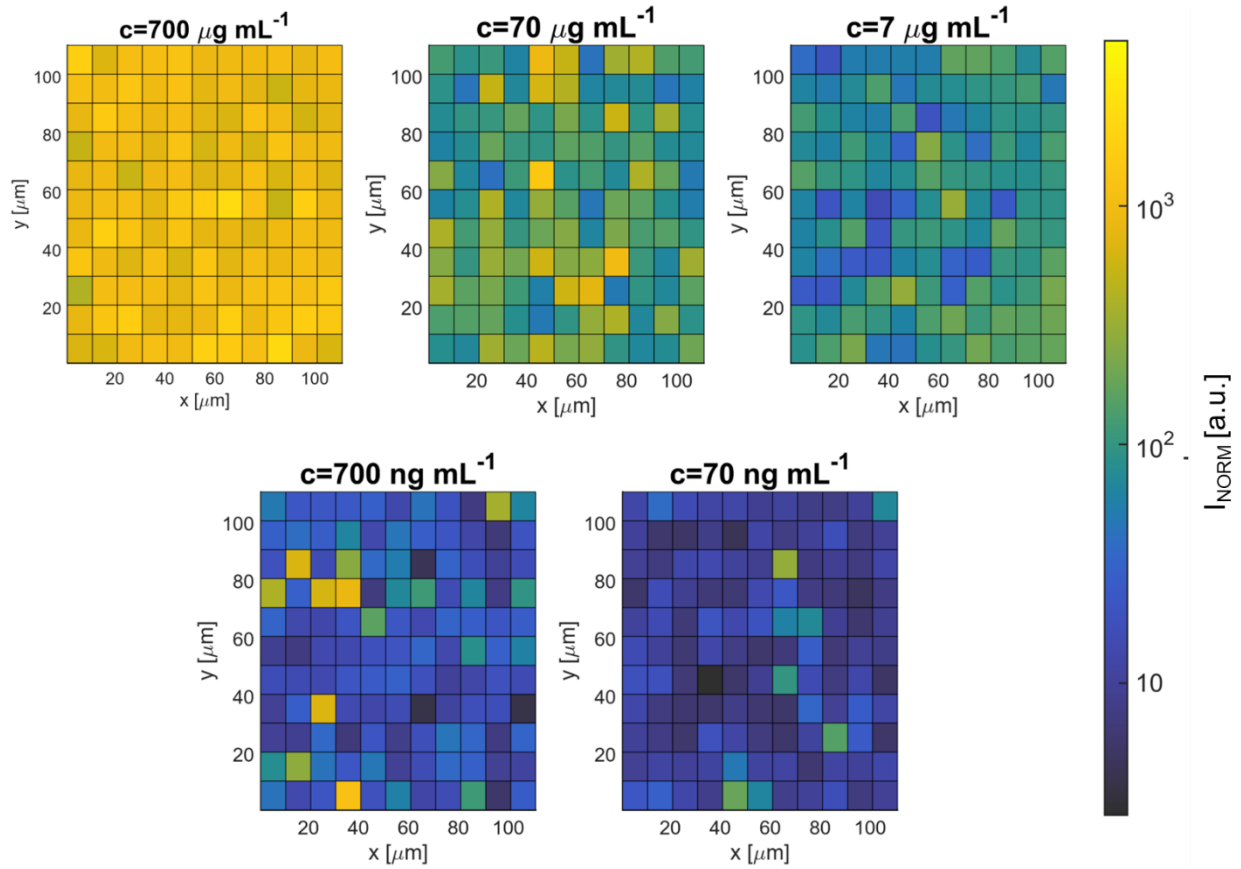

Figure 60: Normalized Raman intensity maps for PS NPs at different concentrations from 70 µg mL^{-1} to 70 ng mL^{-1}.

A digital approach (see Figure 61) was also adopted to process SERS data and obtain a meaningful calibration curve.

Indeed, the metric used is based on the digital SERS counting as in [112] to act as a thresholding function multiplied by the actual counts of the normalized peak intensity at 996 cm^{-1}. Such a weighted average named combined intensity I_{COMB} can be expressed as:

$$I_{COMB} = \sum_{n=1}^{N} w(I_n)\, I_n(n\,\Delta x, n\,\Delta y),\; w(I) = \begin{cases} 0, & I < I_B + 3\sigma_B \\ 1, & I \geq I_B + 3\sigma_B \end{cases} \qquad (4.96)$$

Where N is the number of points measured in the map, $I_n(n\Delta x, n\Delta y)$ is the SERS intensity of the peak at point $(n\Delta x, n\Delta y)$, and $w(I)$ is a threshold function that selects the signals that are at least 3 times above the noise level I_{blank} registered from a blank substrate without NP. The obtained calibration curve reporting I_{COMB} versus the PS NPs concentration is reported in Figure 62 b). The linear fitting of the displayed data is obtained by the equation $I_{COMB} = 0.53c + 1.64$, with R^2 = 0.98.

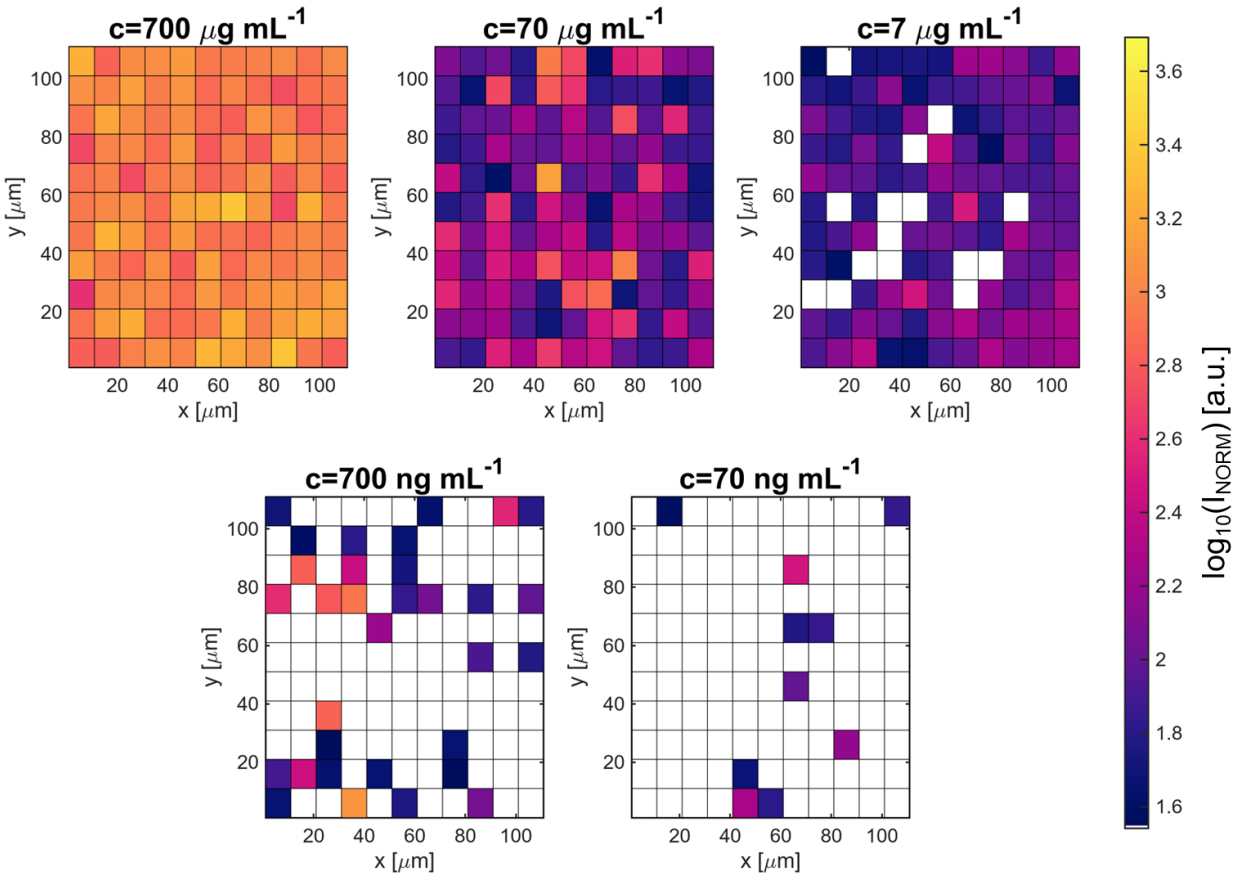

Figure 61: Normalized Raman intensity maps for PS NPs at different concentrations from 70 µg mL^{-1} to 70 ng mL^{-1}. Points whose intensity is lower than $I_B + 3\sigma_B$ are displayed in white.

A calibration curve was obtained by plotting the average I_{NORM} vs the sample concentration as shown in Figure 62 a). The regression line of such a curve, in a double logarithmic scale, was found to be y=0.398x+1.764.

However, the limit of detection (LOD) was also estimated according to a digital [113] count analysis. The average normalized intensity at 996 cm^{-1} I_{BLANK} and its standard deviation $\sigma_{BLANK}$was calculated for a blank sensor, respectively 15.5 and 1.4.

For each concentration, the number of point I_{THR}whose intensity is greater or equal to $I_{BLANK} + 3\sigma_{BLANK}$ against concentration was calculated and reported in Figure 62 b). Both samples at 700 µg mL^{-1} and 70 µg mL^{-1} are saturated with the PS NPs and show a I_{THR} equal to 144.

Samples at lower concentrations show a linear trend (R^2=0.99) and are described by a regression line of equation y=0.53x+1.64. The LOD was estimated as the concentration at which only one point has an intensity value above I_{THR} . This LOD value, calculated as 0.8 ng mL^{-1}, is easily obtained as the regression line y-intercept in the double logarithmic plot. Such a value is almost three orders of magnitude lower than the actual best value reported in the literature[114].

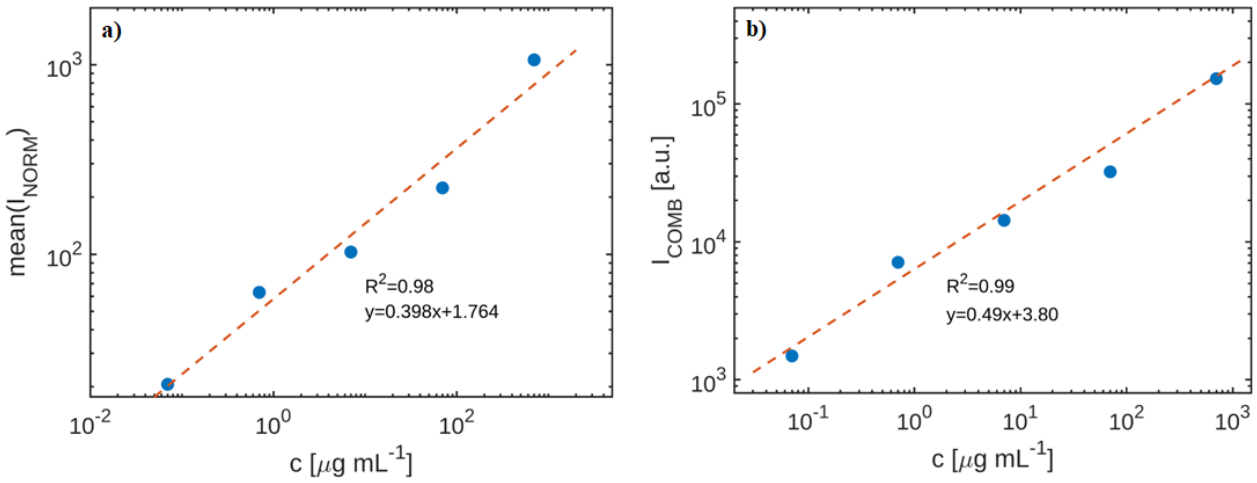

Figure 62: Calibration curve of the mean normalized intensity (a) and combined intensity (b) as a function of sample concentration.

Chapter 5
SOFTWARE TOOLS FOR ADVANCED MICROSCOPY

The optimization of the preparation process of nanomaterials and nanostructured materials often requires to fully characterize the obtained samples from the surface morphology point of view. This characterization is possible with different instruments such as SEM, AFM, or profilometer.
On the one hand, AFM offers a lateral resolution comparable to the atomic size but can operate within a z-range of 100 μm at most [115]. On the other hand, the sample height does not limit modern SEM and offer a resolution of up to half a nanometer. Still, they usually cannot provide topographical information on the vertical direction. Finally, optical profilometers are usually limited to a resolution between 500 nm and 1 μm and do not allow surface reconstruction with tiny features.
During this thesis work, much effort was devoted to the characterization of substrates and the development of tools to ease and improve such processes. This chapter reports on the contribution given to developing two approaches for the tridimensional reconstruction of laser machined surfaces using an SEM exclusively: the *reconstruction from four quadrants of backscattered electron detector* and the *reconstruction from image z-stack*.

5.1 SURFACE TRIDIMENSIONAL RECONSTRUCTION THROUGH FOUR QUADRANTS BACKSCATTERED DETECTOR

This section is largely based on the published paper *Regularization techniques for 3D surface reconstruction from four quadrant backscattered electron detector images*[116].
In a Scanning Electron Microscope (SEM), different types of interaction may occur when the primary electron beam impinges on the sample surface. Primary electrons may be scattered either inelastically, with the production of secondary electrons, or elastically, giving rise to a phenomenon known as backscattering. Backscattered electrons (BSEs) have high kinetic energy, typically higher than 50 eV, and compose most of the signal emanating from the specimen [117].
The backscattering coefficient η_{BSD} is defined as the ratio between the backscattered electron current leaving the sample i_{BSD} and the primary electron current entering the sample surface i_P, namely [118]:

$$\eta_{BSD} = \frac{i_{BSD}}{i_P} \tag{5.97}$$

Such quantity is a function of the mass number $\mathcal{Z}$ of the atoms involved in the scattering process that are present in the sample. For this reason, BSEs are usually employed for obtaining images with compositional contrast, allowing to make the distinction between light ($\eta_{BSD} \simeq 10\%$) and heavy elements ($\eta_{BSD} \geq 50\%$). Indeed, in a sample composed of multiple phases, the ones containing lighter elements will appear relatively dark (lower number of emitted BSEs). On the contrary, the ones containing heavy elements will appear with higher brightness (higher number of emitter BSE).

A critical role in the final SEM analysis with BSE is played by the detectors and their arrangement. For example, a standard Everhart–Thornley detector can be used for BSE if a negative bias is applied to its Faraday's cage to repel secondary electrons (SE), which have lower kinetic energy [118]. More recently, solid states diode detectors (SSDs) consisting of two semiconducting electrodes forming a p–n junction were introduced as BSE detectors. Typically, the two electrodes of the junction are constituted of Si or Ge doped with As/Ga and As/P/Sb, respectively [1]. The SSDs are available in different geometries, although the most common is the four quadrants arrangement (FQSSD) [119], shown in Figure 63.

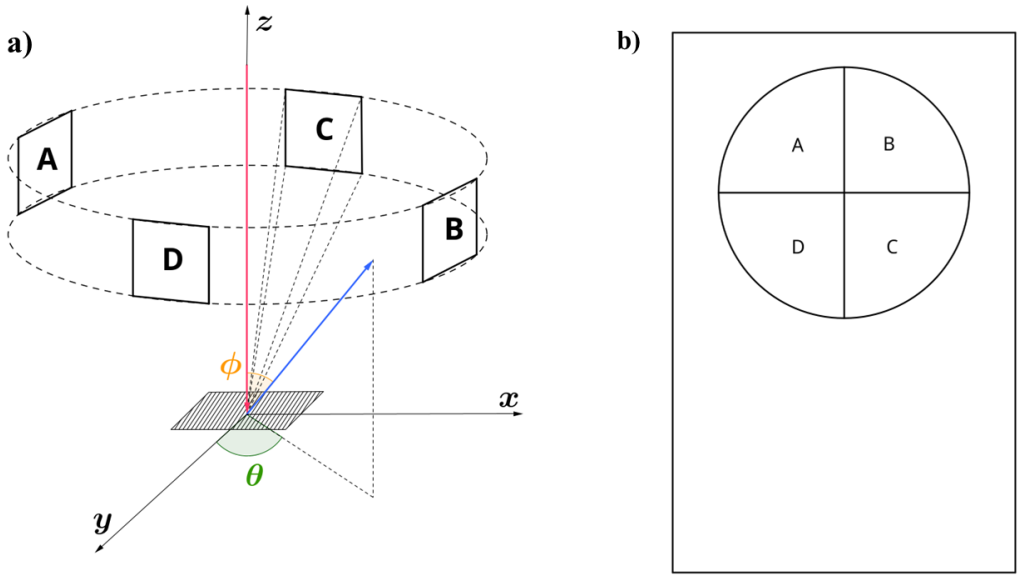

Figure 63: a) Details of BSE detection with a FQBSD and b) details of the FQBSD structure.

In the FQSSD, the compositional contrast is generally given as the sum of the signal of all the quadrants, but topographical information may also be obtained by combining the four signals in different ways. In particular, since the emitted BSEs also depend on the surface inclination, the

surface gradient can be calculated by combining the different quadrant signals as detailed in the following. The signal intensities counted by a detector can be expressed as [120]:

$$i_{BSD} = \frac{i_P \eta_{BSD}}{\pi} [d_A \tan(\phi_S) \cos(\theta_A - \theta_S) + c_A] \tag{5.98}$$

where θ_S and ϕ_S are the surface orientation expressed in polar spherical coordinates, d_A, c_A, and θ_A are constants that depend on the detector geometry. From the (5.98) we can obtain the derivative of surfaces elevation along the x direction as [121], [122]:

$$\frac{\partial z}{\partial x} = \tan(\phi_S) \cos(\theta_S) = \frac{c}{d} \frac{I_A - I_B}{I_A + I_B} \tag{5.99}$$

$$\vec{\nabla} \mathrm{z}(\mathrm{x}, \mathrm{y}) = \left(\frac{\partial z}{\partial x}, \frac{\partial z}{\partial y} \right) = \left(\frac{I_A - I_B}{I_A + I_B}, \frac{I_C - I_D}{I_C + I_D} \right) \tag{5.100}$$

Where I_A, I_B, I_C and I_D are the signal intensities as detected by each quadrant of the backscattered electron detector as shown in Figure 63.

In real applications, the quality of the height reconstructions obtained by these formulas is largely dependent on the alignment, sensitivity, and dynamic ranges of the BSD detectors. Unfortunately, many older models of SEMs are still equipped with manual retractable BSD detectors, which are generally very difficult to align perfectly with the gun axis and may therefore, suffer an unbalanced electron count amongst the quadrants. In this case, the imbalance negatively affects the 3D reconstruction of the topography, introducing artificial gradients and biases. For this reason, modern instruments are typically equipped with either an InLens BSD detector or a pneumatic insertion and positioning system.

Here, we present a regularization approach to mitigate the distortions in the reconstruction of different types of surfaces for the worst and more common case of images collected in a Field Emission Scanning Electron Microscope (FESEM) equipped with a manual retractable FQSSD. Such regularization dramatically improves the surface reconstruction, and the choice for the optimal regularization kernel according to the surface type will be discussed. The algorithm discussed in this section was implemented in a Matlab code, the user interface of which is shown in Figure 64.

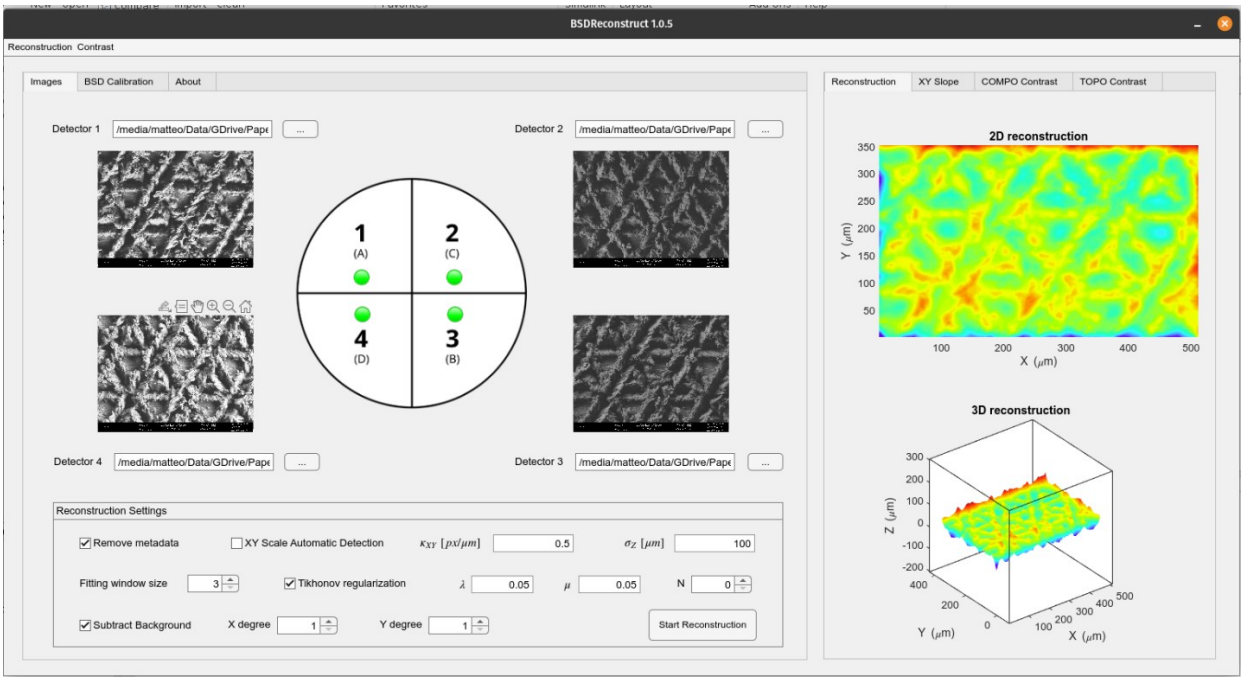

Figure 64: User interface of the FQBSD surface reconstruction tool realized in Matlab.

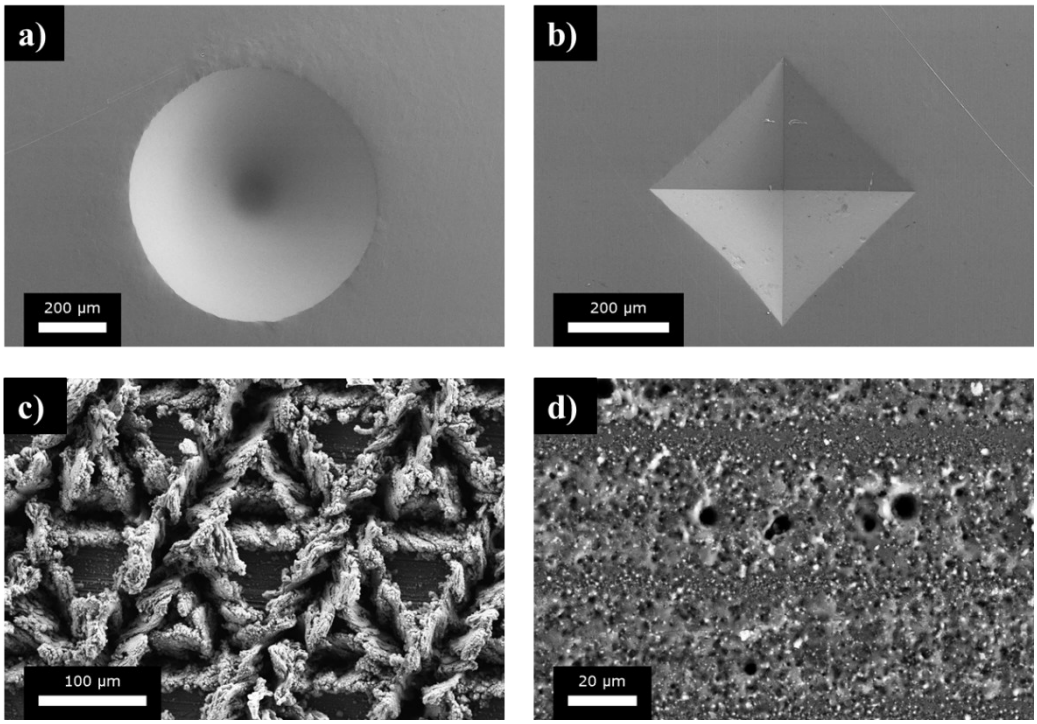

Figure 65: Image of the samples tested for the tridimensional reconstruction observed with SE2 detector at the FESEM.

All the samples studied in this work were analyzed with a Zeiss SupraTM 40 FESEM equipped with a K.E. Developments Type 211 four quadrant backscattered electron detector (FQBSD). Images from each quadrant of the FQBSD, reported in Figure 66, 69, 72 and 75, were acquired at an acceleration tension of 15 kV, setting the aperture to 60 μm and the working distances to 5 mm. The operator manually adjusted the brightness and contrast of the images on each sample to ensure adequate topographical information was contained in all the quadrant signals.
Silicon and steel samples were imaged without any preparation. In contrast, the laser-processed aluminum samples were coated via DC sputtering with a 5 nm platinum layer to mitigate charge accumulation. The height reference for the surface reconstruction was determined from measurements performed with a Taylor Hobson Intra Touch stylus profilometer. To obtain a reference to validate the reconstructions, a square region of 70 μm by 70 μm of the laser-treated silicon sample was measured with a Nanonics MultiView^{TM} 2000 AFM. The acquisition was performed using a 20 nm standard quartz tip at the 1:1 sensitivity mode, adopting a scan step of 145 nm in each direction. This step size was chosen to equal the FQBSD images resolution.
All the images were imported in MATLAB, and a custom code was created to obtain both the reconstruction and regularization of the surfaces. All the surface plots presented here were generated in Matlab employing the Colorcet perceptually accurate 256-color colormaps [123]. In general, the reconstruction of a surface by integrating its gradient field is a particularly tedious operation because it requires low-frequencies information, which is reduced by the derivative operation [124]. Indeed, the tridimensional reconstruction of a surface requires the integration of (5.100) to obtain the height profile given by:

$$\mathrm{z(x,y)} = \int_0^x \left|\frac{\partial z}{\partial x}\right|_y dx + \int_0^y \left|\frac{\partial z}{\partial y}\right|_{x_0} dy \tag{5.101}$$

Direct integration of (5.100), as suggested in some works [121], [122], is definitely possible. Still, fair results are achievable only for relatively smooth surfaces, i.e., without many small surfaces details. At the same time, the image must contain a flat portion to be used as a reference for background estimation. This limit is due to the fact that, if data contains noise, it may accumulate along the integration direction giving rise to significant artifacts or distortions in the reconstructed surface. To overcome this issue, Harker et al. [125] proposed a new least square procedure for surface reconstruction from gradient field.
Provided the gradient matrix is known, the surface whose gradient is closest in the global least square sense is the one that minimizes the cost function ε defined as follows:

$$\varepsilon(\mathrm{Z}) = \left|\left|\mathrm{ZD_x^T} - \hat{Z}_x\right|\right|_F^2 + \left|\left|D_y Z - \hat{Z}_y\right|\right|_F^2 \tag{5.102}$$

Where Z_x and Z_y are the surface derivatives along x and y directions, respectively, Z is the profile of the surface to be reconstructed, and D_x and D_y are the derivative operators. To find the minimum

of (6), a system of linear equations must be solved. It can be proved that partial derivative of the cost function (6) are equal to zero if the following Sylvester form equation is satisfied:

$$D_y^T D_y Z + Z D_x^T D_x - D_y^T \hat{Z}_y - \hat{Z}_x D_x = 0 \tag{5.103}$$

The significant advantage of Harker's algorithm is the possibility of incorporating surface regularization [126], [127]. Among all the possible techniques, Tichonov's and Dirichlet's methods are of particular interest for the regularization of surface reconstructed from FQSSD images.

According to Tichonov's approach, a generic ill-posed least problem in the form $A\vec{x} = \vec{b}$ is solved by the minimization of the following functional:

$$\varepsilon(x) = \left|\left|A\vec{x} + \vec{b}\right|\right|_2^2 + \lambda^2 \left|\left|L(\vec{x} - \overrightarrow{x_0})\right|\right|_2^2 \tag{5.104}$$

where λ is the regularization strength, alse named minimization weight, L is the regularization operator, and $\overrightarrow{x_0}$ is the a priori estimation of the surface. In general, the optimal value of λ is a function of the surface topography [128] and its independent on the material type. The choice of this value is decided upon the spatial characteristics of the sample and some optimization strategies for its determination may be useful.

Setting the value of $\overrightarrow{x_0}$ to a flat surface, i.e. $\overrightarrow{x_0} = \vec{0}$ the least square problem with Tichonov's regularization is reduced to:

$$\min\left\{\left|\left|A\vec{x} + \vec{b}\right|\right|_2^2 + \lambda^2 \left|\left|L\vec{x}\right|\right|_2^2\right\} \tag{5.105}$$

Harker et al. demonstrated that by differentiating (5.104) one could obtain, for the discrete surface, the following Sylvester equation:

$$\left(D_y^T D_y + \lambda L_y^T L_y\right) Z + Z\left(D_x^T + \lambda L_x^T L_x\right) - D_y^T \hat{Z}_y - \hat{Z}_x D_x = 0 \tag{5.106}$$

where, in our case, we chose $\lambda > 0$ and the identity matrix as the regularization operator (i.e. $L = I$). In this way, the equation is fullydefined and, therefore, directly solvable. Constrained regularization can also be performed when the information on the Z coordinate values along the surface border is known. A surface can be expressed as:

$$Z = P\tilde{Z}Q^T \tag{5.107}$$

Where P and Q are two permutation matrices. The premultiplication of Z by P and the subsequent postmultiplication of the result by Q^T produce the result of adding a frame of zeros around the surface Z, i.e. padding of Z.

$$Z = \begin{bmatrix} 0^T \\ I_{m-2} \\ 0^T \end{bmatrix} \qquad Q = \begin{bmatrix} 0^T \\ I_{n-2} \\ 0^T \end{bmatrix} \tag{5.108}$$

By entering (11) into the (6) one obtains the following equation

$$P^T D_y^T D_y P\tilde{Z} + \tilde{Z} Q^T D_x^T D_x Q - P^T \left(D_y^T \tilde{Z}_y + \hat{Z}_x D_x\right) Q = 0 \tag{5.109}$$

Which is solved to obtain the inner portion Z of the regularized image.
Quantitative validation of the difference for the reconstructed and the measured laser-induced roughness on silicon has been conducted by means of Fourier Analysis. In particular, the power spectral density (PSD) function $W(\vec{k})$ allows to study the amplitudes of surface features as a function of the spatial frequency. It is defined as the square modulus of the Fourier Transform of the surface elevation, and can be expressed as:

$$W(\vec{k}) = \left| \int_0^{2\pi} z(x,y) e^{-i\vec{k}\cdot\vec{r}} dxdy \right|^2 \tag{5.110}$$

When interested in displaying the energy amplitude as a function of only the frequency, regardless of the direction, it is usually more convenient to plot the Radial Power Spectral Density (RPSD) function $\widehat{W}(\vec{k})$. The RPSD is obtained by integrating the PSD over the 2π angle, namely:

$$\widehat{W}(\vec{k}) = \int_0^{2\pi} W(k\cos\phi\,, k\sin\phi) k\, d\phi \tag{5.111}$$

We applied the methods described above to the reconstruction of hardness indentations on AISI 316L stainless steel and laser-treated surfaces of aluminum and silicon samples. The chosen samples have different compositions, thus different BSE emissions, to test the applicability of our method on a variety of sample types, even one with low atomic number such as silicon. Moreover, the hardness indentations and the textured surfaces represent two different surface cases in terms of spatial features, the first with a slowly varying profile and a reference flat area around and the second with patterns a textures with features with high spatial frequency.
In Figure 67-71,we show the reconstruction of Rockwell's and Vickers's indentation on stainless steel, respectively. These features were obtained on polished surfaces and are therefore surrounded by vast flat regions that can be regarded as a height reference. The absence of a regularization strategy leaves artificial marked asymmetries of the indentation prints as can be observed, e.g., in Figure 67 a) and Figure 70 a). This fact underlines the need for regularization in reconstructed images and the choice of optimal strategy depends also on the type of substrates and measurement required.

Indeed, for the regular indentations occurring in the microhardness test presented, a plane background subtraction conserves the shape of the indentation but leaves a polynomial background that might falsify the measurement.
While the Dirichlet's method (Figure 67 c) is very effective if the flat surface of the unindented region is taken as a reference, other methods like Tichonov's, introduced ridges all over the indentation boundaries as shown in Figure 67 d). Thus, for microhardness testing, the Dirichlet's regularization offers the best results and could be potentially used to obtain images for quantitative measurements. In Figure 73-77, we report the reconstructed surface of laser patterned aluminum and silicon surface. Since these surfaces exhibit high roughness, their regularization by background subtraction or Dirichlet's methods are rather ineffective. Indeed, these surface do not have a flat reference region outside the main region of interest, and present high frequency spatial components due to the presence of the roughness. Although Tichonov's regularization can potentially provide better results, its strength must be tuned to obtain optimal performance. We studied the quality of the reconstruction of the silicon sample by comparing the RPSD (5.111) of the different regularized surfaces with the RPSD of the surface calculated on an AFM image, reported in **Figure 80**. Indeed, as shown in plots of Figure 78 and Figure 79 low values of λ e.g. $\lambda = 10^{-3}$ or $\lambda = 10^{-2}$ do not allow for a substantial correction of the surface, and its features are still hidden in the background. Higher λ values proved to be adequate to reveal the surface roughness details. In particular, for $\lambda = 10^{-1}$, we obtain an optimal reconstruction of the surface where small scale features appear more neatly. In this case, Tichonov's method proved to be the best choice with the optimal value of the reconstruction strength as can be seen from the PSD function in very close to the one obtained by the AFM analysis in the middle-frequency region ($0.3\ \mu m^{-1} - 3\ \mu m^{-1}$). Deviations in the higher frequency regions can be ascribed to the SEM lower sensitivity along the Z directions given by the 8-bit image depth. On the other hand, deviations in the lower frequencies region are due to the variability in the different regions scanned with SEM and AFM, and the fact that the scanning region of the AFM is limited by the specs of the instrument to a 70 μm × 70 μm area.

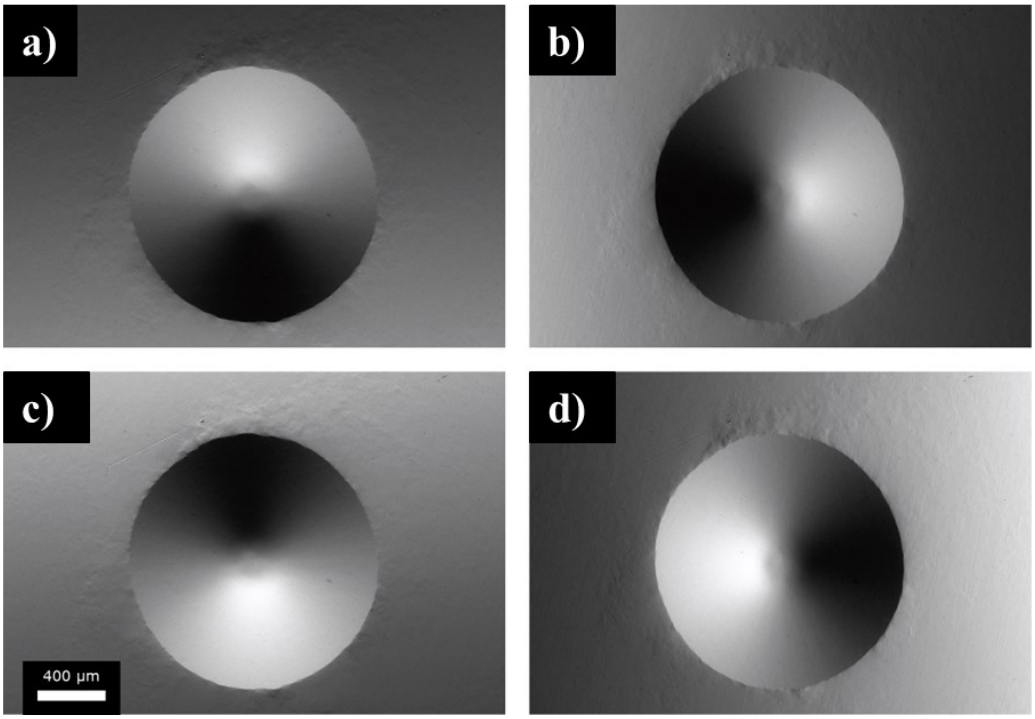

Figure 66: (a-d) Images from single quadrant of FQBSD for the cone indentation sample

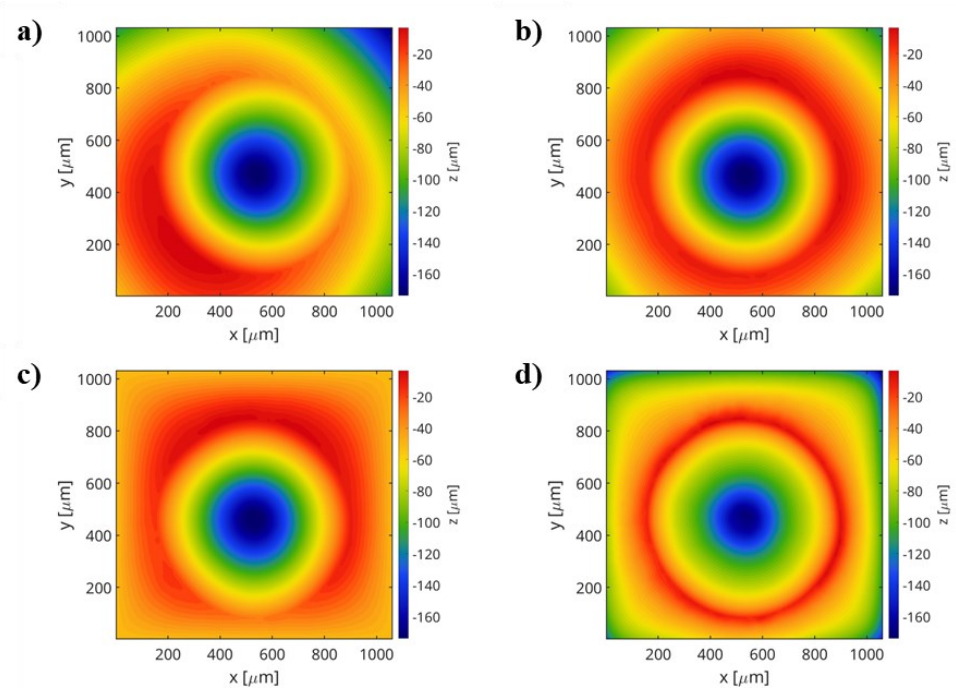

Figure 67: Heatmap of the reconstruction of Rockwell's hardness indentation on AISI 316L stainless steel (see Figure 66) without regularization (A), regularized with plane background subtraction (b), Dirichlet's regularization (c) and Tichonov's regularization (d).

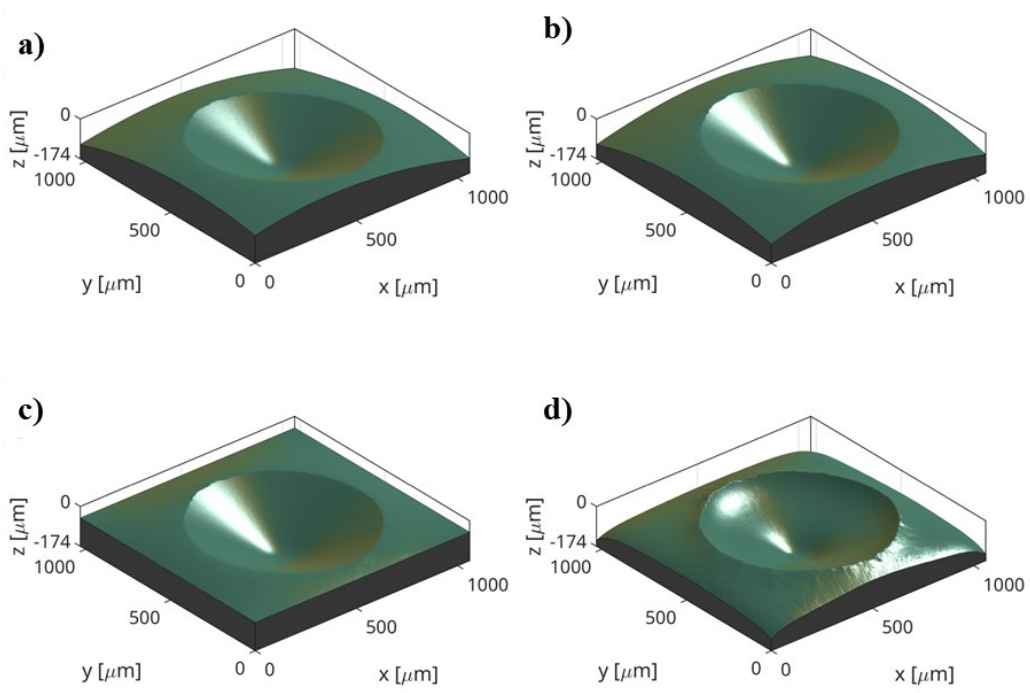

Figure 68: Tridimensional reconstruction of Rockwell's hardness indentation on AISI 316L stainless steel (see Figure 66) without regularization (A), regularized with plane background subtraction (b), Dirichlet's regularization (c) and Tichonov's regularization (d).

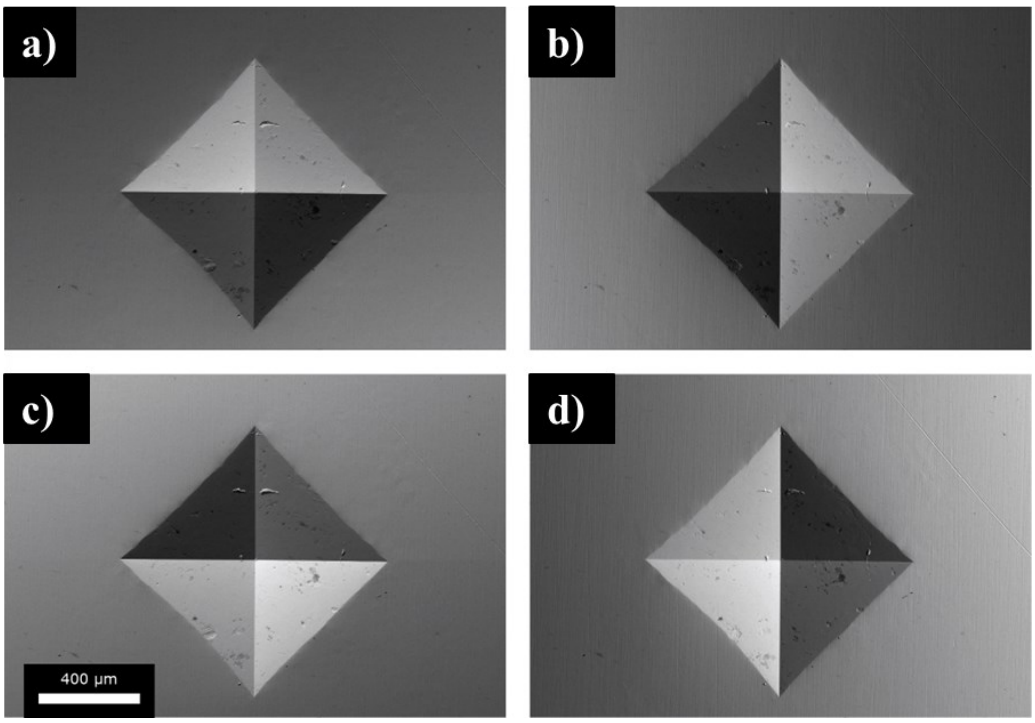

Figure 69: (a-d) Images from single quadrant of FQBSD for the Vicker's indentation sample

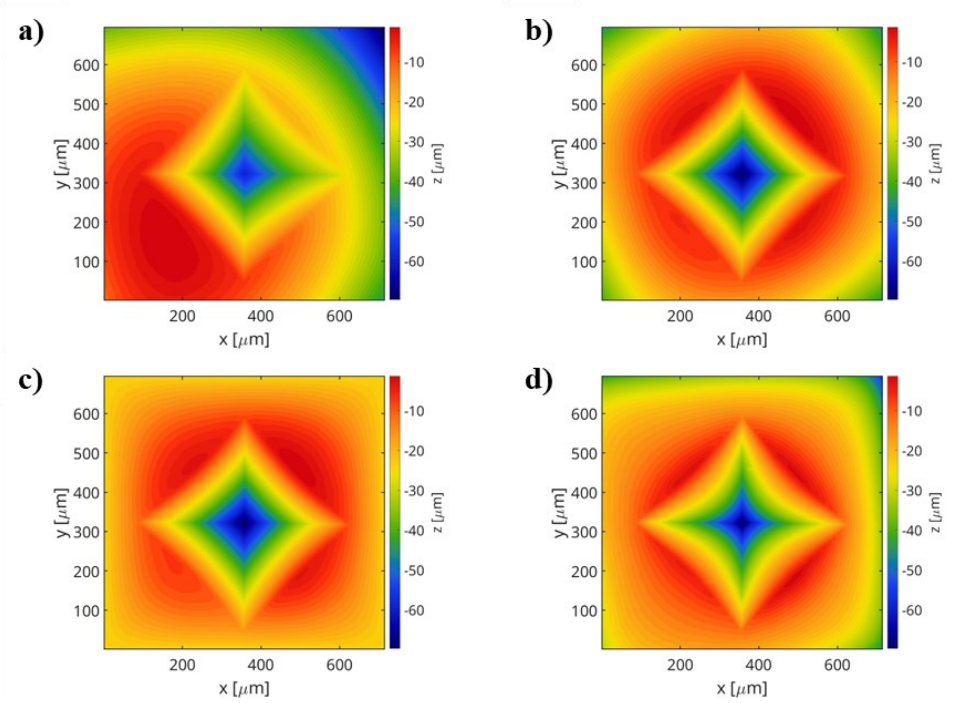

Figure 70: Heatmap of the tridimensional reconstruction of Vicker's hardness indentation on AISI 316L stainless steel (see Figure 69) without regularization a), regularized with plane background b), Dirichlet's regularization c) and Tichonov's regularization d).

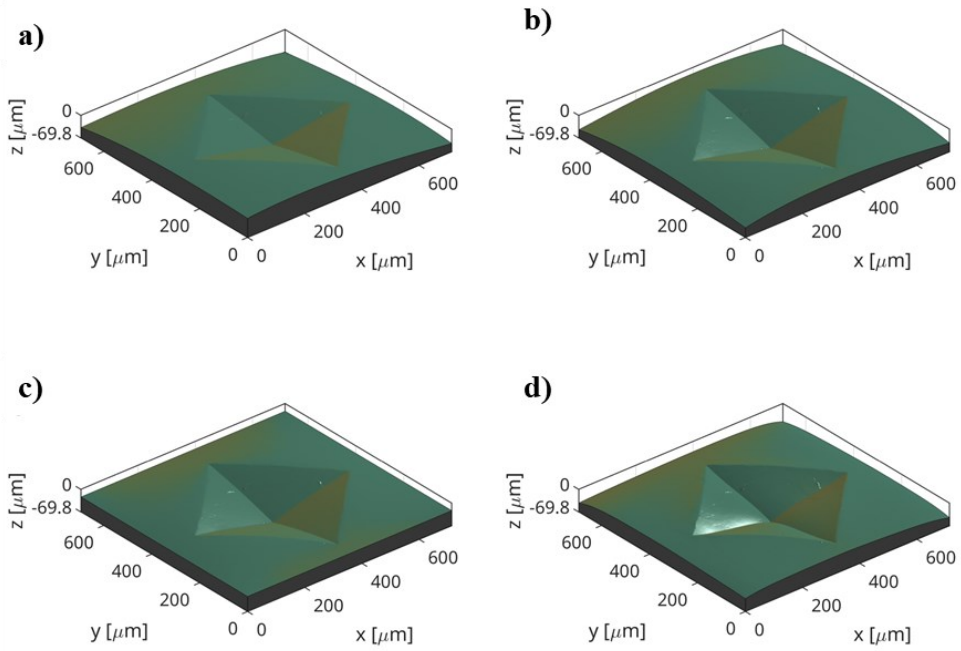

Figure 71: Tridimensional reconstruction of Vicker's hardness indentation on AISI 316L stainless steel (see Figure 69) without regularization a), regularized with plane background subtraction b), Dirichlet's regularization c) and Tichonov's regularization d).

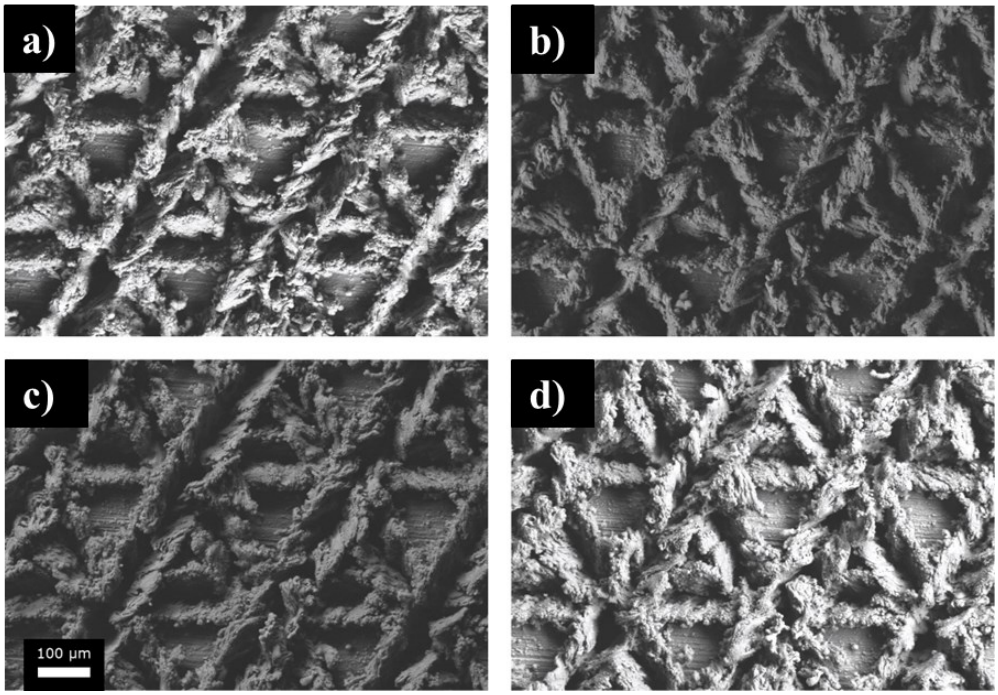

Figure 72: (a-d) Images from single quadrant of FQBSD for the aluminum laser processed samples (triangle texture).

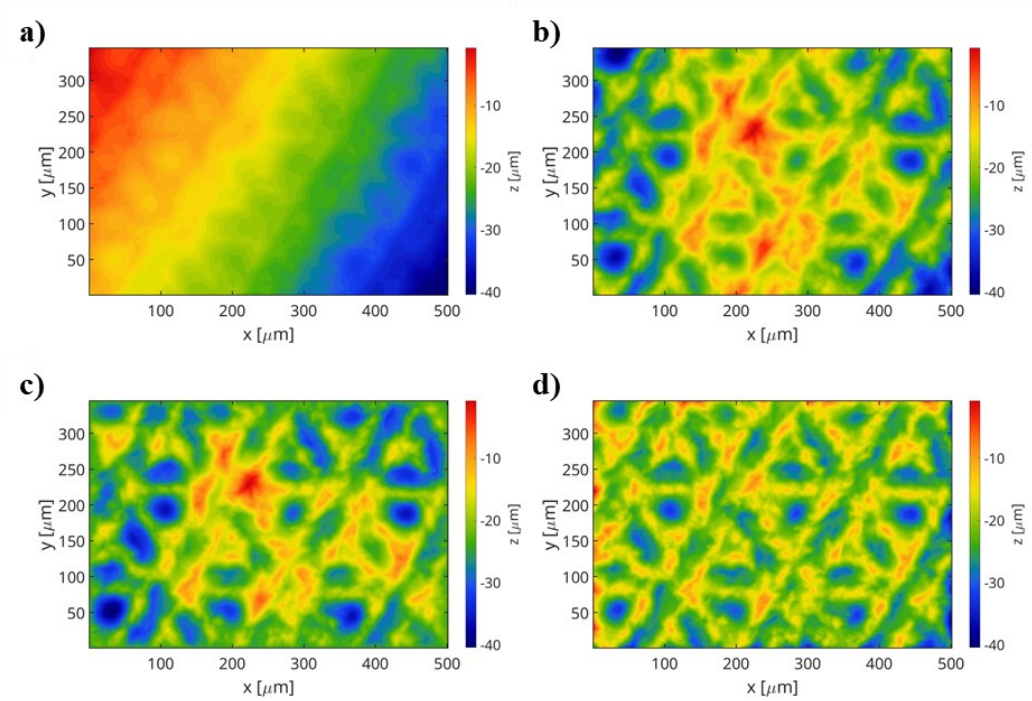

Figure 73: Heatmap of the tridimensional reconstruction of a laser patterned aluminum surface (see Figure 72) without regularization a), regularized with plane background subtraction b) Dirichlet's regularization c) and Tichonov's regularization d).

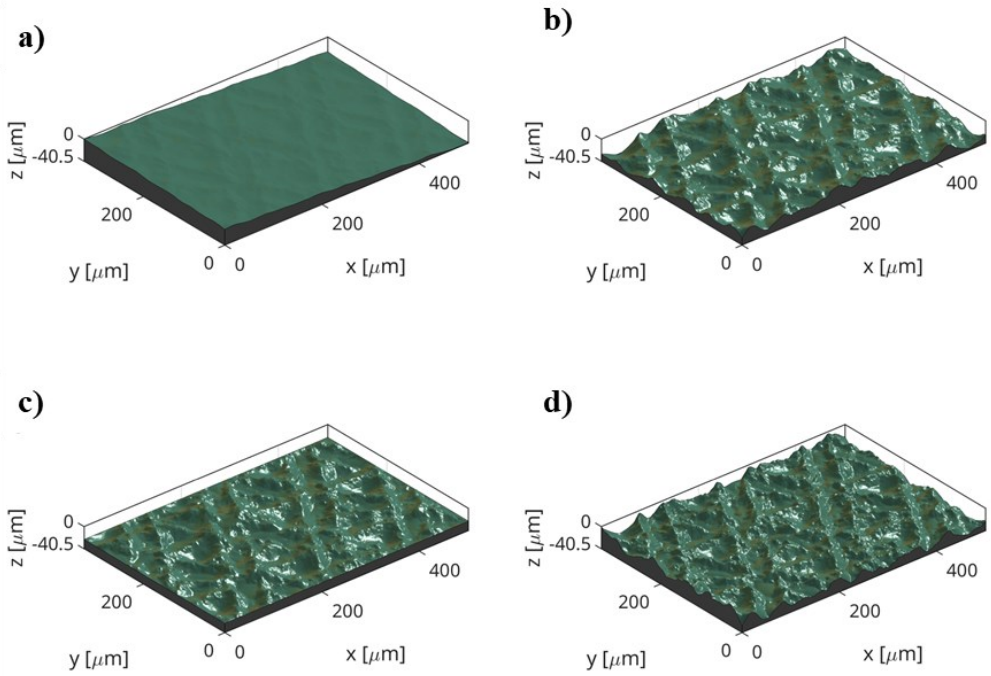

Figure 74: Tridimensional reconstruction of a laser patterned aluminum surface (see Figure 72) without regularization a), regularized with plane background subtraction b) Dirichlet's regularization c) and Tichonov's regularization d).

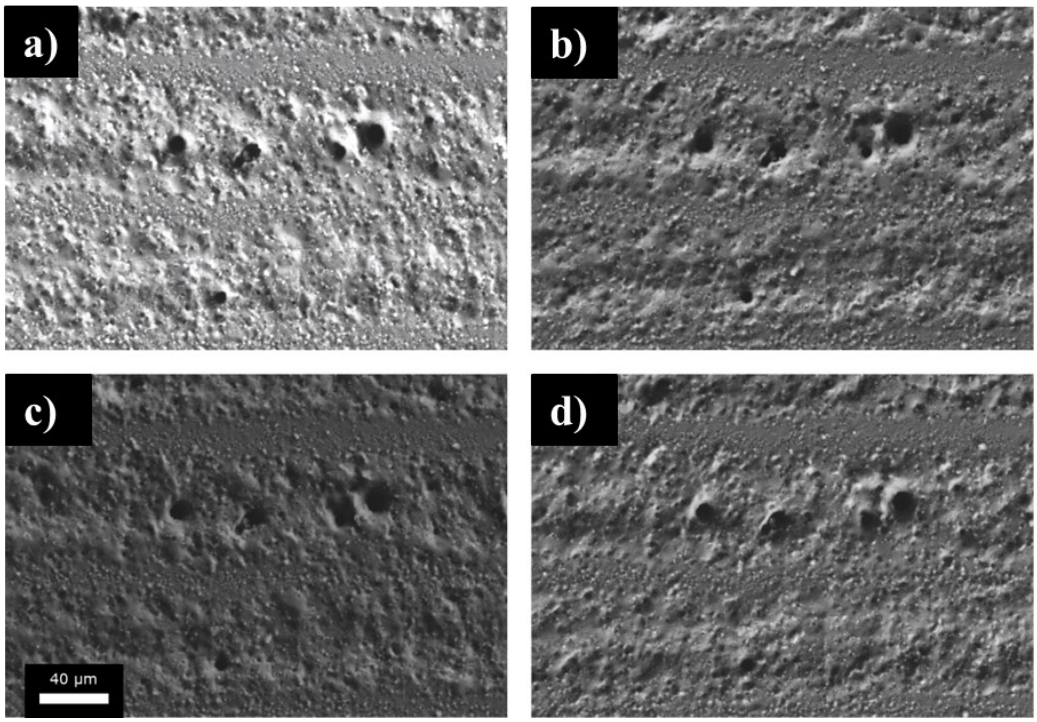

Figure 75: (a-d) Images from single quadrant of FQBSD for the silicon laser textured samples.

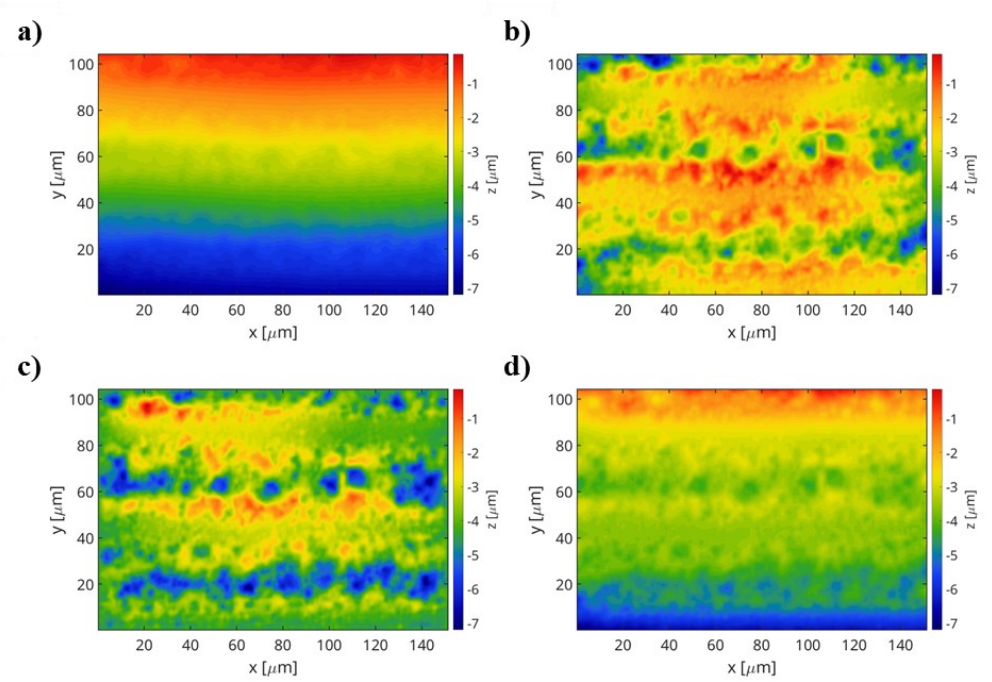

Figure 76: Tridimensional reconstruction of a laser patterned aluminum surface (see Figure 75) without regularization a), regularized with plane background subtraction b), Dirichlet's regularization c) and Tichonov's regularization d).

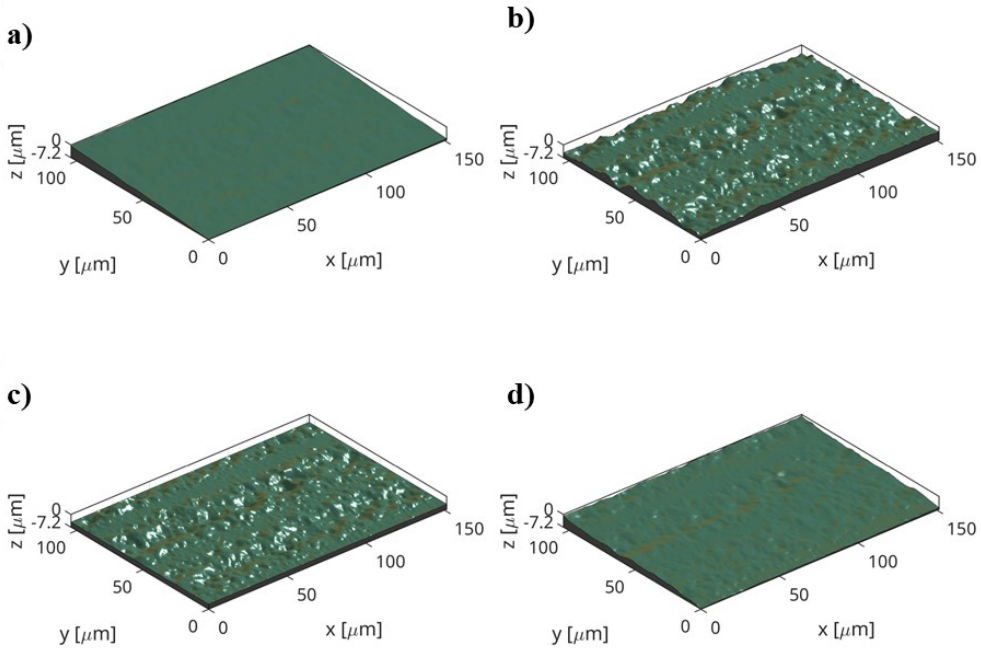

Figure 77: Tridimensional reconstruction of a laser patterned aluminum surface (see Figure 75) without regularization a), regularized with plane background subtraction b), Dirichlet's regularization c) and Tichonov's regularization d).

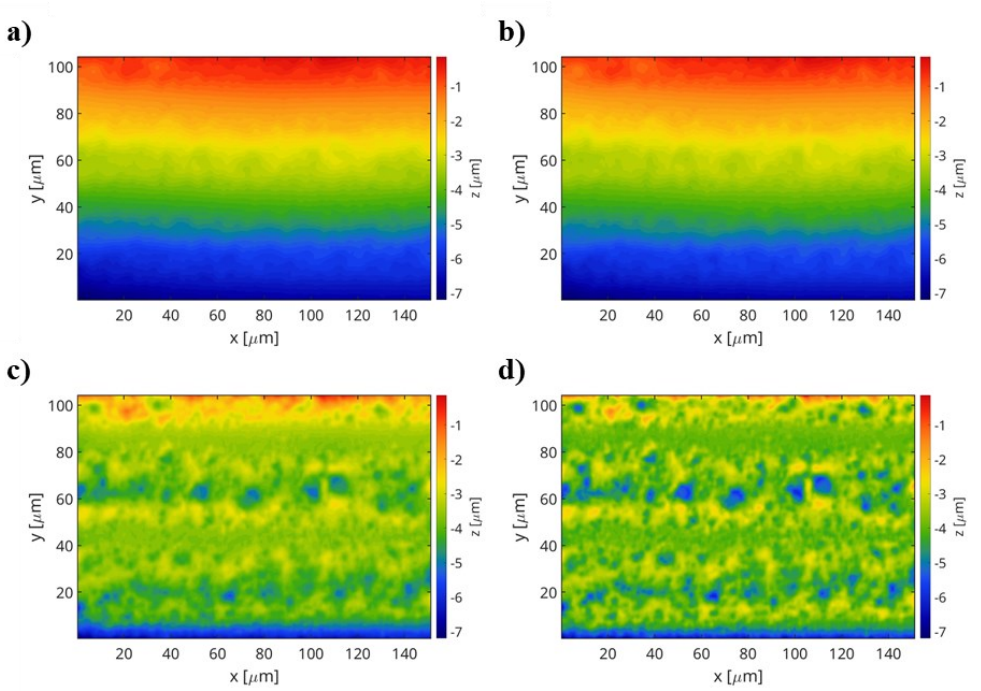

Figure 78: Heatmap of the tridimensional reconstruction of a laser processed silicon surface regularized with Tichonov's techniques with different regularization strength. (a) $\lambda = 1 \cdot 10^{-1}$, (b) $\lambda = 1 \cdot 10^{-2}$, (c) $\lambda = 1 \cdot 10^{-1}$ and (d) $\lambda = 2 \cdot 10^{-1}$.

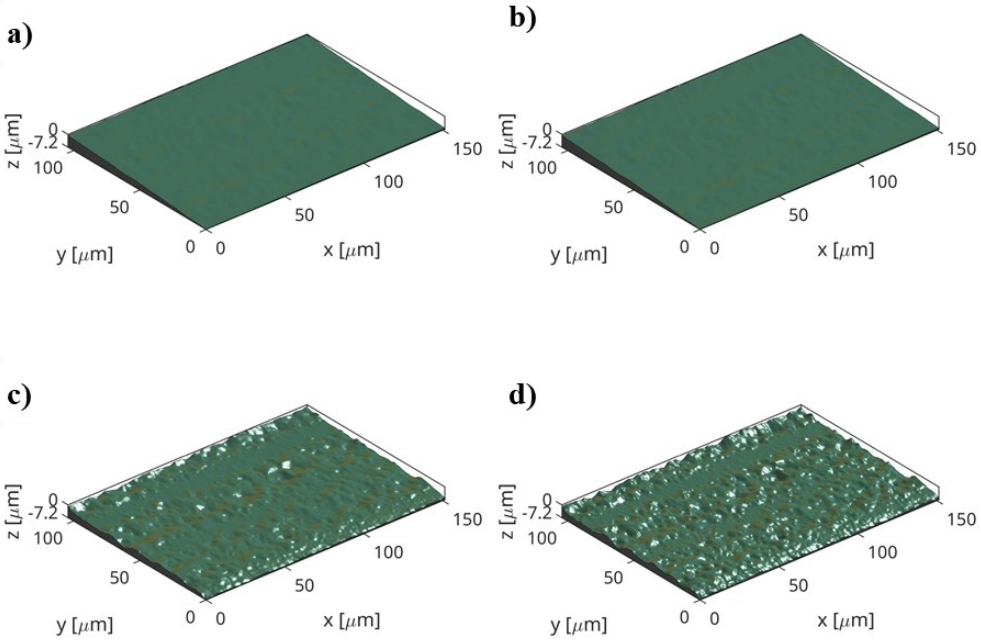

Figure 79: Tridimensional reconstruction of a laser processed silicon surface regularized with Tichonov's techniques with different regularization strength . a) $\lambda = 1 \cdot 10^{-1}$, b) $\lambda = 1 \cdot 10^{-2}$, c) $\lambda = 1 \cdot 10^{-1}$ and d) $\lambda = 2 \cdot 10^{-1}$.

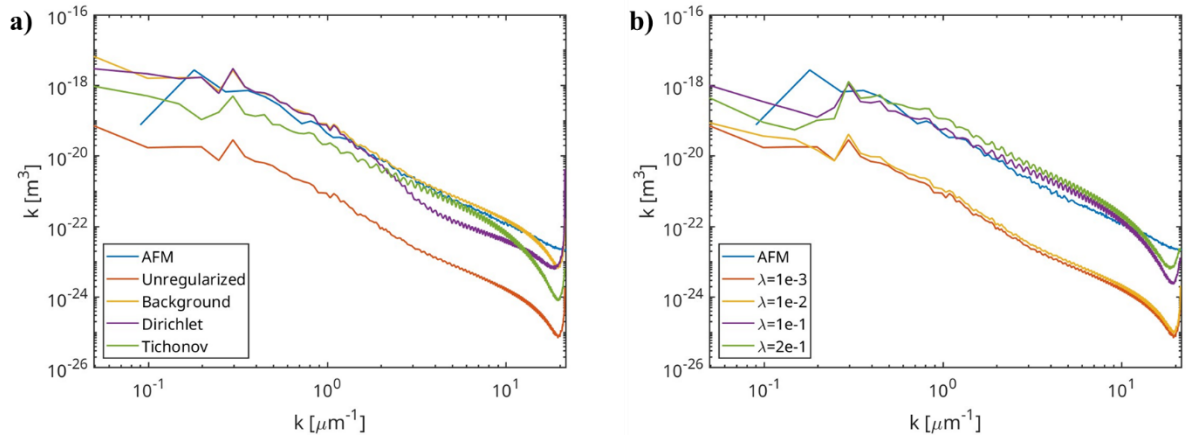

Figure 80: RPSD of the surface reconstructed with different regularization methods a) and reconstructed with Tichonov's method using different regularization strenght b).

5.2 EXTENDED DEPTH OF FIELD IN SCANNING ELECTRON MICROSCOPY

The study of laser machined surfaces is of utmost importance to observe the different phenomena occurring during these treament. However these surfaces usually exhibit a hierarchical structure, revealing details over different size scales. This peculiarity makes theme very difficult to be analyzed with both AFM and profilometers. In this case the use of SEM allow for imaging these surfaces at different levels of detail and obtaning compositional information. In our work [116] we've already showed how tridimensional reconstruction from four quadrant backscattered electron was able to return a good quality replica of laser machined surfaces. However this approach is limited by the relatively low resolution offered by most of the BSE detectors commonly installed on SEM. Moreover, these kinds of samples usually show a high z-elevation, so the depth of field (DoF) offered by the SEM is not enough to characterize the surface in a single image retaining a high resolution. In fact, depending on instruments settings, mainly the aperture size and the working distance, the SEM can achieve DoF, which is usually in the range from some tenths of μm to some mm. If we consider the primary electron beam, its incidence angle on the sample α can be calculated as [129]:

$$\alpha = \operatorname{atan}\left(\frac{D_{ap}}{2W_d}\right) \approx \frac{D_{ap}}{2W_d} \tag{5.112}$$

Where D_{ap} is the diameter of the aperture and W_d is the working distance.
From the beam incidence angle, see Figure 81, the DoF is given as:

$$DoF = \frac{\delta}{\alpha} = \frac{\delta}{\text{atan}\left(\frac{D_{ap}}{2W_d}\right)} \approx \frac{2\delta W_d}{D_{ap}} \tag{5.113}$$

Where δ is the required resolution on the sample as calculated from the calibration bar.

From (5.112) and (5.113) one can easily note that the DoF is increased for high value of working distance and small apertures. Hovewer, sometimes there are situation were small working distances are mandatory. This happens, for instance, when imaging samples at high magnification in a field emission scanning electron microscope (FESEM) with the use InLens detector which requires working distance usually shorter than 4 mm o when using a BSE detector in a topographic contrast mode.

Moreover, to improve the signal-to-noise ratio (SNR) of images from backscattered (BSE) or pseudobackscattered (PBSE) detectors, the use of large apertures is strongly recommended.

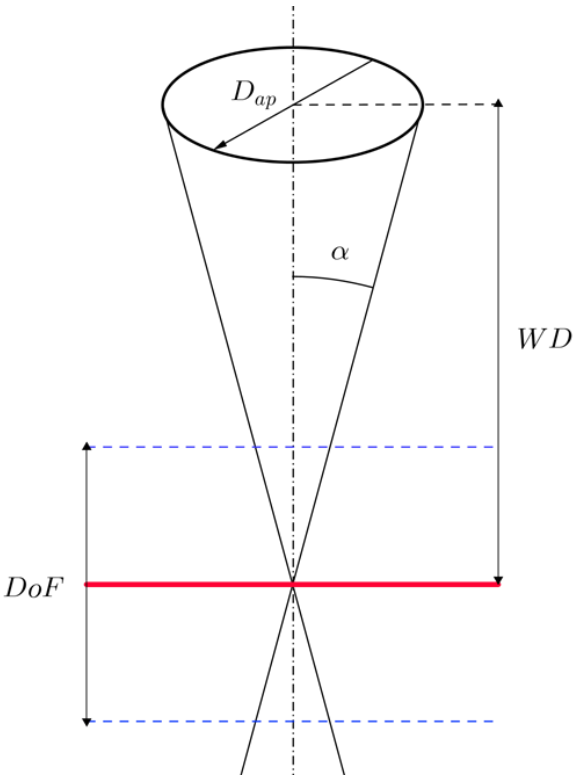

Figure 81: Schematization of the electron optics geometry for the DoF calculation. The red thick line represent the sample.

In all these situation the DoF offered by the SEM is limited and the measurement of samples with high z elevation is not possible with a single image. To overcome this problem an extended depth-of-field (EDoF) approach [130], [131] may be employed.

The reconstruction of the high DoF image can be achieved by either a direct method [132], which makes use of wavelet transform to detect the focused region in each image, or by a model-based

method [133] where the texture and topography are jointly estimated in an iterative process as occurs in optimization problems.
Both methods are based on the collection of a stack of N images with different controlled focus distances that are subsequently merged by a fusion algorithm that will discard all the blurried region in each collected image and merge the in-focus part of the images from the stack. However in some situation we could be interested in reducing as far as possible the DoF to obtain an higher number of images to obtain a tridimensional surface reconstruction with a good resolution on the z-axis.
Following the method discussed in the followings and reported in the flow chart of Figure 82 it is possible to reconstruct an image from Z-stack of SEM images.
The calibration bar containing the SEM metadata from each of the N images is automatically detected and removed. The bar is detected by finding the first line whose pixels are either all black or all white in color. Subsequently, the blurring score BS_i for each collected image M_i is calculated as the variance of Laplacian:

$$BS_i = var[\nabla^2 M_i(x,y)] \tag{5.114}$$

A threshold blurring score BS_{ref} is calculated applying the (5.114) to the $\frac{N}{2}$th image after it has been blurred with a Gaussian filter with kernel size 3 by 3 pixels and standard deviation equal to 0.5. The z-stack is acceptable if the blurring score of the first and last image are lower than BS_{th}, and has to be completed by adding further images otherwise, namely:

$$\begin{cases} BS_0 \leq BS_{ref} \ \wedge BS_N \leq BS_{th} & acceptable \\ BS_0 > BS_{ref} \ \vee BS_N > BS_{th} & not\ acceptable \end{cases} \tag{5.115}$$

The adopted image fusion algorithm is based on the wavelet transform [134]. Wavelet transform is used to divide the image into two components: approximation and details. Approximation is a lower resolution version of the image, whereas details contain the high-frequency components such as edges. This decomposition is obtained by passing the image through high-pass and low-pass filters operating in the horizontal and vertical direction.
For each level, we obtain an approximation (LL), horizontal details (HL), vertical details (LH), and diagonal details (HH):

$$[A(i,x,y), H(i,x,y), V(i,x,y), D(i,x,y)] = DWT(M_i(x,y)] \quad \forall i \tag{5.116}$$

For each point of coordinate (x, y) of the image the most focused areas can be selected and the higher amount of details can be obtained by two different criteria. The first criterion is based on the energy and select the focused image as the one whose details energy is maximized

$$i_f(x,y) = \arg\max_i [H(i,x,y,)^2 + V(i,x,y)^2 + D(i,x,y)^2] \tag{5.117}$$

A second criterion is to choose the focused image as the one which has the highest details coefficient, regardless of the direction, in the point:

$$i_f(x,y) = \arg\max_i\{\max[|H(i,x,y)|, |V(i,x,y)|, |D(i,x,y)|]\} \tag{5.118}$$

The coefficient matrixes of the fused image are calculated as follows:

$$\begin{cases} A_f(x,y) = A\left(\frac{N}{2}\right) \\ H_f(x,y) = H\left[i_f(x,y), x, y\right] \\ V_{f(x,y)} = V\left[i_f(x,y), x, y\right] \\ D_f(x,y) = D\left[i_f(x,y), x, y\right] \end{cases} \tag{5.119}$$

And the image I_m is recostructed as the inverse wavelet transform of the focused components calculated with the (5.119).

$$I_m = IDWT\left(A_f, H_f, V_f, D_f\right) \tag{5.120}$$

Due to noise in the image, it is possible that a local failure of the merging algorithm can lead to spike noise in the reconstructed image. For this reason, the image is finally filtered for noise removal. This filter is easily performed by applying some morphological filter for outlier removal such as median filter, gaussian filter, or Hampfel filter, tuning their kernel size to obtain the desider filtering strength.
To automatize this procedure, a Matlab tool, whose user interface is reported in Figure 83, was realized and used to produce the following reconstructed images.

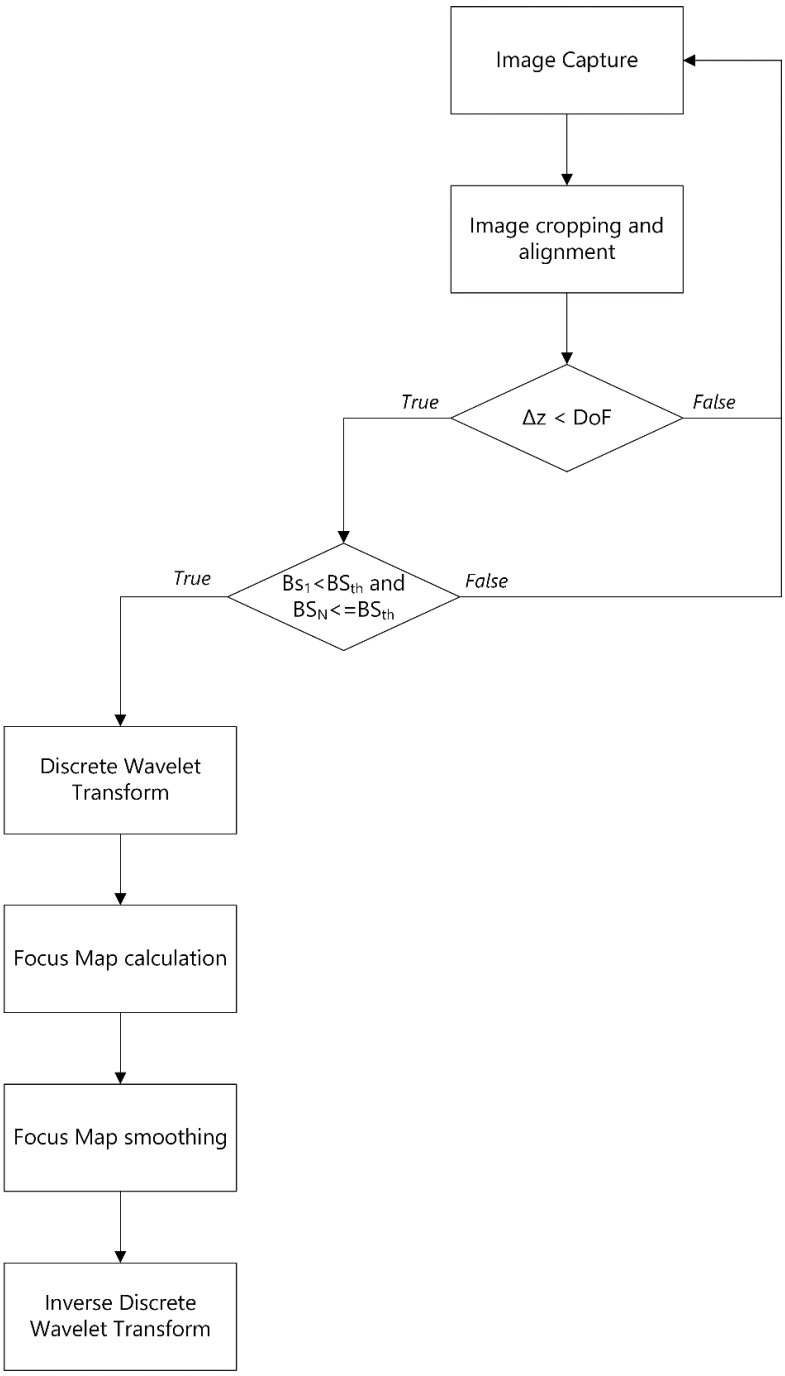

Figure 82: Flowchart of the wavelet-based algorithm for the extended depth of field reconstruction.

The tool was first employed to study the depth of a laser-machined grove on stainless steel, which was impossibile to measure with other instruments. The samples were imaged in a FESEM at a working distance of 5 mm and an aperture size of 60 μm, collecting a Z-stack of 45 pictures, increasing the working distance of 5 μm per step.

Two images from this z-stack are shown in Figure 84, which also shows that it was impossible to get a vision with the whole feature in focus. Meanwhile, Figure 85 shows the extended depth of field images reconstructed by using the sum criterion Figure 85 a) and the maximum criterion Figure 85 b). Both images are good in quality but contain noise, which is more evident when trying to create a tridimensional reconstruction of the surface (Figure 86 a). This noise can be removed by applying a morphological filter, e.g., median or Gaussian blurring filter, as demonstrated in Figure 86 b)-e) .

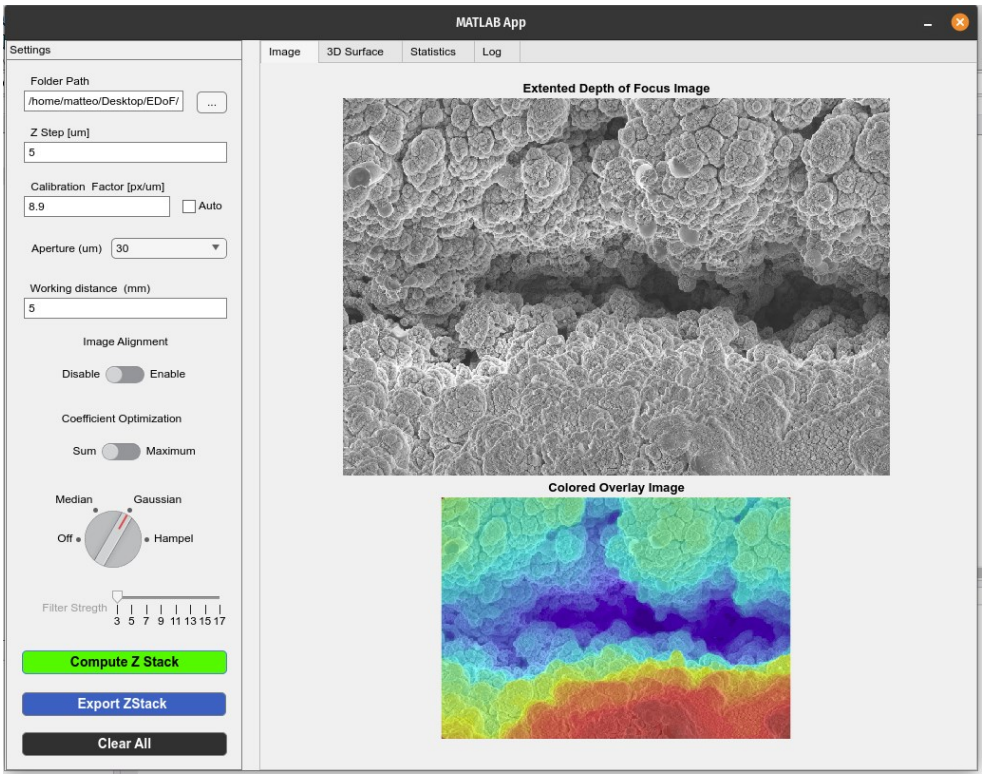

Figure 83: User interface of the Extended Depth of Field tool realized in Matlab.

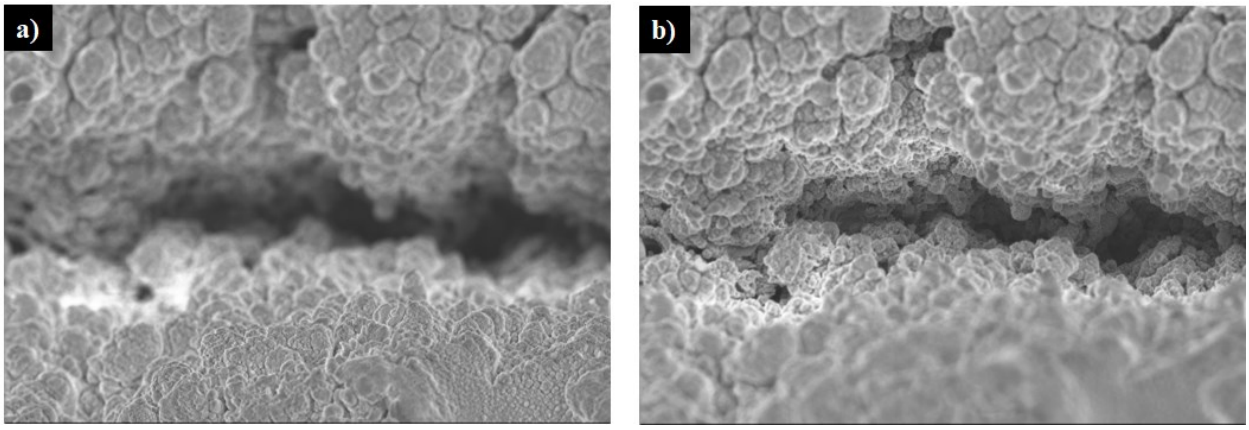

Figure 84: Two images (a and b) from the z-stack of the laser-textured sample. The reader can observe in both the picture that the DoF is much lower than the features height and most of the images appear blurried.

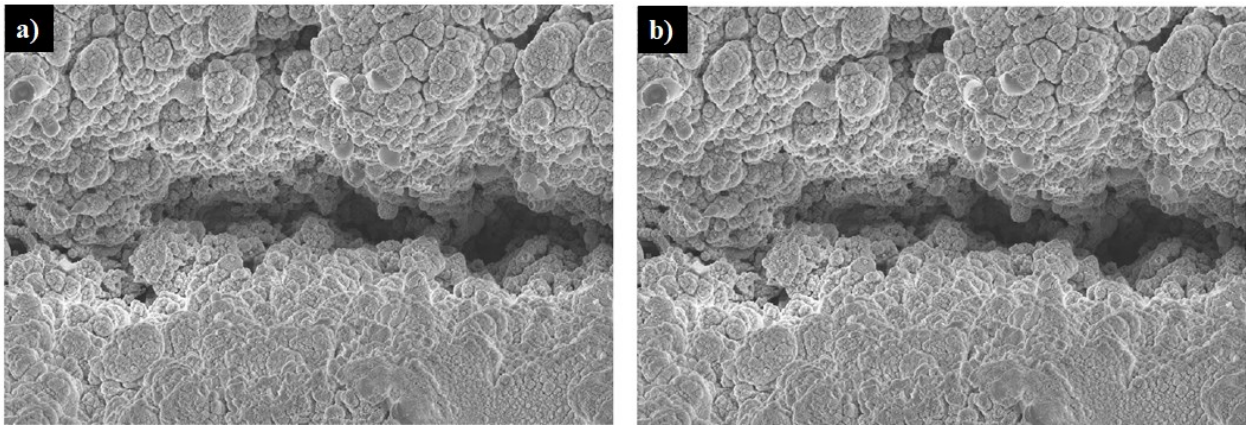

Figure 85: Extended depth of field images reconstructed from z-stack. (a) reconstructed by sum criterion and (b) reconstructed by maximum criterion.

Other two examples of extended depth of field images of laser-processed surfaces are reported in Figure 87 a) and c). Such image stacks have been used to obtained both a tridimensional reconstruction (Figure 88 a) and b) and a height heatmap, shown as overlay on the original images Figure 87 b) and d).

As demonstrated by the results obtained by the application of the algorithm developed, this approach can potentially give almost infinite depth of fields while conserving the lateral resolution which are mainly dependent on the characteristics of the electron microscope and the operating conditions. For both the regularization technique and the extended depth of field approach, we developed tools of great practical utility that can improve the analysis of micro- and nano-textured surfaces in scientific and industrial research.

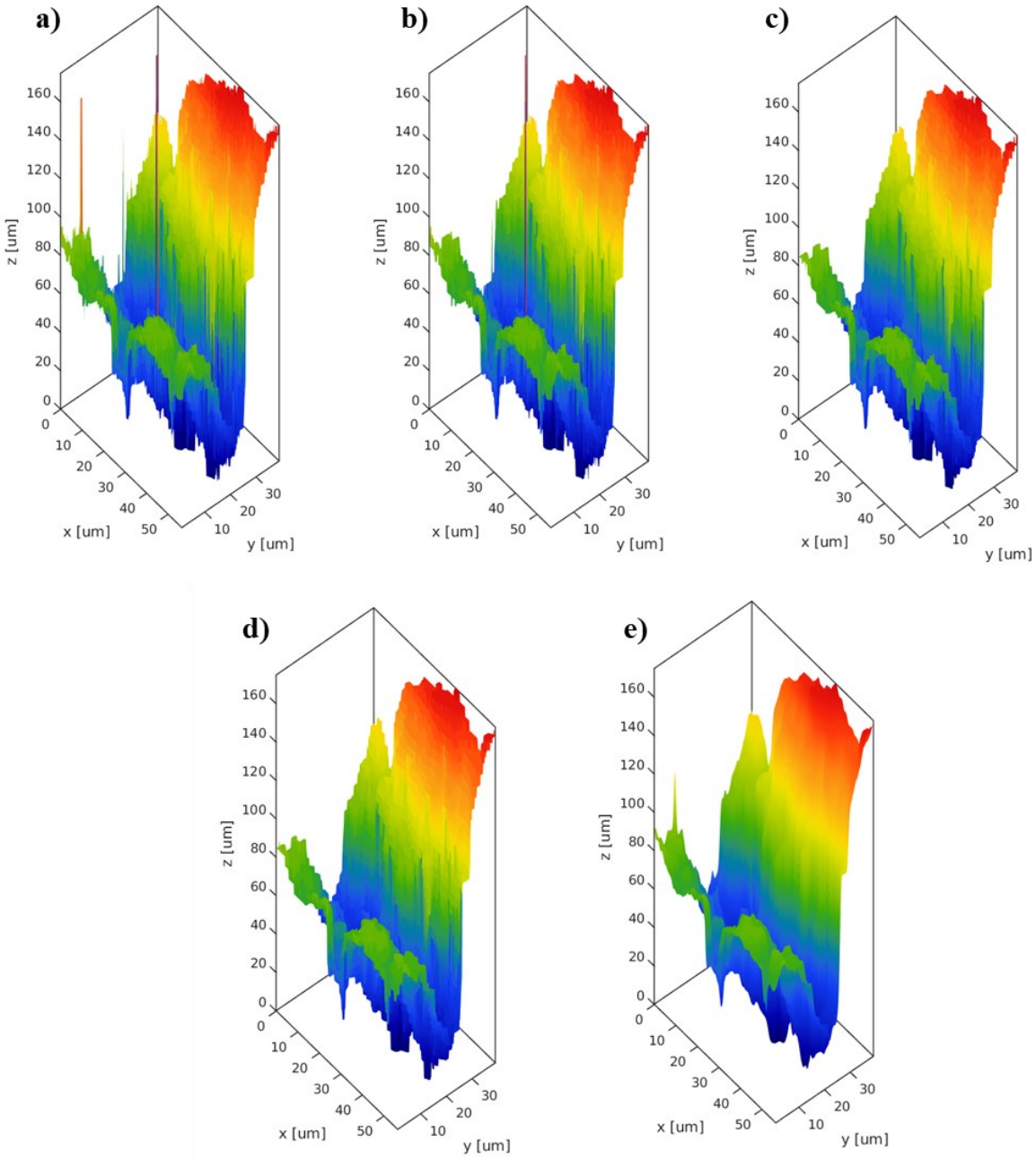

Figure 86: Tridimensional surface reconstruction obtained with the extedend depth of field approach and smoothed with different filtering methods. Unfiltered (a), filter with 3x3 median filter (b), filtered with 5x5 median filter (c), filtered with 7x7 median filter (d) and filtered with 3x3 gaussian filter (e).

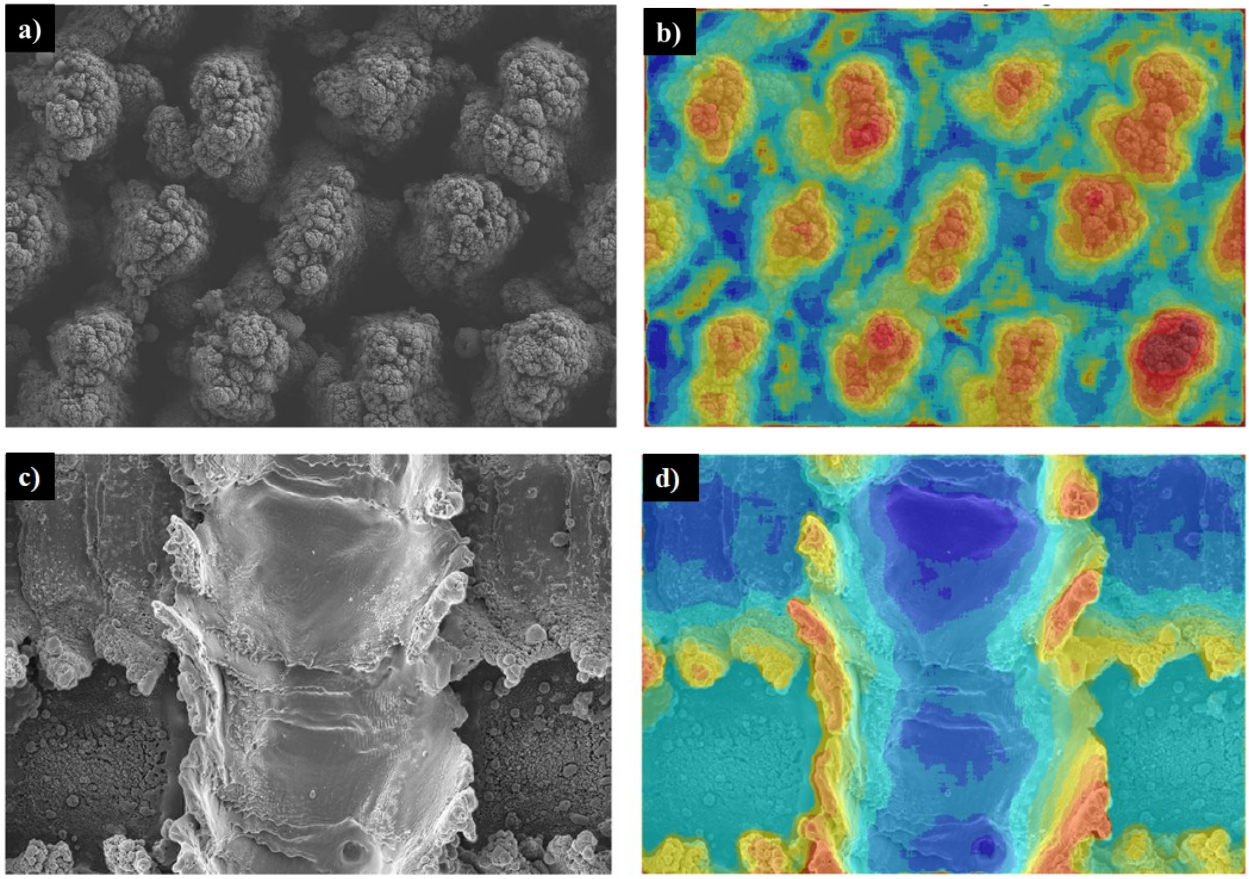

Figure 87: Extedended Depth of field image for two stainless stell laser-processed samples (a and c). Image with an heatmap overlay for the indication of the feature depth (b and b).

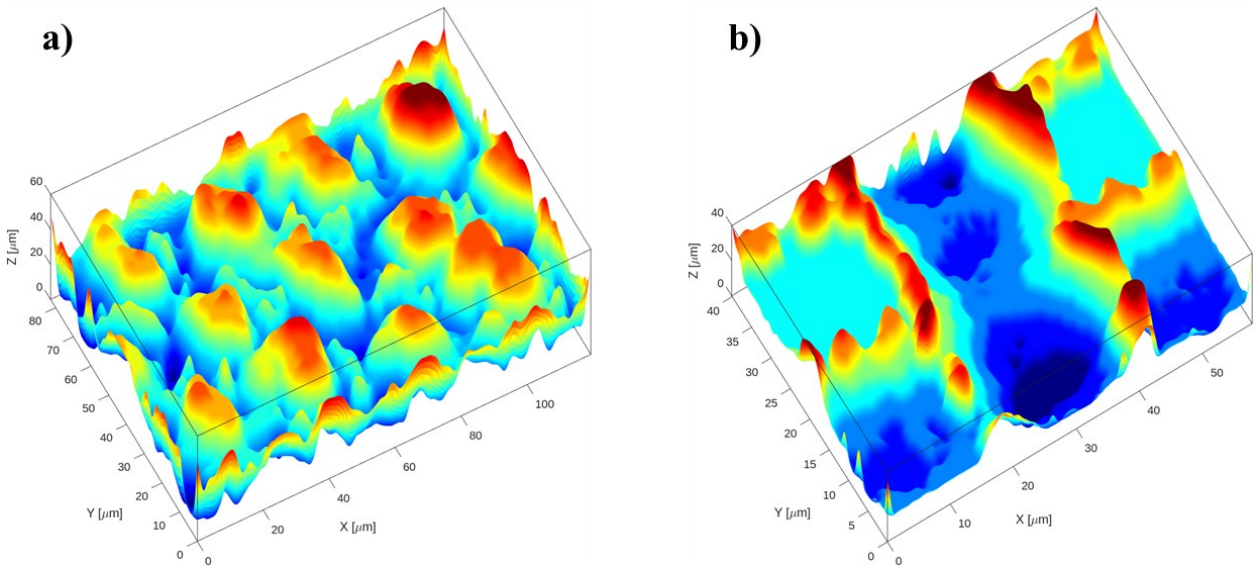

Figure 88: Tridimensional reconstruction of laser processed sample of the samples shown in Figure 87.

Chapter 6
CONCLUSIONS AND FUTURE PERSPECTIVES

The research work undertaken within this thesis allowed for substantial advancement in the SERS substrate preparation techniques for the ultrasensitive detection of different types of contaminants in water. In the following, I will briefly summarize the main results and some paths for possible future developments of the work.

In the first chapter, a novel approach for the simulation-driven design of metal nanoparticle monolayers was developed and successfully tested for detecting skatole in water at an excitation wavelength of 785 nm to reduce fluorescence emission as much as possible. The main goal is to optimize the geometry conditions (particle size and center-to-center distance) targeting a specific Raman band at a given excitation wavelength. The deposition condition to achieve a certain interparticle distance was found by optimizing the seeds' deposition through a Monte Carlo simulation, which takes into account different forces acting on the nanoseeds during the deposition process.
The deposited seeds were grown until they reached the desired particle diameter and, therefore, the optical response that was initially targeted in the simulations. In the model, I assumed that all nanoparticle seeds have the same diameter, even though a more realistic simulation should consider the size distribution and polydispersity of the suspension, which will certainly influence the coverage factor during the deposition.
Despite being tested on gold nanoparticles to detect the skatole, this approach is widely applicable for all the other contaminants and different particle geometry and compositions. Future studies may investigate the possibility of optimizing core-shell particle monolayers to obtain broadband and ultrasensitive SERS substrates.
Although this approach can, in principle, be applied to non-spherical geometry, it appears to be difficult to model more complex nanoparticle morphology, such as nanowires and nanostars.

In the second chapter, I report on an innovative technique for the preparation of nanoparticle arrays by dewetting silver thin films. Thermal and laser-induced dewetting of metal thin-film were already known and well explored by previous studies, but they may cause degradation of the optical response of nanoparticles due to oxidation or tarnishing of the same. I therefore introduced a novel technique based on the exposure of the thin film to high-volatility acid (HCl or HNO_3) or hot water vapors. I also demonstrated by a combined EDX and XPS study that the silver tin film mostly does not react with the vapor, and the obtained nanoparticles show a strong LSPR band.

Only an outer thin layer containing Cl atoms was observed with an XPS analysis, although without producing a significative effect on the optical properties of the nanoparticles. For this reason, these nanoparticles were employed for the detection of Rhodamine 6G as a model molecule (LOD $1.9 \cdot 10^{-11}$ M) and as an etching mask for silicon RIE treatment.
This disruptive procedure for silver nanoparticle synthesis can revolutionize the way we prepare nanoparticles due to its low cost, high reproducibility, and compatibility with almost all the substrates (no thermal or laser treatment is required).
The possibility of dewetting thin films of noble metals, such as gold and platinum, should be investigated to develop a low-cost and fast procedure for producing nanoparticle arrays of these metals.
Further developments should focus on the possibility of producing nanoparticles of semiconductor oxides with relevant applications in photocatalysis, such as Cu_2O and ZnO. Such preparations may involve the exposure of a metal thin film to an oxidant chemical vapor, like, for instance, nitric acid. For a better reproducibility of the synthesis, it appears advisable to recommend the preparation of a sealed cell where an inert transport gas drives the chemical vapor at a controlled flow rate.

The last approach introduced in this thesis is based on the thin-film deposition on a previously nanostructured surface. The surface was nanostructured by a RIE etching treatment using some copper nanoparticles created by laser-induced dewetting as an etching mask. The obtained pillars were coated with a gold-thin film and used for the detection of polystyrene nanoparticles of 100 nm diameter. Using a digital analysis method, we achieved a record limit of detection of about 0.8 ng mL^{-1}, which is almost three orders of magnitude better than the latest work in the field at the moment of writing.
These findings are very promising in the study of such widespread contaminants as, up to now, the detection of such low concentrations has only been allowed by the use of FESEMs, which, however, does not allow identification of polymers. The investigated devices are, therefore, good candidates for routine detection and quantification of nanoplastics. Further work should be done to study, identify, and quantify other polymers' nanoplastics present in water pollution.
Finally, the substrate could be further improved by employing a simulation-driven procedure to lower the limit of detection further and set the path to a novel standard characterization procedure for micro- and nano-plastics.

APPENDIX A - TECHNOLOGY TRANSFER ACTIVITIES

During my Ph.D. course, I have been involved in several technology transfer activities for patenting some of the technological solutions that were developed as a part of my research.
In particular one Italian patent application has been filed and submitted with the title Metal-based filtering membrane for environmental analytical application (membrana filtrante rivestita con metallo plasmonicamente attivo per applicazioni analitiche ambientali).
This patent application describes a nanostructured and metal-coated membrane and the production process thereof, for analytical applications, including SERS.

A.1 DRY ETCHNG OF TRACK ETCHED MEMBRANES

The production of a track-etch (TE) filtering membrane is a process which consists of a first irradiation with heavy ions of the polymeric film and a subsequent etching in a concentrated NaOH solution. The irradiation which is obtained with fragments from the fission of heavy nuclei (Ca or U), or more commonly with an ion beam generated in an accelerator, creates some localized damage in the membrane [135].
When exposed to chemical etchant, the damaged zones show a much higher etching rate than the rest of the membrane so nanopores of controlled size are created through the membrane thickness [136].
Different polymers have been used historically for the preparation of TE membranes but due to the need for high hydrophilicity for filtration of aqueous medium the production nowadays focuses on the use of polycarbonate (PC) or polyethylene terephthalate (PET), with the latter usually preferred for its higher hydrophilicity and its high mechanical strenght[136].
Junkat et al. [137] studied the effect of oxygen plasma treatment on the surface roughness and chemical composition of a PET sample. They observed the oxygen concentration move from 20.8% to around 30% after a few seconds of treatment as a consequence of the formation of O-rich surface groups and the contact angle was lowered from the initial 72° to around 19°.
They also observed a strong increase of surface roughness, with the formation of pillar-like structures. The same type of structures was also obtained in other works [138], [139] and is due to the differential etching rate of amorphous and crystalline zones within the semicrystalline polymer. In fact, it was stated by Fernandez-Blázquez et al. [138] that differences in etch rates related to crystallinity are due to more easy chain scission that occurs in amorphous polymers. However, some phenomena related to glass transition due to polymer heating may also concur with this phenomenon.

A.2 FABRICATION PROCESS

The main idea of the production process is to create pillar-like nanostructures on the surface of the track-etch membranes by means of RIE treatment without using any mask (maskless etching). The absence of the mask deposition and patterning steps will speed up production and also lower the end-product cost.

We therefore exploited the etching behaviour of PET surface previously described for the realization of pillar-like nanostructures on the top of the filtering membrane.

Said nanostructures will be coated with a metal thin-film, generally gold or silver, which, as already discussed in the previous chapters, show a plasmonic resonance located in the visible range and are therefore suitable for SERS application.

The effect of the degree of crystallinity of a polymer on the etching rate in an O_2 plasma has been widely described in the literature. In particular, a differential etching effect has been observed, where the amorphous regions of the polymer tend to be rapidly removed by the O_2 plasma, while the crystalline regions exhibit higher resistance.

The percentage of crystallinity in semi-crystalline polymers, such as polyethylene terephthalate (PET) and polycarbonate (PC), can be altered through treatment with an electron beam (e-beam) or gamma rays. These treatments aim to reduce the degree of crystallinity of the polymer and decrease the average size of crystallites.

The process parameters (beam energy, radiation intensity, and exposure dose) are chosen based on the polymer used and its initial crystalline structure.

The O_2 RIE treatment allows for the creation of nanostructures on the surface of the membrane. These nanostructures form as a result of the differential attack of the polymer by the oxygen plasma, which attacks the amorphous regions more rapidly than the crystalline ones.

In order to obtain pillars of appropriate height it is of utmost importance to give the plasma a strong chemical action. For this purpose the treatment was conducted for 60 seconds at a power of 200W, a pressure of 20 Pa and an oxygen flow of 50 sccm.

The second step is devoted to the deoposition of of layer of metal with a thickness ranging from 30 nm to 50 nm by means of RF sputtering. Power and deposition time can be chosen according to the desired thickness, however, to obtain good conformity it is recommended to operate a presurre around 3 Pa.

The final step goal is to deposit a protective oxide layer (e.g., silicon dioxide) optionally exhibiting photocatalytic behavior (anatase phase of titanium dioxide), with a thickness of around 1 nm, on the surface of the membrane already coated with a metallic layer. In the case of TiO_2 deposition, to push towards the formation of the anatase phase, the treatment can be performed using a process atmosphere of 90% Ar and 10% O_2 at a pressure around 3 Pa. This indication arises from the study by Horprathum et al. [140] who investigated the effect of oxygen partial pressure on the obtained crystalline phase of TiO_2 thin-film deposited by sputtering.

In Figure 1a) I show an SEM micrograph of the PET-TE membrane as provided by the supplier. The same membrane is shown in Figure 89b) after the O_2 RIE treatment and in Figure 89c) after

the deposition of the Ag/TiO_2 thin film. One can observed from Figure 89c) that pillar-like nanostructures are produced as a combination of the nanostructuring/coating process.

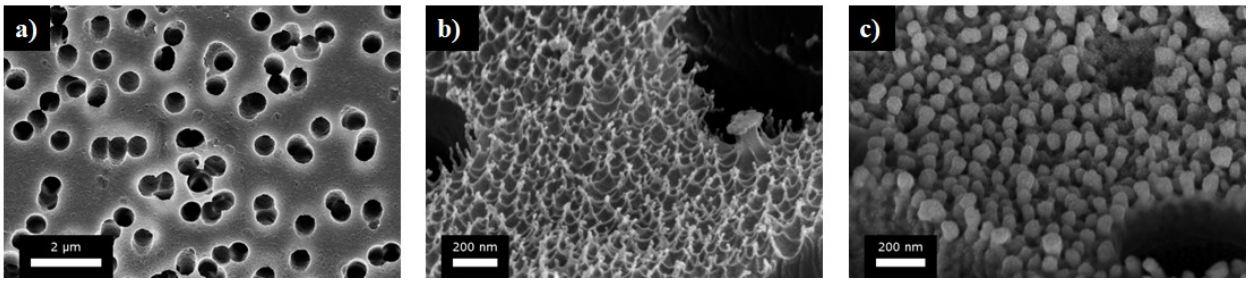

Figure 89: PETE track-etched membrane as provided (a), after O_2 treatment (b) and after the Ag thin-film deposition (c).

A.3 SERS MEASUREMENTS

In Figure 90 a) it is shown the UV-VIS spectra of a PET-TE membrane as provided (red line) and after the nanostructuration and Ag/TiO_2 thin film deposition (blue line) acquired in a diffuse reflectance (incidence at 0°) with a Shimadzu UV-VIS 2600 equipped with a ISR-2600Plus integration sphere.

The comparison of the two spectra makes evident how the nanostructure membrane exhibits a strong LSPR peak localized at around 390 nm.

The membrane has been tested for the detection of Rhodamine 6G (R6G) through surface-enhanced Raman spectroscopy. We utilized an excitation wavelength of 532 nm and a power of 300 µW. A small droplet of 10 µL was deposited on the membrane which was dried under a N_2 flow.

As a benchmark. the same measurement has been performed on PET-TE membrane coated with a 40 nm gold layer which is very similar to the product currently available on the market. Figure 90 d) the obtained Raman spectra are reported and we observe how the intensity of the R6G raman band due to the aromatic ring breathing at 611 cm^{-1} as an intensity of about 4500 counts on the nanostructured Ag/TiO_2 coated membraned whereas is only about 700 counts on the standard gold-coated membranes.

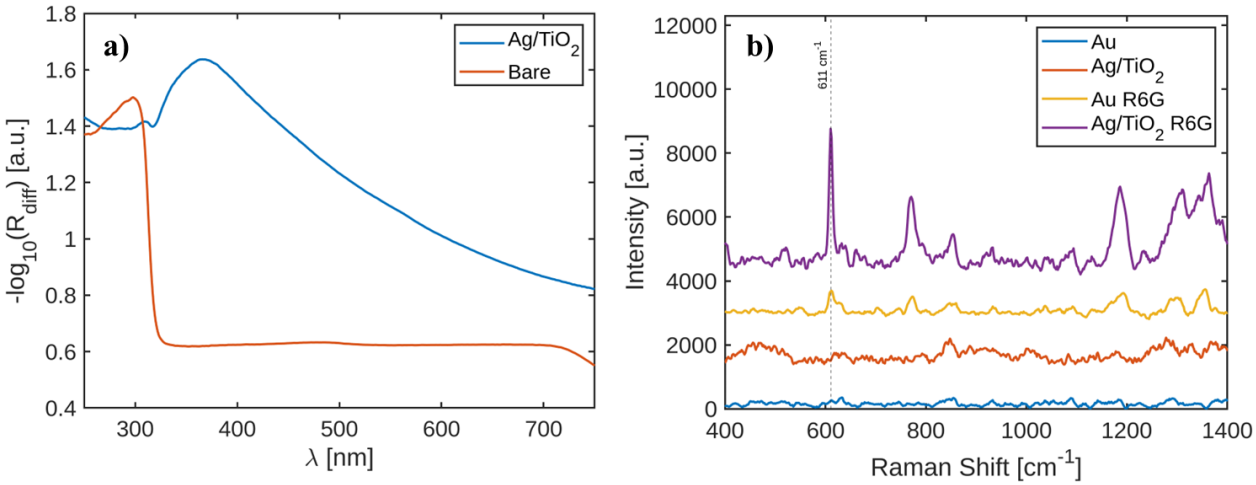

Figure 90: a) UV-VIS reflection spectra of the bare and coated membranes. b) Raman spectra of a Rhodamine6G 1µM solution obtained with standard gold-coated membrane and with the nanostructured membrane.

REFERENCES

[1] A. H. Guerrero, H. J. Fasoli, and J. L. Costa, "Why Gold and Copper Are Colored but Silver Is Not," *J. Chem. Educ.*, vol. 76, no. 2, p. 200, Feb. 1999, doi: 10.1021/ed076p200.

[2] P. Atkins and J. de Paula, *Atkins' Physical Chemistry*. OUP Oxford, 2010.

[3] P. F. Wang *et al.*, "Regulated color-changing metallic glasses," *Journal of Alloys and Compounds*, vol. 876, p. 160139, Sep. 2021, doi: 10.1016/j.jallcom.2021.160139.

[4] W. Blades, A. Reber, S. Khanna, L. López Sosa, P. Calaminici, and A. Koster, "Evolution of the Spin Magnetic Moments and Atomic Valence of Vanadium in VCux(+), VAgx(+), and VAux(+) Clusters (x = 3 - 14)," *The journal of physical chemistry. A*, vol. 121, Mar. 2017, doi: 10.1021/acs.jpca.7b01030.

[5] C. A. Balanis, *Advanced Engineering Electromagnetics*. John Wiley & Sons, 2012.

[6] L. Yongqian, *Plasmonic Optics: Theory and Applications*. SPIE Press, 2017.

[7] P. B. Johnson and R. W. Christy, "Optical Constants of the Noble Metals," *Phys. Rev. B*, vol. 6, no. 12, pp. 4370–4379, Dec. 1972, doi: 10.1103/PhysRevB.6.4370.

[8] S. A. Maier, *Plasmonics: Fundamentals and Applications*. Springer Science & Business Media, 2007.

[9] M. Pelton and G. W. Bryant, *Introduction to Metal-Nanoparticle Plasmonics*. John Wiley & Sons, 2013.

[10] I. D. Mayergoyz, *Plasmon Resonances in Nanoparticles*. World Scientific, 2013.

[11] C. F. Bohren and D. R. Huffman, *Absorption and Scattering of Light by Small Particles*. John Wiley & Sons, 2008.

[12] G. Mie, "Beiträge zur Optik trüber Medien, speziell kolloidaler Metallösungen," *Annalen der Physik*, vol. 330, no. 3, pp. 377–445, 1908, doi: 10.1002/andp.19083300302.

[13] J. D. Jackson, *Elettrodinamica classica*. Zanichelli, 2001.

[14] G. B. Arfken, *Mathematical Methods for Physicists*. Academic Press, 2013.

[15] E. W. Weisstein, "Vector Spherical Harmonic." Accessed: Aug. 21, 2023. [Online]. Available: https://mathworld.wolfram.com/

[16] B. J. Sumlin, W. R. Heinson, and R. K. Chakrabarty, "Retrieving the aerosol complex refractive index using PyMieScatt: A Mie computational package with visualization capabilities," *Journal of Quantitative Spectroscopy and Radiative Transfer*, vol. 205, pp. 127–134, Jan. 2018, doi: 10.1016/j.jqsrt.2017.10.012.

[17] E. Smith and G. Dent, *Modern Raman Spectroscopy: A Practical Approach*. John Wiley & Sons, 2019.

[18] C. V. Raman and K. S. Krishnan, "A New Type of Secondary Radiation," *Nature*, vol. 121, no. 3048, Art. no. 3048, Mar. 1928, doi: 10.1038/121501c0.

[19] D. Porezag and M. R. Pederson, "Infrared intensities and Raman-scattering activities within density-functional theory," *Phys Rev B Condens Matter*, vol. 54, no. 11, pp. 7830–7836, Sep. 1996, doi: 10.1103/physrevb.54.7830.

[20] A. Müller and N. Mohan, "Raman intensities, depolarization ratios, and polarizability derivatives: Matrix notation, relation to other molecular constants and simple isotopic rules," *The Journal of Chemical Physics*, vol. 67, no. 5, pp. 1918–1925, Aug. 2008, doi: 10.1063/1.435123.

[21] M. Tsuboi, J. M. Benevides, and G. J. Thomas, "Raman Tensors and their application in structural studies of biological systems," *Proc Jpn Acad Ser B Phys Biol Sci*, vol. 85, no. 3, pp. 83–97, Mar. 2009, doi: 10.2183/pjab/85.83.

[22] M. Fleischmann, P. J. Hendra, and A. J. McQuillan, “Raman spectra of pyridine adsorbed at a silver electrode,” *Chemical Physics Letters*, vol. 26, no. 2, pp. 163–166, May 1974, doi: 10.1016/0009-2614(74)85388-1.
[23] D. L. Jeanmaire and R. P. Van Duyne, “Surface raman spectroelectrochemistry: Part I. Heterocyclic, aromatic, and aliphatic amines adsorbed on the anodized silver electrode,” *Journal of Electroanalytical Chemistry and Interfacial Electrochemistry*, vol. 84, no. 1, pp. 1–20, Nov. 1977, doi: 10.1016/S0022-0728(77)80224-6.
[24] M. G. Albrecht and J. A. Creighton, “Anomalously intense Raman spectra of pyridine at a silver electrode,” *J. Am. Chem. Soc.*, vol. 99, no. 15, pp. 5215–5217, Jun. 1977, doi: 10.1021/ja00457a071.
[25] E. C. Le Ru and P. G. Etchegoin, “Rigorous justification of the |E|4 enhancement factor in Surface Enhanced Raman Spectroscopy,” *Chemical Physics Letters*, vol. 423, no. 1, pp. 63–66, May 2006, doi: 10.1016/j.cplett.2006.03.042.
[26] M. Giardino, I. Mannelli, R. Yu, F. J. G. de Abajo, V. Pruneri, and D. Janner, “Synthesis of tailored nanostructured gold surfaces for SERS applications by controlled seed deposition and growth,” *Applied Surface Science*, vol. 649, p. 159076, Mar. 2024, doi: 10.1016/j.apsusc.2023.159076.
[27] D. Aureau, Y. Varin, K. Roodenko, O. Seitz, O. Pluchery, and Y. J. Chabal, “Controlled Deposition of Gold Nanoparticles on Well-Defined Organic Monolayer Grafted on Silicon Surfaces,” *J. Phys. Chem. C*, vol. 114, no. 33, pp. 14180–14186, Aug. 2010, doi: 10.1021/jp104183m.
[28] M. Fan and A. G. Brolo, “Silver nanoparticles self assembly as SERS substrates with near single molecule detection limit,” *Phys. Chem. Chem. Phys.*, vol. 11, no. 34, pp. 7381–7389, Aug. 2009, doi: 10.1039/B904744A.
[29] B. Andreiuk *et al.*, “Design and synthesis of gold nanostars-based SERS nanotags for bioimaging applications,” *Nanotheranostics*, vol. 6, no. 1, pp. 10–30, Jan. 2022, doi: 10.7150/ntno.61244.
[30] N. G. Bastús, J. Comenge, and V. Puntes, “Kinetically Controlled Seeded Growth Synthesis of Citrate-Stabilized Gold Nanoparticles of up to 200 nm: Size Focusing versus Ostwald Ripening,” *Langmuir*, vol. 27, no. 17, pp. 11098–11105, Sep. 2011, doi: 10.1021/la201938u.
[31] Z. Liu, W. Hou, P. Pavaskar, M. Aykol, and S. B. Cronin, “Plasmon resonant enhancement of photocatalytic water splitting under visible illumination,” *Nano Lett.*, vol. 11, no. 3, pp. 1111–1116, Mar. 2011, doi: 10.1021/nl104005n.
[32] N. I. Evcimen, S. Coskun, D. Kozanoglu, G. Ertas, H. E. Unalan, and E. N. Esenturk, “Growth of branched gold nanoparticles on solid surfaces and their use as surface-enhanced Raman scattering substrates,” *RSC Adv.*, vol. 5, no. 123, pp. 101656–101663, Nov. 2015, doi: 10.1039/C5RA18570J.
[33] J. G. Hinman, A. J. Stork, J. A. Varnell, A. A. Gewirth, and C. J. Murphy, “Seed mediated growth of gold nanorods: towards nanorod matryoshkas,” *Faraday Discuss.*, vol. 191, no. 0, pp. 9–33, Oct. 2016, doi: 10.1039/C6FD00145A.
[34] W. Yang, L. W. Yap, S. Gong, and W. Cheng, “Hairy gold nanorods: gold nanowire growth on nanosubstrates [Invited],” *Opt. Mater. Express, OME*, vol. 10, no. 2, pp. 342–357, Feb. 2020, doi: 10.1364/OME.10.000342.
[35] D. M. Solís, J. M. Taboada, F. Obelleiro, L. M. Liz-Marzán, and F. J. García de Abajo, “Optimization of Nanoparticle-Based SERS Substrates through Large-Scale Realistic

Simulations," *ACS Photonics*, vol. 4, no. 2, pp. 329–337, Feb. 2017, doi: 10.1021/acsphotonics.6b00786.
[36] V. Joseph, A. Matschulat, J. Polte, S. Rolf, F. Emmerling, and J. Kneipp, "SERS enhancement of gold nanospheres of defined size," *Journal of Raman Spectroscopy*, vol. 42, no. 9, pp. 1736–1742, 2011, doi: 10.1002/jrs.2939.
[37] S. Hong and X. Li, "Optimal size of gold nanoparticles for surface-enhanced raman spectroscopy under different conditions," *J. Nanomaterials*, vol. 2013, p. 49:49, Gennaio 2013, doi: 10.1155/2013/790323.
[38] N. J. Ray *et al.*, "Enhanced Tunability of Gold Nanoparticle Size, Spacing, and Shape for Large-Scale Plasmonic Arrays," *ACS Appl. Nano Mater.*, vol. 2, no. 7, pp. 4395–4401, Jul. 2019, doi: 10.1021/acsanm.9b00815.
[39] F. J. García de Abajo and A. Howie, "Retarded field calculation of electron energy loss in inhomogeneous dielectrics," *Phys. Rev. B*, vol. 65, no. 11, p. 115418, Mar. 2002, doi: 10.1103/PhysRevB.65.115418.
[40] "Silane Coupling Agents," Gelest. Accessed: Jan. 03, 2024. [Online]. Available: https://technical.gelest.com/brochures/silane-coupling-agent/silane-coupling-agents/
[41] J. Sukham, O. Takayama, A. V. Lavrinenko, and R. Malureanu, "High-Quality Ultrathin Gold Layers with an APTMS Adhesion for Optimal Performance of Surface Plasmon Polariton-Based Devices," *ACS Appl. Mater. Interfaces*, vol. 9, no. 29, pp. 25049–25056, Jul. 2017, doi: 10.1021/acsami.7b07181.
[42] A. U. Alam, M. Howlader, and M. J. Deen, "Oxygen Plasma and Humidity Dependent Surface Analysis of Silicon, Silicon Dioxide and Glass for Direct Wafer Bonding," *ECS Journal of Solid State Science and Technology*, vol. 2, pp. P515–P523, Oct. 2013, doi: 10.1149/2.007312jss.
[43] Y. Huan, S. J. Park, K. C. Gupta, S.-Y. Park, and I.-K. Kang, "Slide cover glass immobilized liquid crystal microdroplets for sensitive detection of an IgG antigen," *RSC Adv.*, vol. 7, no. 60, pp. 37675–37688, Jul. 2017, doi: 10.1039/C7RA06386E.
[44] W. Haiss, N. T. K. Thanh, J. Aveyard, and D. G. Fernig, "Determination of Size and Concentration of Gold Nanoparticles from UV−Vis Spectra," *Anal. Chem.*, vol. 79, no. 11, pp. 4215–4221, Jun. 2007, doi: 10.1021/ac0702084.
[45] J. Eklöf, T. Gschneidtner, S. Lara-Avila, K. Nygård, and K. Moth-Poulsen, "Controlling deposition of nanoparticles by tuning surface charge of SiO2 by surface modifications," *RSC Adv.*, vol. 6, no. 106, pp. 104246–104253, Nov. 2016, doi: 10.1039/C6RA22412A.
[46] Z. Adamczyk, M. Zembala, B. Siwek, and P. Warszyński, "Structure and ordering in localized adsorption of particles," *Journal of Colloid and Interface Science*, vol. 140, no. 1, pp. 123–137, Nov. 1990, doi: 10.1016/0021-9797(90)90329-M.
[47] Z. Adamczyk, B. Siwek, M. Zembala, and P. Belouschek, "Kinetics of localized adsorption of colloid particles," *Advances in Colloid and Interface Science*, vol. 48, pp. 151–280, Apr. 1994, doi: 10.1016/0001-8686(94)80008-1.
[48] J. N. Israelachvili, *Intermolecular and Surface Forces*. Academic Press, 2015.
[49] B. P. Cahill, G. Papastavrou, G. J. M. Koper, and M. Borkovec, "Adsorption of Poly(amido amine) (PAMAM) Dendrimers on Silica: Importance of Electrostatic Three-Body Attraction," *Langmuir*, vol. 24, no. 2, pp. 465–473, Jan. 2008, doi: 10.1021/la7021352.
[50] K. C. Grabar *et al.*, "Kinetic Control of Interparticle Spacing in Au Colloid-Based Surfaces: Rational Nanometer-Scale Architecture," *J. Am. Chem. Soc.*, vol. 118, no. 5, pp. 1148–1153, Jan. 1996, doi: 10.1021/ja952233+.

[51] M. Semmler, J. Rička, and M. Borkovec, “Diffusional deposition of colloidal particles: electrostatic interaction and size polydispersity effects,” *Colloids and Surfaces A: Physicochemical and Engineering Aspects*, vol. 165, no. 1, pp. 79–93, May 2000, doi: 10.1016/S0927-7757(99)00438-0.
[52] H. Ohshima, “Surface Charge Density/Surface Potential Relationship for a Spherical Colloidal Particle in a Solution of General Electrolytes,” *Journal of Colloid and Interface Science*, vol. 171, no. 2, pp. 525–527, May 1995, doi: 10.1006/jcis.1995.1214.
[53] R. J. Hunter, *Zeta Potential in Colloid Science: Principles and Applications*. Academic Press, 2013.
[54] C. H. Li and C. K. Lee, “Minimum cross entropy thresholding,” *Pattern Recognition*, vol. 26, no. 4, pp. 617–625, Apr. 1993, doi: 10.1016/0031-3203(93)90115-D.
[55] C. H. Li and P. K. S. Tam, “An iterative algorithm for minimum cross entropy thresholding,” *Pattern Recognition Letters*, vol. 19, no. 8, pp. 771–776, Jun. 1998, doi: 10.1016/S0167-8655(98)00057-9.
[56] L. Chen *et al.*, “Plasmonic-induced SERS enhancement of shell-dependent Ag@Cu2O core–shell nanoparticles,” *RSC Adv.*, vol. 7, no. 27, pp. 16553–16560, Mar. 2017, doi: 10.1039/C7RA01187C.
[57] M. A. Tahir *et al.*, “Klarite as a label-free SERS-based assay: a promising approach for atmospheric bioaerosol detection,” *Analyst*, vol. 145, no. 1, pp. 277–285, Dec. 2019, doi: 10.1039/C9AN01715A.
[58] R. B. Chevalier and J. R. Dwyer, “Optimizing noncontact oxygen-plasma treatment to improve the performance of a top-down nanofabricated surface enhanced Raman spectroscopy substrate with structurally responsive, high-aspect-ratio nanopillar array,” *Journal of Raman Spectroscopy*, vol. 52, no. 3, pp. 608–615, 2021, doi: 10.1002/jrs.6050.
[59] A. Matikainen, T. Nuutinen, P. Vahimaa, and S. Honkanen, “A solution to the fabrication and tarnishing problems of surface-enhanced Raman spectroscopy (SERS) fiber probes,” *Sci Rep*, vol. 5, no. 1, Art. no. 1, Feb. 2015, doi: 10.1038/srep08320.
[60] J.-H. Ham, J. S. Park, M.-K. Oh, and J. H. Kim, “Reusable Wrinkled Nanoporous Silver Film Fabricated by Plasma Treatment for Surface-Enhanced Raman Scattering Applications,” *ACS Omega*, vol. 8, no. 49, pp. 47146–47152, Dec. 2023, doi: 10.1021/acsomega.3c07167.
[61] D. Gentili, G. Foschi, F. Valle, M. Cavallini, and F. Biscarini, “Applications of dewetting in micro and nanotechnology,” *Chem. Soc. Rev.*, vol. 41, no. 12, pp. 4430–4443, May 2012, doi: 10.1039/C2CS35040H.
[62] D. Wang and P. Schaaf, “Solid-state dewetting for fabrication of metallic nanoparticles and influences of nanostructured substrates and dealloying,” *physica status solidi (a)*, vol. 210, no. 8, pp. 1544–1551, 2013, doi: 10.1002/pssa.201200895.
[63] P. G. Jamkhande, N. W. Ghule, A. H. Bamer, and M. G. Kalaskar, “Metal nanoparticles synthesis: An overview on methods of preparation, advantages and disadvantages, and applications,” *Journal of Drug Delivery Science and Technology*, vol. 53, p. 101174, Oct. 2019, doi: 10.1016/j.jddst.2019.101174.
[64] V. Amendola, S. Polizzi, and M. Meneghetti, “Laser Ablation Synthesis of Gold Nanoparticles in Organic Solvents,” *J. Phys. Chem. B*, vol. 110, no. 14, Art. no. 14, Apr. 2006, doi: 10.1021/jp0605092.

[65] S. N. Bonvicini, B. Fu, A. J. Fulton, Z. Jia, and Y. Shi, “Formation of Au, Pt, and bimetallic Au–Pt nanostructures from thermal dewetting of single-layer or bilayer thin films,” *Nanotechnology*, vol. 33, no. 23, Art. no. 23, Mar. 2022, doi: 10.1088/1361-6528/ac5a83.
[66] L. Q. Ly, A. J. Fulton, S. N. Bonvicini, and Y. Shi, “Pulsed laser-induced dewetting and thermal dewetting of Ag thin films for the fabrication of Ag nanoparticles,” *Nanotechnology*, vol. 32, no. 33, Art. no. 33, May 2021, doi: 10.1088/1361-6528/abfee7.
[67] C. V. Thompson, “Solid-State Dewetting of Thin Films,” *Annu. Rev. Mater. Res.*, vol. 42, no. 1, pp. 399–434, Aug. 2012, doi: 10.1146/annurev-matsci-070511-155048.
[68] O. Tsui, B. Du, F. Xie, Z. Yang, and Y. J. Wang, “Distinguishing Spinodal and Nucleation Phase Separation in Dewetting Polymer Films,” *Nano Science and Technology: Novel Structures and Phenomena*, Mar. 2003, doi: 10.1201/9780203390283.ch19.
[69] J. Bischof, D. Scherer, S. Herminghaus, and P. Leiderer, “Dewetting Modes of Thin Metallic Films: Nucleation of Holes and Spinodal Dewetting,” *Physical review letters*, vol. 77, pp. 1536–1539, Sep. 1996, doi: 10.1103/PhysRevLett.77.1536.
[70] J. W. Cahn, “Phase Separation by Spinodal Decomposition in Isotropic Systems,” *The Journal of Chemical Physics*, vol. 42, no. 1, pp. 93–99, Jul. 2004, doi: 10.1063/1.1695731.
[71] P. Jacquet *et al.*, “Grain growth: The key to understand solid-state dewetting of silver thin films,” *Scripta Materialia*, vol. 115, pp. 128–132, Apr. 2016, doi: 10.1016/j.scriptamat.2016.01.005.
[72] A. Sharma and R. Khanna, “Pattern Formation in Unstable Thin Liquid Films,” *Phys. Rev. Lett.*, vol. 81, no. 16, pp. 3463–3466, Oct. 1998, doi: 10.1103/PhysRevLett.81.3463.
[73] E. Owusu-Ansah, V. I. Birss, and Y. Shi, “Mechanisms of Pulsed Laser-Induced Dewetting of Thin Platinum Films on Tantalum Substrates—A Quantitative Study,” *J. Phys. Chem. C*, vol. 124, no. 42, Art. no. 42, Oct. 2020, doi: 10.1021/acs.jpcc.0c06264.
[74] K. Jacobs, S. Herminghaus, and K. R. Mecke, “Thin Liquid Polymer Films Rupture via Defects,” *Langmuir*, vol. 14, no. 4, pp. 965–969, Feb. 1998, doi: 10.1021/la970954b.
[75] U. Thiele, M. Mertig, and W. Pompe, “Dewetting of an Evaporating Thin Liquid Film: Heterogeneous Nucleation and Surface Instability,” *Phys. Rev. Lett.*, vol. 80, no. 13, pp. 2869–2872, Mar. 1998, doi: 10.1103/PhysRevLett.80.2869.
[76] C.-Y. Cho, J.-C. Chang, M.-X. Cai, P.-T. Lin, and Y.-J. Yang, “Dewetting Process of Silver Thin Films and Its Application on Percolative Pressure Sensors with High Sensitivity,” *Polymers*, vol. 15, no. 1, Art. no. 1, Jan. 2023, doi: 10.3390/polym15010180.
[77] J. Rombaut, S. Martínez, U. M. Matera, P. Mazumder, and V. Pruneri, “Antireflective Multilayer Surface with Self-Cleaning Subwavelength Structures,” *ACS Photonics*, vol. 8, no. 3, pp. 894–900, Mar. 2021, doi: 10.1021/acsphotonics.0c01909.
[78] A. B. Tesler, B. M. Maoz, Y. Feldman, A. Vaskevich, and I. Rubinstein, “Solid-State Thermal Dewetting of Just-Percolated Gold Films Evaporated on Glass: Development of the Morphology and Optical Properties,” *J. Phys. Chem. C*, vol. 117, no. 21, pp. 11337–11346, May 2013, doi: 10.1021/jp400895z.
[79] S. Yadavali, M. Khenner, and R. Kalyanaraman, “Pulsed laser dewetting of Au films: Experiments and modeling of nanoscale behavior,” *Journal of Materials Research*, vol. 28, no. 13, Art. no. 13, Jul. 2013, doi: 10.1557/jmr.2013.90.
[80] J. Trice, D. Thomas, C. Favazza, R. Sureshkumar, and R. Kalyanaraman, “Pulsed-laser-induced dewetting in nanoscopic metal films: Theory and experiments,” *Phys. Rev. B*, vol. 75, no. 23, Art. no. 23, Jun. 2007, doi: 10.1103/PhysRevB.75.235439.

[81] S. V. Makarov *et al.*, "Controllable femtosecond laser-induced dewetting for plasmonic applications," *Laser & Photonics Reviews*, vol. 10, no. 1, Art. no. 1, 2016, doi: 10.1002/lpor.201500119.
[82] K. Kumar and P. Swaminathan, "Role of silver nanoparticles in the dewetting behavior of copper thin films," *Thin Solid Films*, vol. 642, pp. 364–369, Nov. 2017, doi: 10.1016/j.tsf.2017.10.014.
[83] N. Bhandaru, P. S. Goohpattader, D. Faruqui, R. Mukherjee, and A. Sharma, "Solvent-Vapor-Assisted Dewetting of Prepatterned Thin Polymer Films: Control of Morphology, Order, and Pattern Miniaturization," *Langmuir*, vol. 31, no. 10, pp. 3203–3214, Mar. 2015, doi: 10.1021/la5045738.
[84] L. Xu, A. Sharma, and S. W. Joo, "Dewetting of Stable Thin Polymer Films Induced by a Poor Solvent: Role of Polar Interactions," *Macromolecules*, vol. 45, no. 16, pp. 6628–6633, Aug. 2012, doi: 10.1021/ma301227m.
[85] L. Xu, T. Shi, and L. An, "Nonsolvent-Induced Dewetting of Thin Polymer Films," *Langmuir*, vol. 23, no. 18, pp. 9282–9286, Aug. 2007, doi: 10.1021/la700805f.
[86] S. H. Lee, P. J. Yoo, S. J. Kwon, and H. H. Lee, "Solvent-driven dewetting and rim instability," *The Journal of Chemical Physics*, vol. 121, no. 9, pp. 4346–4351, Aug. 2004, doi: 10.1063/1.1770475.
[87] "SCUFF-EM documentation." Accessed: Jan. 07, 2024. [Online]. Available: http://homerreid.github.io/scuff-em-documentation/
[88] J. Ye, "Investigation of the mechanism of solid-state dewetting of silver thin films using spatial correlation analysis of hole patterns," *Appl. Phys. Express*, vol. 7, no. 8, p. 085601, Jul. 2014, doi: 10.7567/APEX.7.085601.
[89] "OpenCV: OpenCV modules." Accessed: Sep. 03, 2023. [Online]. Available: https://docs.opencv.org/4.x/index.html
[90] J. I. Goldstein, D. E. Newbury, J. R. Michael, N. W. M. Ritchie, J. H. J. Scott, and D. C. Joy, *Scanning Electron Microscopy and X-Ray Microanalysis*. Springer New York, 2017.
[91] D. D. Evanoff Jr. and G. Chumanov, "Synthesis and Optical Properties of Silver Nanoparticles and Arrays," *ChemPhysChem*, vol. 6, no. 7, pp. 1221–1231, Jul. 2005, doi: 10.1002/cphc.200500113.
[92] F. Heisler *et al.*, "Resonant Optical Properties of Single Out-Diffused Silver Nanoislands," *J. Phys. Chem. C*, vol. 119, no. 47, pp. 26692–26697, Nov. 2015, doi: 10.1021/acs.jpcc.5b09051.
[93] V. Juvé *et al.*, "Size-Dependent Surface Plasmon Resonance Broadening in Nonspherical Nanoparticles: Single Gold Nanorods," *Nano Lett.*, vol. 13, no. 5, pp. 2234–2240, May 2013, doi: 10.1021/nl400777y.
[94] "ICH Q2(R1) Validation of Analytical Procedures: Text and Methodology - ECA Academy." Accessed: May 06, 2023. [Online]. Available: https://www.gmp-compliance.org/guidelines/gmp-guideline/ich-q2r1-validation-of-analytical-procedures-text-and-methodology
[95] J. L. Mauer, J. S. Logan, L. B. Zielinski, and G. C. Schwartz, "Mechanism of silicon etching by a CF4 plasma," *Journal of Vacuum Science and Technology*, vol. 15, no. 5, pp. 1734–1738, Sep. 1978, doi: 10.1116/1.569836.
[96] R. Ghodssi and P. Lin, *MEMS Materials and Processes Handbook*. Springer Science & Business Media, 2011.

[97] “Convert spectrum to color.” Accessed: Jan. 08, 2024. [Online]. Available: https://it.mathworks.com/matlabcentral/fileexchange/98289-convert-spectrum-to-color
[98] S. Yadavali, M. Khenner, and R. Kalyanaraman, “Pulsed laser dewetting of Au films: Experiments and modeling of nanoscale behavior,” *Journal of Materials Research*, vol. 28, no. 13, pp. 1715–1723, Jul. 2013, doi: 10.1557/jmr.2013.90.
[99] S. V. Makarov *et al.*, “Controllable femtosecond laser-induced dewetting for plasmonic applications,” *Laser & Photonics Reviews*, vol. 10, no. 1, pp. 91–99, 2016, doi: 10.1002/lpor.201500119.
[100] C. A. Horwood, E. Owusu-Ansah, Y. J. Shi, and V. I. Birss, “Pulsed laser induced dewetting of Au thin films on Ta2O5 substrates,” *Chemical Physics*, vol. 541, p. 110926, Jan. 2021, doi: 10.1016/j.chemphys.2020.110926.
[101] E. Owusu-Ansah, V. I. Birss, and Y. Shi, “Mechanisms of Pulsed Laser-Induced Dewetting of Thin Platinum Films on Tantalum Substrates—A Quantitative Study,” *J. Phys. Chem. C*, vol. 124, no. 42, pp. 23387–23393, Oct. 2020, doi: 10.1021/acs.jpcc.0c06264.
[102] V. Torrisi, M. Censabella, G. Piccitto, G. Compagnini, M. G. Grimaldi, and F. Ruffino, “Characteristics of Pd and Pt Nanoparticles Produced by Nanosecond Laser Irradiations of Thin Films Deposited on Topographically-Structured Transparent Conductive Oxides,” *Coatings*, vol. 9, no. 2, Art. no. 2, Feb. 2019, doi: 10.3390/coatings9020068.
[103] K.-T. Wang and T.-C. Wei, “Direct Selective Wet Metallization on Glass by Controlling the Hydrophilicity of Glass Surface: Effect of Contact Angle on the Performance of Electroless Deposition,” in *2018 13th International Microsystems, Packaging, Assembly and Circuits Technology Conference (IMPACT)*, Oct. 2018, pp. 173–176. doi: 10.1109/IMPACT.2018.8625763.
[104] D. A. Olsen and A. J. Osteraas, “The Critical Surface Tension of Glass,” *J. Phys. Chem.*, vol. 68, no. 9, pp. 2730–2732, Sep. 1964, doi: 10.1021/j100791a510.
[105] B. A. Kim Y. Pan, Y. M., “The Role of Polarity in the Structure of Silanes Employed in Surface Modification,” in *Silanes and Other Coupling Agents, Volume 5*, CRC Press, 2009.
[106] “1H,1H,2H,2H-Perfluorododecyltrichlorosilane 97 102488-49-3.” Accessed: May 30, 2023. [Online]. Available: http://www.sigmaaldrich.com/
[107] A. Hozumi, K. Ushiyama, H. Sugimura, and O. Takai, “Fluoroalkylsilane Monolayers Formed by Chemical Vapor Surface Modification on Hydroxylated Oxide Surfaces,” *Langmuir*, vol. 15, no. 22, pp. 7600–7604, Oct. 1999, doi: 10.1021/la9809067.
[108] P. Mazumder *et al.*, “Superomniphobic, Transparent, and Antireflection Surfaces Based on Hierarchical Nanostructures,” *Nano Lett.*, vol. 14, no. 8, pp. 4677–4681, Aug. 2014, doi: 10.1021/nl501767j.
[109] M. T. H. Reid, A. W. Rodriguez, J. White, and S. G. Johnson, “Efficient Computation of Casimir Interactions between Arbitrary 3D Objects,” *Phys. Rev. Lett.*, vol. 103, no. 4, p. 040401, Jul. 2009, doi: 10.1103/PhysRevLett.103.040401.
[110] M. Rubin, “Optical properties of soda lime silica glasses,” *Solar Energy Materials*, vol. 12, no. 4, pp. 275–288, Sep. 1985, doi: 10.1016/0165-1633(85)90052-8.
[111] W. Yue *et al.*, “Surface-enhanced Raman scattering with gold-coated silicon nanopillars arrays: The influence of size and spatial order,” *Spectrochimica Acta Part A: Molecular and Biomolecular Spectroscopy*, vol. 267, p. 120582, Feb. 2022, doi: 10.1016/j.saa.2021.120582.

[112] C. D. L. de Albuquerque, R. G. Sobral-Filho, R. J. Poppi, and A. G. Brolo, “Digital Protocol for Chemical Analysis at Ultralow Concentrations by Surface-Enhanced Raman Scattering,” *Anal. Chem.*, vol. 90, no. 2, pp. 1248–1254, Jan. 2018, doi: 10.1021/acs.analchem.7b03968.
[113] J.-E. Shim, Y. J. Kim, J.-H. Choe, T. G. Lee, and E.-A. You, “Single-Nanoparticle-Based Digital SERS Sensing Platform for the Accurate Quantitative Detection of SARS-CoV-2,” *ACS Appl. Mater. Interfaces*, vol. 14, no. 34, pp. 38459–38470, Aug. 2022, doi: 10.1021/acsami.2c07497.
[114] L. Mikac, I. Rigó, L. Himics, A. Tolić, M. Ivanda, and M. Veres, “Surface-enhanced Raman spectroscopy for the detection of microplastics,” *Applied Surface Science*, vol. 608, p. 155239, Jan. 2023, doi: 10.1016/j.apsusc.2022.155239.
[115] P. C. Braga and D. Ricci, *Atomic Force Microscopy: Biomedical Methods and Applications*. Springer Science & Business Media, 2008.
[116] M. Giardino, D. M. N. Menon, and D. L. Janner, “Regularization techniques for 3D surface reconstruction from four quadrant backscattered electron detector images,” *Ultramicroscopy*, vol. 250, p. 113746, Aug. 2023, doi: 10.1016/j.ultramic.2023.113746.
[117] A. Ul-Hamid, *A Beginners’ Guide to Scanning Electron Microscopy*. Springer, 2018.
[118] L. Reimer, *Scanning Electron Microscopy: Physics of Image Formation and Microanalysis*. Springer, 2013.
[119] J. Hejna, “Detection of Topographic Contrast in the Scanning Electron Microscope at Low and Medium Resolution by Different Detectors and Detector Systems,” *Scanning Microscopy*, vol. 8, no. 2, Jul. 1994, [Online]. Available: https://digitalcommons.usu.edu/microscopy/vol8/iss2/1
[120] W. Slówko, “Directional detection of secondary electrons for electron beam profilography,” *Vacuum*, vol. 52, no. 4, pp. 441–449, Apr. 1999, doi: 10.1016/S0042-207X(98)00329-7.
[121] W. Slowko and M. Krysztof, “Detector System for Three-Dimensional Imaging in the Variable Pressure/Environmental SEM,” *Acta Physica Polonica Series a*, vol. 123, pp. 877–879, Jan. 2014, doi: 10.12693/APhysPolA.123.877.
[122] J. Paluszyński and W. Slówko, “Surface reconstruction with the photometric method in SEM,” *Vacuum*, vol. 78, no. 2, pp. 533–537, May 2005, doi: 10.1016/j.vacuum.2005.01.081.
[123] P. Kovesi, “Good Colour Maps: How to Design Them.” arXiv, Sep. 11, 2015. doi: 10.48550/arXiv.1509.03700.
[124] S. Ettl, J. Kaminski, M. C. Knauer, and G. Häusler, “Shape reconstruction from gradient data,” *Applied Optics*, vol. 47, no. 12, pp. 2091–2097, Apr. 2008, doi: 10.1364/AO.47.002091.
[125] M. Harker and P. O’Leary, “Least squares surface reconstruction from measured gradient fields,” in *2008 IEEE Conference on Computer Vision and Pattern Recognition*, Jun. 2008, pp. 1–7. doi: 10.1109/CVPR.2008.4587414.
[126] M. Harker and P. O’Leary, “Direct regularized surface reconstruction from gradients for Industrial Photometric Stereo,” *Computers in Industry*, vol. 64, no. 9, pp. 1221–1228, Dec. 2013, doi: 10.1016/j.compind.2013.03.013.
[127] M. Harker and P. O’Leary, “Regularized Reconstruction of a Surface from its Measured Gradient Field.” arXiv, Aug. 2013. doi: 10.48550/arXiv.1308.4292.
[128] F. Benvenuto and B. Jin, “A parameter choice rule for Tikhonov regularization based on predictive risk,” *Inverse Problems*, vol. 36, no. 6, p. 065004, May 2020, doi: 10.1088/1361-6420/ab6d58.

[129] N. Marturi, S. Dembélé, and N. Piat, “Depth and Shape Estimation from Focus in Scanning Electron Microscope for Micromanipulation,” presented at the CARE 2013 - 2013 IEEE International Conference on Control, Automation, Robotics and Embedded Systems, Proceedings, Dec. 2013. doi: 10.1109/CARE.2013.6733694.
[130] A. Boyde, “Improved digital SEM of cancellous bone: scanning direction of detection, through focus for in-focus and sample orientation,” *Journal of Anatomy*, vol. 202, no. 2, pp. 183–194, 2003, doi: 10.1046/j.1469-7580.2003.00146.x.
[131] A. Boyde, “Improved depth of field in the scanning electron microscope derived from through-focus image stacks,” *Scanning*, vol. 26, no. 6, pp. 265–269, 2004, doi: 10.1002/sca.4950260602.
[132] B. Forster, D. Van De Ville, J. Berent, D. Sage, and M. Unser, “Extended depth-of-focus for multi-channel microscopy images: a complex wavelet approach,” in *2004 2nd IEEE International Symposium on Biomedical Imaging: Nano to Macro (IEEE Cat No. 04EX821)*, Apr. 2004, pp. 660-663 Vol. 1. doi: 10.1109/ISBI.2004.1398624.
[133] F. Aguet, D. Van De Ville, and M. Unser, “Model-Based 2.5-D Deconvolution for Extended Depth of Field in Brightfield Microscopy,” *IEEE Transactions on Image Processing*, vol. 17, no. 7, pp. 1144–1153, Jul. 2008, doi: 10.1109/TIP.2008.924393.
[134] L. Prasad and S. S. Iyengar, *Wavelet Analysis with Applications to Image Processing*. CRC Press, 2020.
[135] P. Apel, “Track etching technique in membrane technology,” *Radiation Measurements*, vol. 34, no. 1, pp. 559–566, Jun. 2001, doi: 10.1016/S1350-4487(01)00228-1.
[136] D. Kaya and K. Keçeci, “Review—Track-Etched Nanoporous Polymer Membranes as Sensors: A Review,” *J. Electrochem. Soc.*, vol. 167, no. 3, p. 037543, Jan. 2020, doi: 10.1149/1945-7111/ab67a7.
[137] I. Junkar, A. Vesel, U. Cvelbar, M. Mozetič, and S. Strnad, “Influence of oxygen and nitrogen plasma treatment on polyethylene terephthalate (PET) polymers,” *Vacuum*, vol. 84, no. 1, pp. 83–85, Aug. 2009, doi: 10.1016/j.vacuum.2009.04.011.
[138] J. P. Fernández-Blázquez and A. del Campo, “Templateless nanostructuration of polymer surfaces,” *Soft Matter*, vol. 8, no. 8, pp. 2503–2508, Feb. 2012, doi: 10.1039/C2SM06739K.
[139] M. Amberg *et al.*, “Surface modification of recycled polymers in comparison to virgin polymers using Ar/O2 plasma etching,” *Plasma Processes and Polymers*, vol. 19, no. 12, p. 2200068, 2022, doi: 10.1002/ppap.202200068.
[140] M. Horprathum, P. Eiamchai, P. Chindaudom, A. Pokaipisit, and P. Limsuwan, “Oxygen Partial Pressure Dependence of the Properties of TiO2 Thin Films Deposited by DC Reactive Magnetron Sputtering,” *Procedia Engineering*, vol. 32, pp. 676–682, Jan. 2012, doi: 10.1016/j.proeng.2012.01.1326.